이학박사 학위논문

# Development and application of analytical methods for boron isotope proxy: paleoceanographic interpretation of Paleozoic and Cenozoic carbonates

붕소 동위원소 지시자의 분석법 개발과 활용:

고생대와 신생대 탄산염에 대한 고해양학적 이해

2023년 2월

서울대학교 대학원

지구환경과학부

방 선 화

# Development and application of analytical methods for boron isotope proxy: paleoceanographic interpretation of Paleozoic and Cenozoic carbonates

지도 교수 허 영 숙

이 논문을 이학박사 학위논문으로 제출함
2022 년 10 월

서울대학교 대학원
지구환경과학부
방 선 화

방선화의 이학박사 학위논문을 인준함
2023 년 1 월

위 원 장 심 민 섭 (인)

부위원장 허 영 숙 (인)

위 원 우 주 선 (인)

위 원 홍 성 경 (인)

위 원 서 인 아 (인)

# Abstract

# Development and application of analytical methods for boron isotope proxy: paleoceanographic interpretation of Paleozoic and Cenozoic carbonates

Sunhwa Bang

School of Earth and Environmental Sciences

The Graduate School

Seoul National University

Boron isotopes of marine carbonate ($CaCO_3$) are known as an indicator of pH and $CO_2$ content in past seawater. This thesis aims to improve understanding the boron isotope method through research in past marine carbonates (e.g., Cenozoic foraminifera and Paleozoic carbonate rocks). This thesis consists of three chapters that deal with pH-dependant fractionation of boron isotopes (Chapter 1) and reconstructed pH and $pCO_2$ records in paleoceanographic case studies (Chapters 2 and 3).

In Chapter 2, multiple planktic foraminiferal species were separated and cleaned from the sediment core NPGM/P 1302-1B (32° 16′ N, 158° 13′ E, 2514 m water depth), located on Shatsky Rise in the western North Pacific(WNP), to examine the oceanic $pCO_2$ at the time scale of last glacial maximum (LGM; 24 – 18 ka), Heinrich stadial-1 (HS1; 18 – 15 ka), Bolling-Allerod (B/A; 15 – 12.8 ka), Younger Dryas (YD; 12.8 – 11.5 ka). The new WNP $\delta^{11}B$, pH, and $pCO_2$ records for the 4 – 23 kyr reveal distinct $CO_2$ degassing patterns in the LGM-to-HS1 transition period (19.7 – 17.5 ka), the middle HS1 (16 – 17 ka), and the early YD. The new $\Delta pCO_2$ data of the WNP was compared by other

Pacific core studies (North, West equatorial, East equatorial Pacific) in the last deglaciation. WNP shows similarities in the $\Delta pCO_2$ of East equatorial Pacific (EEP) and the North Pacific (NP) up to LGM and middle HS1, YD in the Pacific compilation. These changes can be explained by the relationships between surface-intermediate currents in the Northern Hemisphere Pacific, especially during rapid atmospheric $CO_2$ rise.

In Chapter 3, boron isotope extraction and analysis from carbonate rock were experimentally applied to the lower Paleozoic stratigraphy in the Taebaek group, Joseon Supergroup of the Korean Peninsula. This study tested which dissolution method was effective on carbonate rock samples with different insoluble residue contents. As a result, we found the acid concentration range and reaction time to minimize contamination by clay minerals. This new pretreatment method reconstructed the new $\delta^{11}B$ record from 25 carbonate rock samples of middle Drriwillian isotopic carbon excursion (MDICE) in the Middle Ordovician. The new $\delta^{11}B_{bulk}$ data compared by global $\delta^{11}B$ in the literature of Ordovician seawater and $\delta^{13}C$ chemostratigraphy in updated biostratigraphy. These results support the hypothetic relationship between the oceanic stratification and acidification of Taebaek as a shallow carbonate platform environment in a peri-Gondwanan epeiric sea.

**Keywords: boron isotope, paleoceanography, $CO_2$ flux, acidification, marine carbonate, climate change**

**Student Number: 2017-34629**

# TABLE OF CONTENTS

# LIST OF FIGURES

# LIST OF TABLES

# Chapter 1. Introduction: Boron isotope as a proxy of oceanic acidification and $CO_2$ storage

## 1.1. Boron isotope in seawater

Boron isotope ratios in marine carbonate sediments have been attracting attention as indicators of palaeoclimate and paleoceanography over the past decade. The reason is that boron is an indicator that allows us to find out the acidity (pH) of seawater in the past, and it is an indicator that can determine the characteristics of seawater at the time. Due to these merits, effective separation and analysis of boron isotopes are being continuously developed despite the factors that have been difficult to experiment with in the past, such as the volatility of boron and the overall high boron background in the laboratory (McCulloch et al., 2014; Sadekov et al., 2019).

The isotopes of boron are $^{10}B$ (about 20% of natural boron) and $^{11}B$ (about 80%), and the isotope ratio is expressed in parts per thousand (‰) using the delta (δ) notation like other stable isotopes. The standard (standard) for the denominator used here is SRM 951a boric acid ($^{11}B/^{10}B$ = 4.04367) from the National Institute of Science and Technology (NIST).

$$\delta^{11}B = \left( \frac{^{11}B/^{10}B_{\text{sample}}}{^{11}B/^{10}B_{\text{NIST951}}} - 1 \right) \times 1{,}000‰$$

On the other hand, boron in seawater exists as tetrahedral borate ions ($B(OH)_4^-$) and trigonal boric acid (B(OH)3), and their abundance is dependent on the pH value (**Fig. 1**).

The equilibrium of the two boron species in seawater is given by:

$B(OH)_3 + H_2O = B(OH)_4^- + H^+$

Since the equilibrium constant value ($K_B$) of the above reaction is 8.6, similar to the pH of seawater, the relative ratio of the two chemical species and the boron isotope ratio in seawater change sensitively according to pH (**Fig. 1**a; Foster and Rae, 2016). Among these, it is known that the borate ion $B(OH)_4^-$ is mainly incorporated into the marine carbonate. In addition, the isotopic ratio of boric acid contained in marine carbonate also changes according to pH because $^{11}B$, which has a heavier mass, is selectively distributed to boric acid species with stronger B-O bonding (**Fig. 1b**; Foster and Rae, 2016).

$$CaCO_3 + B(OH)_4^- \Rightarrow Ca(HBO_3) + HCO_3^- + H_2O.$$

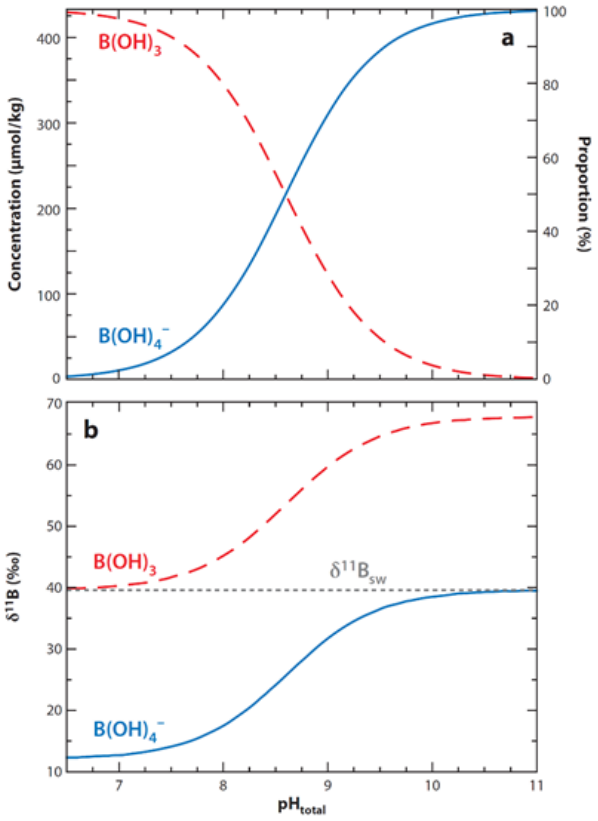


**Figure 2-1**. (a) Relative concentration change and (b) isotope ratio change of borate ion and boric acid according to pH for standard seawater conditions (25°C, 34.7 PSU). $pH_{total} = \log[H^+]_T$, $pH_{total}$ is an acidity unit that controls acidity in a buffer solution such as seawater and includes all ions (mainly the sum of $[H^+]$ and $[HSO_4^-]$) that play a role in buffer solution (Foster and Rae, 2016).

## 1.2. Boron isotope proxy-derived pH, seawater $pCO_2$

The carbonic acid equilibrium determines the amount of carbon dioxide stored in seawater, and the ratio of carbonic acid ($CO_2$), bicarbonate ($HNO_3^{2-}$), and carbonate ion ($CO_3^{2-}$) is controlled by the equilibrium equation below.

$$CO_2 + H_2O \overset{K_1}{\Leftrightarrow} H^+ + HCO_3^{2-} \overset{K_2}{\Leftrightarrow} 2H^+ + CO_3^{2-}$$

In this case, K1 and K2 are dissociation constants depending on temperature, salinity, and pressure.

Dissolved inorganic carbon (DIC) and alkalinity (ALK) can also be expressed as the sum of the major ions participating in the above reaction.

$$DIC = [CO_2] + [HCO_3^-] + [CO_3^{2-}],$$

$$ALK = [HCO_3^-] + 2[CO_3^{2-}] - [H^+],$$

$$K_1^* = \frac{[HCO_3^-][H^+]}{[CO_2]},$$

$$K_2^* = \frac{[CO_3^{2-}][H^+]}{[HCO_3^-]}.$$

It should be noted in this relationship that $H^+$ is commonly included in the factors that can determine the constant. In other words, if atmospheric $CO_2$ partial pressure, alkalinity, salinity, and temperature can be estimated through collaboration with the ice core and other proxies, the amount of carbon dioxide stored in the ocean and partial pressure of carbon dioxide in the atmosphere at the time by restoring the pH value using boron isotopes can be estimated (Zeebe and Wolf-Gladrow, 2001; Zeebe et al., 2003).

As mentioned above, the chemical species of boron is pH-dependent, and the separation rate in seawater can also be expressed as the concentration of $H^+$ ions.

$$[B(OH)_3] = \frac{[B]_{sw}}{1 + K_B^*/[H^+]},$$

$$[B(OH)_4^-] = \frac{[B]_{sw}}{1 + [H^+]/K_B^*}$$

$$K_B^* = \frac{[B(OH)_4^-][H^+]}{[B(OH)_3]}$$

On the other hand, since the isotopic value ranges of boron species are different, the separation of the isotopes is also pH-dependent (**Fig. 1-1**).

$$^{10}B(OH)_3 + {}^{11}B(OH)_4^- \Leftrightarrow {}^{11}B(OH)_3 + {}^{10}B(OH)_4^-$$

$$\delta^{11}B_{B(OH)_3} = \delta^{11}B_{B(OH)_4^-} \times \alpha_B + \varepsilon_B.$$

$$\delta^{11}B_{B(OH)_4^-} = \frac{\delta^{11}B_{sw} + (\delta^{11}B_{sw} - \varepsilon_B) \times 10^{pK_B^* - pH}}{1 + \alpha_B \times 10^{pK_B^* - pH}}.$$

$$\alpha_B = \frac{{}^{\frac{11}{10}}R_{B(OH)_3}}{{}^{\frac{11}{10}}R_{B(OH)_4^-}},$$

$$\varepsilon_B = (\alpha_B - 1) \times 1{,}000.$$

In this case, the isotopic fractionation constant is called $\alpha_B$, and the expression of $\alpha_B$ in the epsilon unit($\varepsilon$) is called $\varepsilon_B$.

The first direct measurement of $\alpha_B$ in seawater was determined to be 1.0272 ± 0.0006 at 25ºC and a salinity of 35 PSU (Klochko et al., 2006). Klochko et al. (2006) confirmed measurements of $\alpha_B$ at elevated temperature (~40ºC) in seawater, giving 1.0269 ± 0.0027, within error of the value for 25˚C but with relatively considerable uncertainty. As a result, the environmental sensitivity of $\alpha_B$ is currently underconstrained.

In conclusion, by combining the above relational and equilibrium equations, the pH in seawater where

carbonate equilibrium occurs can be expressed only with boron isotope values (Zeebe & Wolf-Gladrow 2001)

$$\mathrm{pH} = \mathrm{p}K_{\mathrm{B}}^{*} - \log\left(-\frac{\delta^{11}\mathrm{B}_{\mathrm{sw}} - \delta^{11}\mathrm{B}_{\mathrm{CaCO_3}}}{\delta^{11}\mathrm{B}_{\mathrm{sw}} - \alpha_{\mathrm{B}}\delta^{11}\mathrm{B}_{\mathrm{CaCO_3}} - \varepsilon_{\mathrm{B}}}\right)$$

$$[\mathrm{CO_2}] = \left(\mathrm{TA} - \frac{K^{*}_{\mathrm{B}}\mathrm{B_T}}{K^{*}_{\mathrm{B}} + [\mathrm{H^+}]} - \frac{K^{*}_{\mathrm{W}}}{[\mathrm{H^+}]} + [\mathrm{H^+}]\right) \Big/ \left(\frac{K^{*}_{1}}{[\mathrm{H^+}]} + \frac{K^{*}_{1}K^{*}_{2}}{[\mathrm{H^+}]^2}\right)$$

In the above pH equation, $\delta^{11}B_{CaCO3}$ needs correction according to each carbonate-making organism (e.g., foraminifera, coral) (Foster et al., 2018; Greenop et al., 2017; Raitzsch et al., 2018). Also, in the case of carbonate rocks formed by sedimentation, additional simulations of the sedimentation environment may be required (Clarkson et al., 2015; Kasemann et al., 2000; Paris et al., 2010). The calibration procedure for pH reconstruction with $\delta^{11}B$ calcite will be discussed in more detail in Chapter 2 (foraminifera) and Chapter 3 (carbonate rock).

In paleoceanographic studies that studied boron isotope, the value of seawater $pCO_2$ dramatically depends on the value of pH, and it is a method to infer from the error range of other factors (e.g., temperature, salinity, alkalinity, DIC) (Foster and Rae, 2016; Zeebe and Wolf-Gladrow, 2001). The following dissolved CO2 concentration derivation equation can be derived from the relationship between the reaction equations described above. The data uncertainties on each variable (temperature, salinity, alkalinity, DIC) should be considered in Monte Carlo simulations. This function can be applied to the *seacarb* package in R (Gattuso and Lavigne, 2009; Gray et al., 2018; Martínez-Botí et al., 2015; Shao et al., 2019) and the Python module such as a MyAMI model (Hain et al., 2015;

Sosdian et al., 2018). One of the examples implemented in our study (e.g., Chapter 2), the *seacarb* package in R was mainly used in the method applied by previous studies.

We want to introduce the method of analyzing boron isotopes in Cenozoic foraminifera (Chapter 2) and Paleozoic carbonate rock (Chapter 3) and the results of calculated pH and $pCO_2$ and consider their implications.

# Chapter 2. Factors regulating $CO_2$ emissions in the western North Pacific gyre transition zone in the last deglaciation

## 2.1. Introduction

Some of the most significant air-sea fluxes of $CO_2$ in the modern North Pacific occur in the transition zone between the subpolar gyre (SPG) and the subtropical gyre (STG) (**Fig. 2-1**). Latitudinally, this transition zone is between 32°N and 42°N, though it varies seasonally (**Fig. 2-1a**) (Roden, 1991). The Kuroshio Extension (KE) is the main surface current in the transition zone with its present-day central axis at 34-35°N. It results from mixing the Oyashio current (OC) from the cooler and less saline SPG and the Kuroshio current (KC) from the STG (**Fig. 2-1a**) (Yasuda, 2003). The KE also undergoes large-scale path changes (34°N–37°N) seasonally and interannually as the gyre positions shift (Mizuno and White, 1983; Na et al., 2018; Sakamoto et al., 2005). The southern migration of the KE axis with the expansion of the SPG was also documented in the past, e.g., the Last Glacial Maximum (LGM) (Thompson, 1981; Ujiié et al., 2016), Younger Dryas (YD) and Heinrich Stadial-1 (HS1) (Harada et al., 2004; Kawahata and Ohshima, 2002; Ohkushi et al., 1999; Seo et al., 2018). Changes in sea surface temperature (SST), El Niño/Southern Oscillation (ENSO), and the Pacific Decadal Oscillation (PDO) cause changes in the climatological wind stress curl. The combination of these factors affects the latitude of bifurcation of KC from the North equatorial current (NEC) (**Fig. 2-1**) and the strength of the KC and the latitudinal position of the STG (Hu et al., 2015; Kawahata and Ohshima, 2002). For example, (i) during seasonal or climatological warming, (ii) under La Niña-like status in the east equatorial

Pacific, or (iii) under cold PDO mode, the wind stress curl is increased and the KC bifurcates from the NEC at a more southerly latitude (12-13°N) and drifts in high wind stress curl by enhanced easterlies (Jin, 1997; Qiu and Chen, 2010; Wu et al., 2019). In the case of stronger KC, the STG boundary expands to more northerly latitudes. In the opposite cases, the KC-NEC bifurcation occurs at a more northern latitude (~15°N); the weaker KC means a contracted STG and the boundary shift to more southerly latitudes (Qiu et al., 2019; Wu et al., 2019).

Regarding air-sea $CO_2$ fluxes, the STG-SPG transition zone is an important sink in the modern ocean (**Fig. 2-1b**). To determine its role as a $CO_2$ sink, $\Delta pCO_2$ can be calculated relative to the contemporaneous atmospheric $pCO_2$ notated as follows:

$$\Delta pCO_2 = pCO_{2,\,sw} - pCO_{2,\,atm}$$

Atmospheric $pCO_2$ values can be obtained from ice core records (Bereiter et al., 2015), and $pCO_2$ of past seawater can be reconstructed using boron isotopes. Regions of negative $\Delta pCO_2$ can be considered '$CO_2$ sink' that captures $CO_2$ from the atmosphere and stores it dissolved in the seawater, and regions of positive $\Delta pCO_2$ are '$CO_2$ source'. Records of $\Delta pCO_2$ have been reconstructed for the Cenozoic across the global oceans (Rae et al., 2021; Shao et al., 2019; Shuttleworth et al., 2021). In the Pacific, the $\Delta pCO_2$ record is available for the modern $CO_2$ source areas, e.g., East Equatorial Pacific (Martinez-Boti et al., 2015), sub-Antarctic zone (Martinez-Boti et al., 2015; Shuttleworth et al., 2021), and the North Pacific (Gray et al., 2018). However, records for the modern $CO_2$ sink areas are limited to the subtropical South Pacific and regional variations in West Equatorial Pacific (Kubota et al., 2019; Palmer and Pearson, 2003; Shao et al., 2019).

Understanding the STG-SPG expansion relationship that dominates the substantial surface currents of the northern Pacific Ocean is particularly important during the last deglaciation period. In particular, among the deglacial periods after the LGM, HS1 ($CO_2$, atm increased ~50 ppmv) and YD ($CO_2$, atm increased ~30 ppm) are known periods when atmospheric $CO_2$ increased rapidly (Bereiter et al., 2015). Since the ocean is the largest pool of $CO_2$, it is necessary to synthesize how $pCO_2$ in Pacific waters saturates in different marine environments during these unique periods and what factors control it. In particular, from the perspective of the Pacific Ocean, it has been hypothesized that when the STG influence increases due to warming in the North Pacific, where the influence of SPG is usually dominant, intermediate $CO_2$ pools become shallow with less intermediate water sinking (Gray et al., 2018; Gray et al., 2020). Meanwhile, in the STG-dominated Western Equatorial Pacific and Eastern Equatorial Pacific, the process of mode water transport from the Southern Ocean played an important role, and $pCO_2$ records were found that may have increased upwelling at the thermocline depth during periods of $CO_2$ increase (Kubota et al., 2019). Referring to these cases, this study attempted to examine the $pCO_2$ record of seawater at WNP, where SPG and STG meet, and its relationship with nearby Pacific regions.

In this study, we present a $\Delta pCO_2$ record based on boron isotopes for a core located in the western North Pacific (WNP) in a strong $CO_2$ sink region in the STG-SPG transition zone, an area traversed by the KE (**Fig. 2-1b**). For $\delta^{11}B$ analyses, we picked multiple species of planktic foraminifera (Table S1). Records from various species prevented discontinuity due to the shift in dominant species with changes in sea surface temperature and salinity in the SPG-STG transition zone. The relative abundance of foraminifera species of these cores indeed documents the past position of the gyres. The

subtropical species (*Trilobatus sacculifer, Globigerinoides ruber,* and *Globorotalia truncatulinoides*) were dominant throughout the last 23 kyrs. Still, the abundance of subpolar species (*Neogloboquadrina pachyderma, N. dutetrei, N. incompta*) increased during the Heinrich Stadial 1 (HS1) and the Younger Dryas (YD), indicating the southern migration of the SPG (Seo et al., 2018). Therefore, the oceanic $pCO_2$ records from this area can provide SPG-STG relationships between Pacific $CO_2$ changes with the shift in ocean circulation.

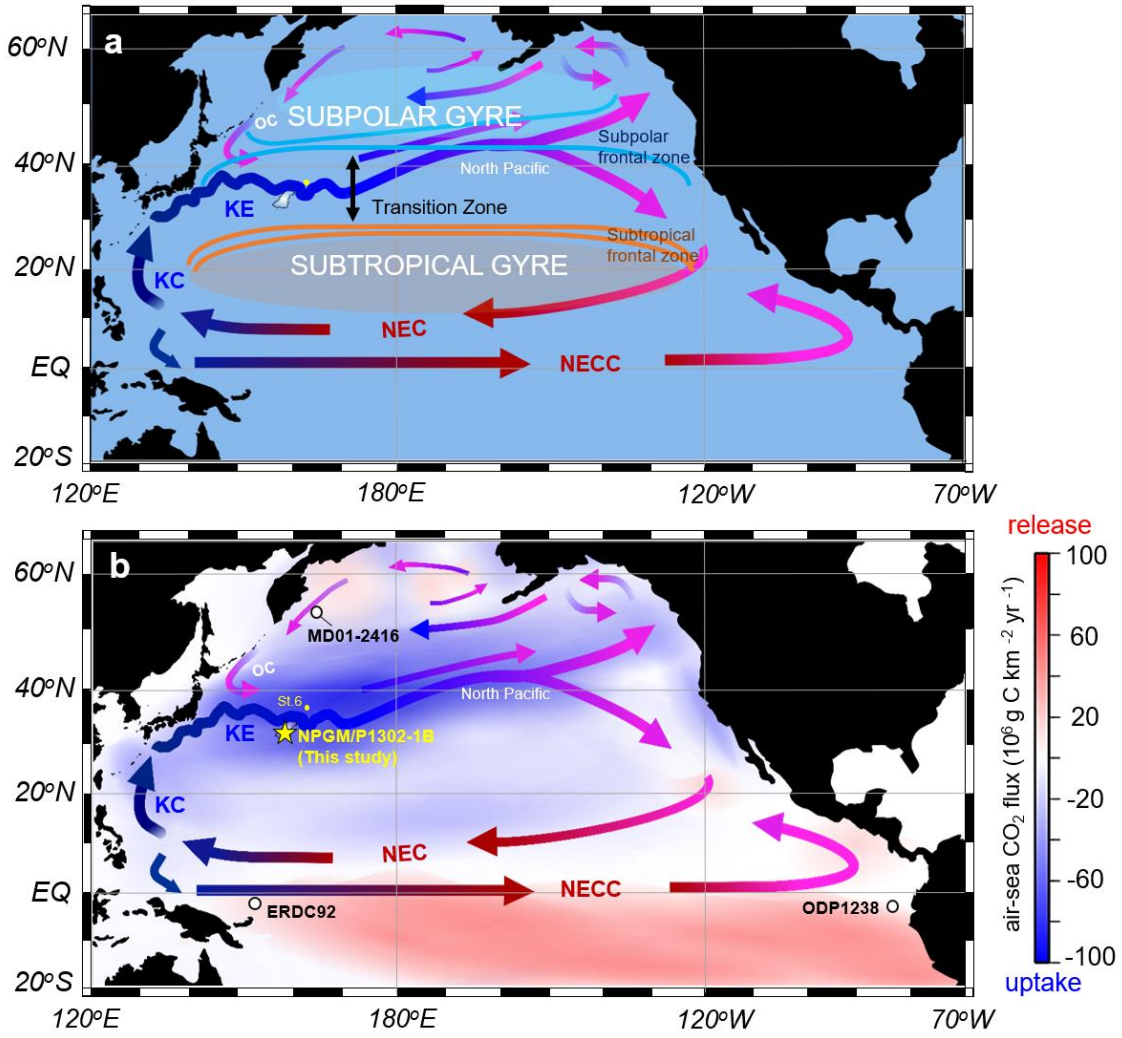


**Figure. 2-3. The surface circulation system and air-sea $CO_2$ flux of the Pacific Ocean and core locations.** (a) The gyre system of the North Pacific and surface currents. The climatological mean positions are depicted (Roden et al., 1991; Howell et al., 2012; Hu et al., 2015). (b) Modern (year 2008) air-sea $CO_2$ flux map (Japan Meteorological Agency) with core locations of this study (star symbol) and other boron isotope-based $pCO_2$ studies (white circle). **OC**: Oyashio Current, **KE**: Kuroshio Extension, **KC**: Kuroshio Current, **NEC**: North Equatorial Current, **NECC**: North Equatorial Counter-Current.

## 2.2. Study Area

Sediment cores NPGM 1302-1B (24 cm long) and NPGP1302-1B (613 cm long) were raised from the Tamu Massif (32° 16′ N, 158° 13′ E, 2514 m water depth) of the Shatsky Rise in the western North Pacific (WNP) (**Fig. 2-1b**). The Shatsky Rise developed by the large igneous province between the three plates (Pacific, Izanagi, Farallon) from the late Jurassic (140-150 Ma) period and consisted of three high massifs known as Tamu, Ori, Shirsshov (Heydolph et al., 2014; Georgen and Shotorban, 2021). Among them, Tamu massif, where the location of studied core NPGM/P 1302-1B, is the southern high in overall Shatsky Rise. The oceanic station 48292 (32º01'N, 155º04'E), referred to as the depth profile of present seawater in this study, was also sampled in the surrounding area of Tamu massif (**Fig. 2-2**) (Key et al., 2004).

Core NPGM 1302-1B retrieved with multiple corers substituted for the disturbed uppermost section of the piston core NPGP1302-1B. The relative abundance of planktic foraminiferal species and $\delta^{18}O$ of planktic and benthic foraminifera have been reported for these cores by Seo et al. (2018). The core site is close to the southern limit of the modern KE (**Fig. 2-1b**), although the position of the KE axis and SPG-STG transition zone have changed during the last deglaciation due to the gyre boundary shift (De Boer et al., 2013; Gray et al., 2020; Seo et al., 2018).

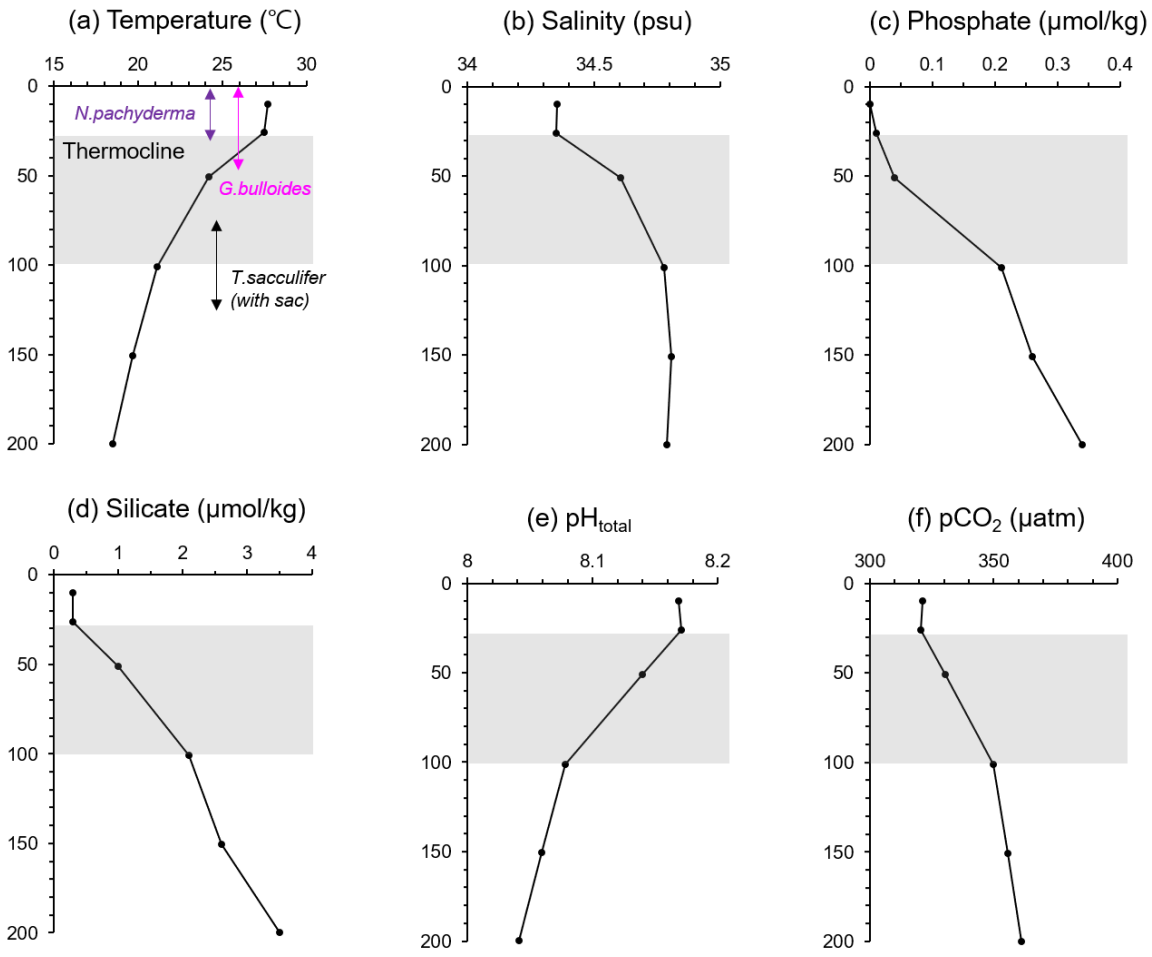


**Figure 2-2.** Vertical profile of seawater chemistry from Southern-high Shatsky Rise (GLODAP dataset; station 48292; Key et al., 2004) and calcifying depth estimation of planktonic foraminifera (G.bulloides, N.pachyderma, and T.sacculifer with sac). (a) Temperature of water column, gray shaded area referred as thermocline depth (4-50 m), (b) salinity (c) phosphate con (d) silicate concentration (e) $pH_{total}$, data (a)-(e) from GLODAP dataset and (f) seawater $pCO_2$ calculated by vertical temperature, salinity and total alkalinity.

## 2.3. Analytical Methods

### 2.3.1. Sample Information

The age model of this core was established by Seo et al. (2018) by radiocarbon ($^{14}C$) dating the mixed planktic foraminifera – three dates on the shorter core and 7 dates on the longer core (**Fig. 2-3, Table 2-1**). The uncertainty on the $^{14}C$ age was less than 70 years, and they used a reservoir age of 414 years (Seo et al., 2018).

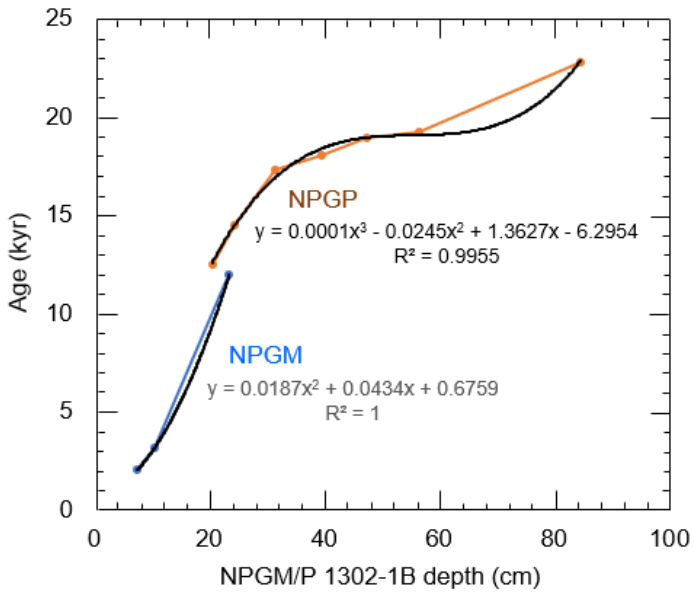


**Figure 2-3. Age dating of core NPGM/P 1302-1B.** (a) Radiocarbon ($^{14}C$-AMS) ages for NPGM/P 1302-1B measured from mixed species of planktic foraminifera (Seo et al., 2018) (b) Chronology of WNP core NPGM 1302-1B and NPGP 1302-1B. Orange circles and line, calendar ages of NPGM 1302-1B and linear fit; blue circles and line, calendar ages of NPGM 1302-1B and linear fit; black line, representative polynomial fit with equations.

**Table 2-1.** Radiocarbon ages of the NPGM/P 1302-1B measured from multi-species planktic foraminifera samples (modified after Seo et al., 2018).

| Core ID | Depth(cm) | $^{14}$C age (year) | ±1σ | Calendar age* (year) | ±1σ |
|---|---|---|---|---|---|
| NPGM1302-1B | 7–8 | 2830 | 30 | 2051 | 49 |
| NPGM1302-1B | 10–11 | 3750 | 30 | 3188 | 52 |
| NPGM1302-1B | 23–24 | 11,070 | 30 | 11998 | 76 |
| NPGP1302-1B | 20–21 | 11,380 | 40 | 12538 | 51 |
| NPGP1302-1B | 24–25 | 13,260 | 40 | 14545 | 182 |
| NPGP1302-1B | 31–32 | 15,050 | 40 | 17336 | 100 |
| NPGP1302-1B | 39–40 | 15,680 | 50 | 18061 | 91 |
| NPGP1302-1B | 47–48 | 16,530 | 50 | 18928 | 80 |
| NPGP1302-1B | 56–57 | 16,760 | 50 | 19227 | 106 |
| NPGP1302-1B | 84–85 | 19,790 | 70 | 22838 | 125 |

*Converted by CALIB 7.1 calibration program (Stuiver et al., 2017)

Three species of planktonic foraminifera (*G. bulloides, N. pachyderma,* and *T. sacculifer with sac*) were collected. These species allowed a continuous reconstruction over the deglacial for the surface and the lower thermocline. The calcifying depth, size fraction, and calibration reference of these species are summarized in **Table 2-2**. The calcifying depth of *G. bulloides* and *N. pachyderma* was reported to the surface and photic zone (0 to 50m), while *T.sacculifer* with sac-like chamber and gametogenic calcite coating, prefers deeper water-mass surrounding thermocline (**Table 2-2**)

The mass of each sample was 0.8-2 mg (40 to 100 individuals), checked under the microscope for the pore, shape, and in the case of *T. sacculifer,* the presence of a sac-like chamber (**Fig. 2-4**).

**Table 2-2.** List of planktic foraminifera species for boron isotope analysis and summary of sample information.

| Species | Calcifying depth (m) | sample size (μm) | $\delta^{11}B$ data (n) | References for habitat, borate equation |
|---|---|---|---|---|
| *Globigerina bulloides* | ~50 | 300-355 | 16 | (Darling et al., 2017; Henehan et al., 2016; Martínez-Botí et al., 2015) |
| *Trilobus Sacculifer w. sac* | ~125 | 425-500, | 21 | (Henehan et al., 2016; Kubota et al., 2019; Martínez-Botí et al., 2015; Scott, 2020) |
| *Neogloboquadrina pachyderma* | ~25 | 150-250 | 26 | (Darling et al., 2017; Henehan et al., 2016; Gray et al., 2018) |

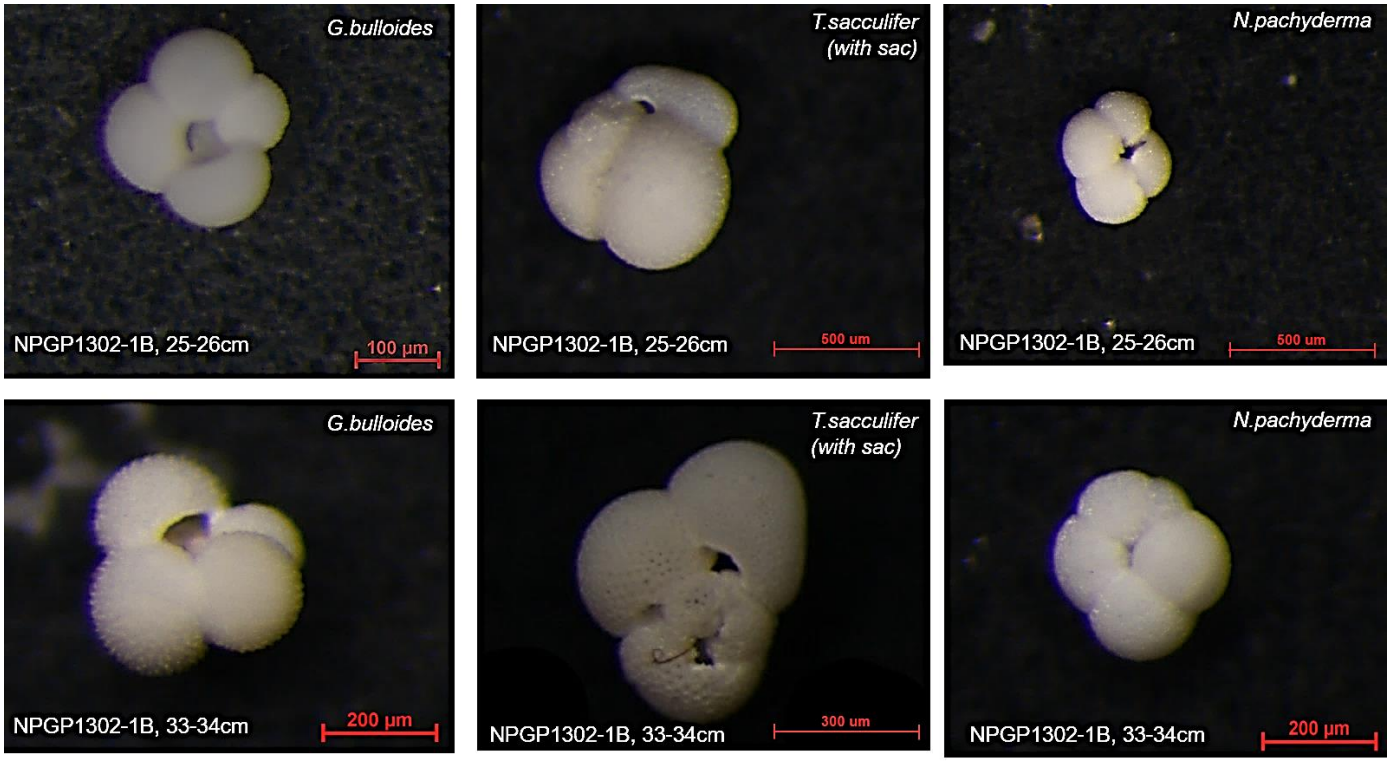


**Figure 2-4.** Microscope images of planktonic foraminifera samples from this study. The cores and depth (cm) are given.

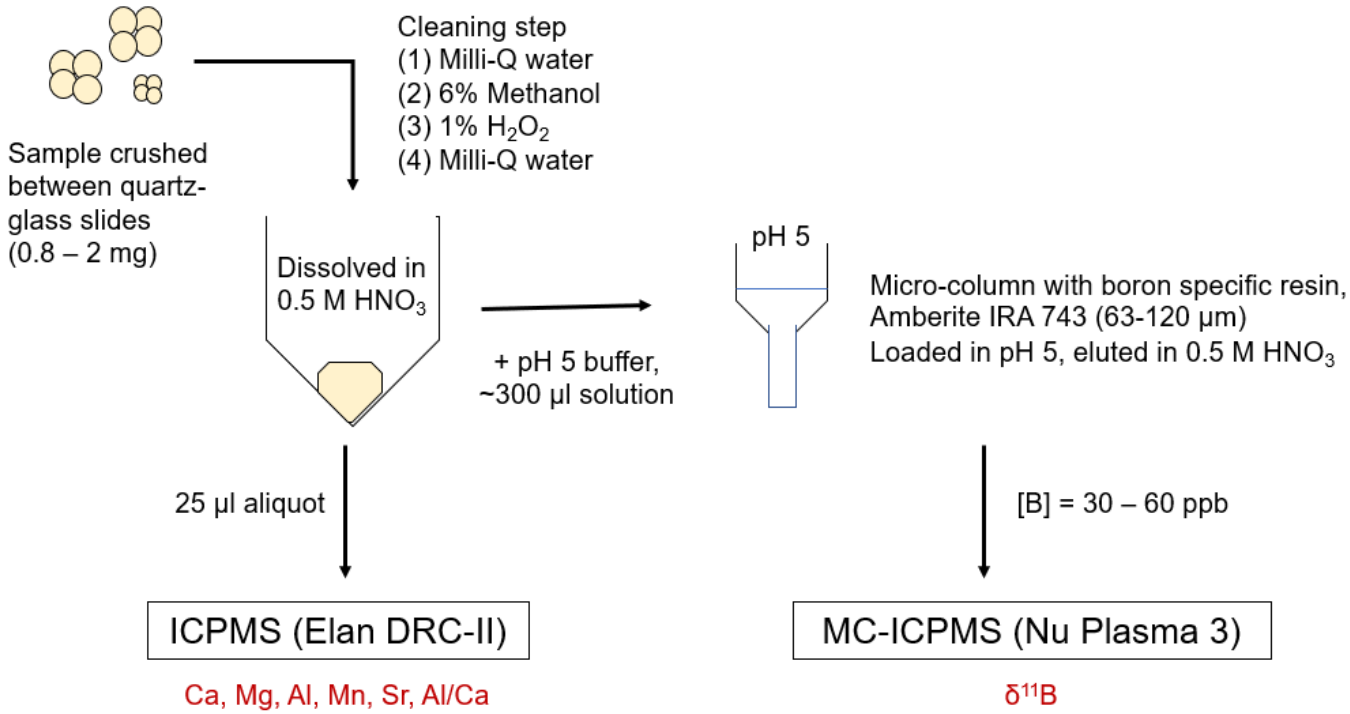


**Figure 2-5.** Schematic description of sample pretreatment and analysis (modified from Kubota et al., 2019; Foster, 2008)

### 2.3.2. Extraction and Analysis of Boron isotopes

Dissolving and column separation was processed under a ULPA-filtered laminar flow bench to lower the blank boron levels. The nitric acid used throughout the boron analyses was distilled 5 times using the all-Teflon Savillex DST-1000 acid purification system.

The schematic processes of the sample pretreatment and column separation are illustrated in **Fig. 2-5**. The foraminifera samples were carefully cracked between glass slides and sonicated to remove clay and dust particles. After drying, each sample was observed under a microscope to check for and remove detrital grains. The foraminifera samples were dissolved in 0.5 M $HNO_3$, as Foster (2008) described. After complete dissolution, 25 µl aliquots were taken out for trace and major element analysis by ICP-MS (**section 2.3.3**).

We separated boron from the sample matrix using the boron-specific exchange resin Amberite IRA 743 (63–120 µm) in a 50 µl microcolumn, following Foster et al. (2008). The samples were loaded in buffered acetic acid (pH 5) and eluted with 0.5 M $HNO_3$. The elution curve was checked several times, and the recovery of boron was 97–102%. The boron isotope ratio was measured using the NuPlasma3 MC-ICPMS at the National Center for Inter-university Research Facilities at Seoul National University. Mass 11 was collected on the H6 Faraday cup equipped with a $10^{-11}$ Ω resistor, and mass 10 was collected on L6 with a $10^{-11}$ Ω resistor.

All samples were analyzed by sample-standard bracketing using NIST SRM 851a as the standard. Blanks were checked before and after each sample and were always <2% of the sample signal (for

~30 ng/g of sample [B], <1 ng blank). The long-term reproducibility was ± 0.28‰ at a 95% confidence interval (**Fig. 2-6**). The column recovery and isotope ratio were confirmed using boron isotope standards NIST SRM 951a ($^{11}B/^{10}B$ = 4.04367; Cantazaro et al., 1970), ERM-AE121 ($\delta^{11}B$ = 19.9 ± 0.6 ‰), ERM-AE122 ($\delta^{11}B$ = 39.7 ± 0.6 ‰), and an in-house carbonate standard PR83, a *Porites* coral from a Micronesia reef ($\delta^{11}B$ = 22.4 ± 0.7 ‰). External reproducibility on $\delta^{11}B$ was calculated following Rae et al. (2011) on repeat analyses of three different boric acid standards (NIST SRM 951a, ERM-AE121, ERM-AE122) (**Fig. 2-6**).

$$2\sigma = 1.58\ \exp^{-17.9[^{11}B]} + 0.24\ \exp^{-0.41[^{11}B]}$$

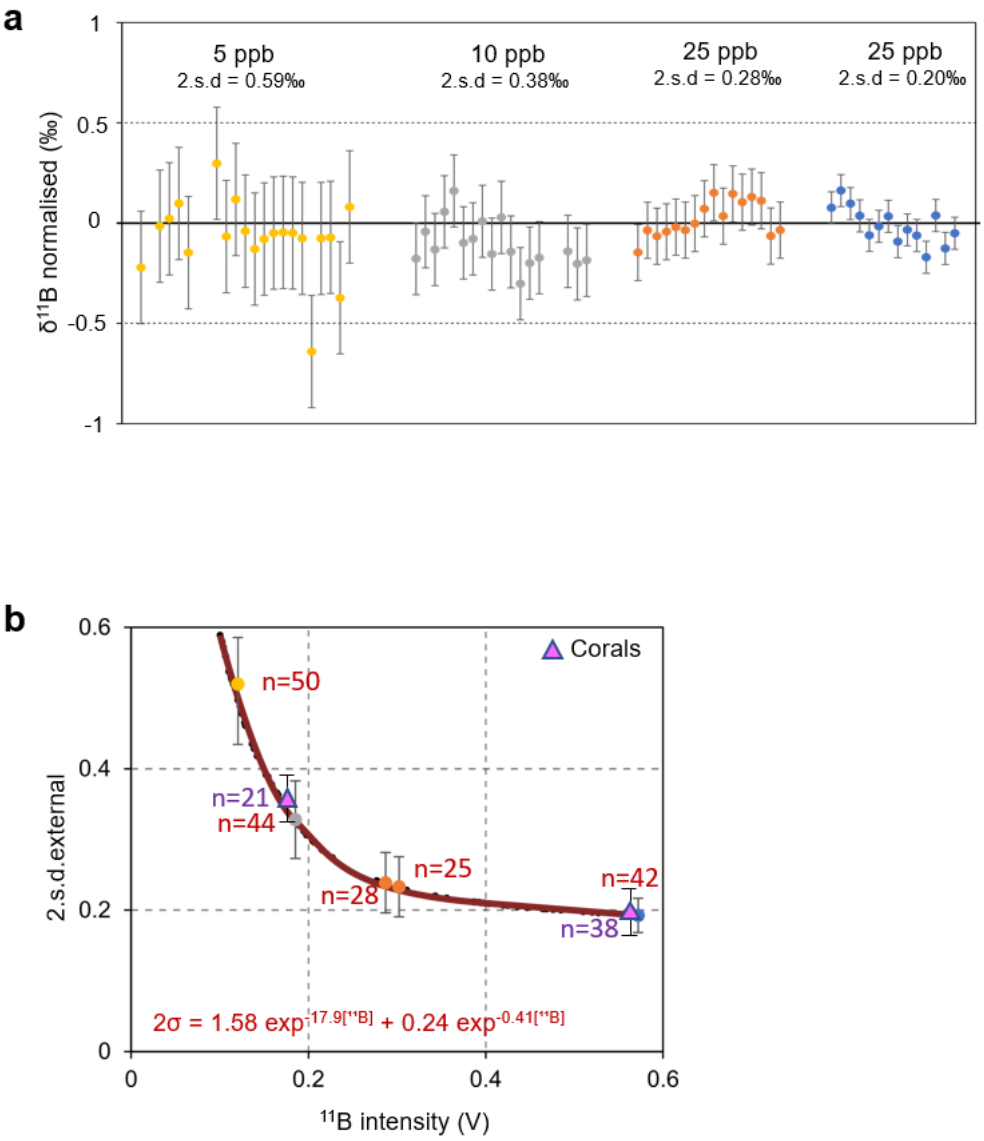


**Figure 2-6.** External reproducibility in long-term analysis.

(a) $\delta^{11}B$ deviation of 3 boric acid standards (NIST SRM 951a, ERM-AE121, ERM-AE122) from various concentration (5 ppb, 10 ppb, 25 ppb, 50 ppb) with 2.s.d external reproducibility. 2.s.e of each internal measurements are shown by error bars. (b) External reproducibility relationship between 11B intensity and 2 s.d of boric acid standards and columned coral in-house standard. 2σ equation is calculated following Rae et al. (2011).

**Table 2-3. Trace element (Ca, Al, Mn, Sr, Al, Ca) and Al/Ca results from ICP-MS analysis, less than 5% Uncertainty.**

| No. | Species and size | Depth (mean, cm) | Age (ka) | Ca (mg/L) | Al (μg/L) | Mn (μg/L) | Sr (μg/L) | Al (μmol) | Ca (mol) | Al/Ca (μmol/mol) |
|---|---|---|---|---|---|---|---|---|---|---|
| 1 | *G.bulloides* 300-355 μm | 20.5 | 12.54 | 0.92 | 14.16 | 0.44 | 2.19 | 0.52 | 0.02 | 22.85 |
| 2 | *G.bulloides* 300-355 μm | 26.5 | 14.86 | 1.17 | 13.17 | 1.03 | 3.05 | 0.49 | 0.03 | 16.68 |
| 3 | *G.bulloides* 300-355 μm | 34.5 | 17.45 | 0.62 | 24.79 | 0.98 | 14.03 | 0.92 | 0.02 | 29.76 |
| 4 | *G.bulloides* 300-355 μm | 36.5 | 17.76 | 0.50 | 27.48 | 1.60 | 10.07 | 1.02 | 0.01 | 41.15 |
| 5 | *G.bulloides* 300-355 μm | 44.5 | 18.64 | 0.72 | 9.08 | 0.35 | 1.49 | 0.34 | 0.02 | 9.35 |
| 6 | *G.bulloides* 300-355 μm | 45.5 | 18.73 | 0.72 | 10.68 | 0.52 | 2.49 | 0.40 | 0.02 | 21.90 |
| 7 | *G.bulloides* 300-355 μm | 47.5 | 18.93 | 1.14 | 11.38 | 1.05 | 3.38 | 0.42 | 0.03 | 14.85 |
| 8 | *G.bulloides* 300-355 μm | 48.5 | 18.96 | 0.62 | 22.99 | 0.42 | 4.23 | 0.85 | 0.02 | 54.71 |
| 9 | *G.bulloides* 300-355 μm | 51.5 | 19.06 | 0.51 | 7.91 | 0.45 | 1.37 | 0.29 | 0.01 | 22.99 |
| 10 | *G.bulloides* 300-355 μm | 54.5 | 19.16 | 1.90 | 17.34 | 0.48 | 6.10 | 0.64 | 0.05 | 13.57 |
| 11 | *G.bulloides* 300-355 μm | 58.5 | 19.48 | 1.52 | 12.29 | 0.60 | 4.24 | 0.46 | 0.04 | 12.05 |
| 12 | *G.bulloides* 300-355 μm | 68.5 | 20.77 | 0.33 | 23.43 | 0.60 | 0.93 | 0.87 | 0.01 | 106.28 |
| 13 | *G.bulloides* 300-355 μm | 72.5 | 21.29 | 1.84 | 22.02 | 0.53 | 5.61 | 0.82 | 0.05 | 17.76 |

**Table 2-3. (Continued) Trace element (Ca, Al, Mn, Sr, Al, Ca) and Al/Ca results.**

| No. | Species and size | Depth (mean, cm) | Age (ka) | Ca (mg/L) | Al (μg/L) | Mn (μg/L) | Sr (μg/L) | Al (μmol) | Ca (mol) | Al/Ca (μmol/mol) |
|---|---|---|---|---|---|---|---|---|---|---|
| 1 | *N.pachyderma*.250-300 μm | 5.5 | 3.36 | 0.46 | 14.14 | 0.42 | 0.80 | 0.52 | 0.01 | 45.36 |
| 2 | *N.pachyderma*.250-300 μm | 10.5 | 6.42 | 0.37 | 20.92 | 0.17 | 0.49 | 0.78 | 0.01 | 84.88 |
| 3 | *N.pachyderma*.250-300 μm | 23.5 | 13.88 | 2.36 | 12.89 | 0.74 | 7.53 | 0.48 | 0.06 | 8.12 |
| 4 | *N.pachyderma*.250-300 μm | 26.5 | 14.86 | 1.53 | 37.42 | 2.20 | 30.98 | 1.39 | 0.04 | 18.13 |
| 5 | *N.pachyderma*.250-300 μm | 30.5 | 16.84 | 0.90 | 34.72 | 1.09 | 18.33 | 1.29 | 0.02 | 28.57 |
| 6 | *N.pachyderma*.250-300 μm | 33.5 | 17.30 | 2.00 | 88.58 | 1.38 | 22.20 | 3.28 | 0.05 | 32.87 |
| 7 | *N.pachyderma*.250-300 μm | 34.5 | 17.45 | 1.84 | 21.17 | 1.43 | 6.00 | 0.78 | 0.05 | 8.56 |
| 8 | *N.pachyderma*.250-300 μm | 36.5 | 17.76 | 1.18 | 20.76 | 1.01 | 11.49 | 0.77 | 0.03 | 13.02 |
| 10 | *N.pachyderma*.250-300 μm | 44.5 | 18.64 | 1.45 | 7.08 | 0.32 | 4.57 | 0.26 | 0.04 | 7.23 |
| 11 | *N.pachyderma*.250-300 μm | 46.5 | 18.83 | 0.99 | 37.30 | 1.11 | 11.00 | 1.38 | 0.02 | 55.97 |
| 12 | *N.pachyderma*.250-300 μm | 48.5 | 18.96 | 1.52 | 22.01 | 0.54 | 3.25 | 0.82 | 0.04 | 21.51 |
| 13 | *N.pachyderma*.250-300 μm | 50.5 | 19.03 | 1.84 | 8.22 | 2.70 | 5.85 | 0.30 | 0.05 | 6.65 |
| 14 | *N.pachyderma*.250-300 μm | 51.5 | 19.06 | 1.32 | 19.84 | 0.47 | 4.40 | 0.74 | 0.03 | 22.27 |
| 15 | *N.pachyderma*.250-300 μm | 52.5 | 19.09 | 0.74 | 3.81 | 0.19 | 2.17 | 0.14 | 0.02 | 7.64 |
| 16 | *N.pachyderma*.250-300 μm | 53.5 | 19.13 | 2.09 | 11.41 | 0.54 | 6.70 | 0.42 | 0.05 | 8.10 |
| 17 | *N.pachyderma*.250-300 μm | 54.5 | 19.16 | 1.72 | 12.25 | 0.50 | 5.50 | 0.45 | 0.04 | 10.60 |
| 18 | *N.pachyderma*.250-300 μm | 55.5 | 19.19 | 2.19 | 65.87 | 1.46 | 6.49 | 2.44 | 0.05 | 44.71 |

**Table 2-3. (Continued) Trace element (Ca, Al, Mn, Sr, Al, Ca) and Al/Ca results.**

| No. | Species and size | Depth (mean, cm) | Age (ka) | Ca (mg/L) | Al (μg/L) | Mn (μg/L) | Sr (μg/L) | Al (μmol) | Ca (mol) | Al/Ca (μmol/mol) |
|---|---|---|---|---|---|---|---|---|---|---|
| 19 | *N.pachyderma.*250-300 μm | 56.5 | 19.23 | 0.49 | 3.44 | 0.24 | 1.01 | 0.13 | 0.01 | 10.36 |
| 20 | *N.pachyderma.*250-300 μm | 58.5 | 19.48 | 2.23 | 14.14 | 0.63 | 7.27 | 0.52 | 0.06 | 9.44 |
| 21 | *N.pachyderma.*250-300 μm | 59.5 | 19.61 | 2.69 | 12.34 | 0.54 | 8.54 | 0.46 | 0.07 | 6.83 |
| 22 | *N.pachyderma.*250-300 μm | 68.5 | 20.77 | 0.91 | 17.57 | 1.33 | 3.14 | 0.65 | 0.02 | 28.57 |
| 23 | *N.pachyderma.*250-300 μm | 72.5 | 21.29 | 1.67 | 19.49 | 0.36 | 5.59 | 0.72 | 0.04 | 17.36 |
| 1 | *T.sacculifer* 425-800 μm | 10.5 | 6.42 | 0.53 | 11.33 | 0.25 | 1.44 | 0.42 | 0.01 | 32.06 |
| 2 | *T.sacculifer* 425-800 μm | 14.5 | 8.87 | 0.80 | 7.76 | 0.27 | 1.83 | 0.29 | 0.02 | 14.32 |
| 3 | *T.sacculifer* 425-800 μm | 20.5 | 12.54 | 1.88 | 15.05 | 0.91 | 5.57 | 0.56 | 0.05 | 11.90 |
| 4 | *T.sacculifer* 425-800 μm | 23.5 | 13.88 | 0.93 | 8.52 | 0.30 | 2.12 | 0.32 | 0.02 | 13.54 |
| 5 | *T.sacculifer* 425-800 μm | 26.5 | 14.86 | 2.45 | 11.12 | 0.59 | 7.39 | 0.41 | 0.06 | 6.74 |
| 6 | *T.sacculifer* 425-800 μm | 30.5 | 16.84 | 2.17 | 68.47 | 2.07 | 20.10 | 2.54 | 0.05 | 23.39 |
| 7 | *T.sacculifer* 425-800 μm | 33.5 | 17.30 | 1.16 | 61.70 | 1.29 | 4.48 | 2.29 | 0.03 | 39.40 |
| 8 | *T.sacculifer* 425-800 μm | 34.5 | 17.45 | 1.32 | 38.41 | 1.69 | 31.21 | 1.42 | 0.03 | 21.63 |
| 9 | *T.sacculifer* 425-800 μm | 36.5 | 17.76 | 39.52 | 52.42 | 4.26 | 79.25 | 1.94 | 0.99 | 0.99 |
| 10 | *T.sacculifer* 425-800 μm | 44.5 | 18.64 | 1.28 | 20.27 | 0.67 | 3.38 | 0.75 | 0.03 | 11.72 |
| 11 | *T.sacculifer* 425-800 μm | 50.5 | 19.03 | 0.96 | 14.86 | 0.29 | 2.67 | 0.55 | 0.02 | 23.07 |
| 12 | *T.sacculifer* 425-800 μm | 51.5 | 19.06 | 1.04 | 10.48 | 0.34 | 2.98 | 0.39 | 0.03 | 15.02 |
| 13 | *T.sacculifer* 425-800 μm | 53.5 | 19.13 | 1.50 | 7.21 | 0.41 | 4.49 | 0.27 | 0.04 | 7.16 |

**Table 2-3. (Continued) Trace element (Ca, Al, Mn, Sr, Al, Ca) and Al/Ca results.**

| No. | Species and size | Depth (mean, cm) | Age (ka) | Ca (mg/L) | Al (µg/L) | Mn (µg/L) | Sr (µg/L) | Al (µmol) | Ca (mol) | Al/Ca (µmol/mol) |
|---|---|---|---|---|---|---|---|---|---|---|
| 14 | *T.sacculifer* 425-800 µm | 54.5 | 19.16 | 0.93 | 71.25 | 0.50 | 3.53 | 2.64 | 0.02 | 114.10 |
| 15 | *T.sacculifer* 425-800 µm | 56.5 | 19.23 | 0.66 | 16.71 | 0.36 | 1.96 | 0.62 | 0.02 | 37.80 |
| 16 | *T.sacculifer* 425-800 µm | 58.5 | 19.48 | 2.65 | 12.60 | 0.95 | 7.95 | 0.47 | 0.07 | 7.07 |
| 17 | *T.sacculifer* 425-800 µm | 60.5 | 19.74 | 2.93 | 20.66 | 0.88 | 9.13 | 0.77 | 0.07 | 10.47 |
| 18 | *T.sacculifer* 425-800 µm | 68.5 | 20.77 | 1.45 | 13.27 | 0.25 | 4.25 | 0.49 | 0.04 | 13.63 |

### 2.3.3. Trace element analyses

Major and trace elements were analyzed for Ca, Mg, Al, Mn, and Sr by Elan DRC-II ICPMS at Korea Basic Science Institute (KBSI) Seoul Center. The uncertainty was less than 5% for all elements. Conventionally, samples with Al/Ca > 120 μmol/mol are considered to be contaminated by detrital minerals (Foster, 2008; Kubota et al., 2021) and not considered further. Most of the samples in this study had Al/Ca below ~ 40 μmol/mol, and even the 15 samples that had Al/Ca between 40 and 120 μmol/mol showed concentrations of the other trace elements in the typical range (**Table 2-3**).

### 2.3.4. Carbonate system calculations

The $\delta^{11}B_{calcite}$ of foraminifera was converted into $\delta^{11}B_{borate}$, the boron isotope ratio of the borate ion in the seawater in which the foraminifera grew. The species-specific calibration equations based on sediment trap, core top, and culture studies were taken from literature and uppermost core top samples from NPGM1302-1B (**Table 2-4**).

To calculate the pH from $\delta^{11}B_{borate}$ data, we first need estimates of sea surface temperature (SST), sea surface salinity (SSS), pressure, and total alkalinity (TA) to calculate the $pK_B^*$. Past SST was calculated from the $\delta^{18}O$ difference between the benthic and planktonic foraminifera and past SSS from planktonic $\delta^{18}O$. We used $\delta^{18}O$ data of Seo et al. (2018) and the relationships established in the northwest Pacific for the post-LGM period.

$$SST = 0.331 \cdot \Delta(\delta^{18}O_{benthic} - \delta^{18}O_{planktonic})^2 + 3.643 \cdot \Delta(\delta^{18}O_{benthic} - \delta^{18}O_{planktonic}) - 0.14$$

$$SSS = (\delta^{18}O_{planktonic} + 17.955) / 0.521$$

In this study, $\delta^{18}O$ from *G. ruber* was considered as the surface record (0 to 25 m), and the *N. incompta* was regarded as the lower thermocline (~50 to 100 m) record (**Table 2-5, Table 2-6**). This empirical estimate of SST and SSS in the Kuroshio extension agrees with modern measured values (SST = ± 0.37 ℃, SSS = ± 0.7 psu)(Oba and Murayama, 2004). When the calculated SST for our core is compared with the alkenone-derived SST for a core nearby (Station 6) (Harada et al., 2004), the amount of temperature change from the LGM to the Holocene is similar (~ 6 ℃). Another noteworthy point is that the restored SST and SSS values are similar to the average range of the seasonal depth profile in the modern study area (**Fig 2-2**). Due to the timescale characteristics of this study, a correction for a 2.5 °C drop in deep water temperature was applied in the calculation of SST from 5.5 ka to 20 ka. Calculated SST and SSS were in the range of modern seasonally-averaged values in the northwest Pacific (SST < 20℃ at ~100 m water depth, 33 < SSS < 35 PSU; (Ishii et al., 2011).

Total alkalinity was calculated using the estimated SST and SSS and the relationship (equation 4) for our core location in the North Pacific, including a longitude correction (Lee et al., 2006).

$$TA = 2305 + 53.23 \cdot (SSS - 35) + 1.85 \cdot (SSS - 35)^2 - 14.72 \cdot (SST - 20) - 0.158 \cdot (SST-20)^2 + 0.062 \cdot (SST - 20)$$

The calculated TA was in the range of 2298 - 2389 μeq $kg^{-1}$, which is higher than the modern seasonal range observed further west along the Kuroshio Extension (31-34 ºN, 137 ºE; 2290 μeq $kg^{-1}$

< TA < 2320 μeq $kg^{-1}$; Ishii et al., 2011). we considered that the present KE area also has a higher TA (~2350 μmol $kg^{-1}$) than the surrounding area, and these high TA appeared in the pelagic transition zone, especially in longitude 150-180°E of North Hemisphere Pacific (Lee et al., 2006). TA uncertainty in pH, $pCO_2$ realizations contains the glacial alkalinity increase (± 125 μmol $kg^{-1}$) those estimated in the modeling studies (Hain et al., 2015; Toggweiler, 1999). SST, SSS, and TA datasets were used to determine the $pK_B^*$ value of each sample (Zeebe & Wolf-Gladrow, 2001).

To convert $\delta^{11}B_{borate}$ to pH, the seawater $\delta^{11}B$ value of 39.61‰ (Foster et al., 2010) and the fractionation factor $\alpha_B$ of 1.0272 (Zeebe & Wolf-Gladrow, 2001) were substituted in the following equation (Foster and Rae, 2016; Vengosh et al., 1991).

$$pH = pK_B^* - \log\left(-\frac{\delta^{11}B_{seawater} - \delta^{11}B_{borate}}{\delta^{11}B_{seawater} - (\alpha B \times \delta^{11}B_{borate}) - 1000 \times (\alpha B - 1)}\right)$$

The uncertainty of each pH data point was fully propagated with 10,000 realizations of the Monte Carlo approach and was ±0.097 on average (**Table 2-7**). The $pCO_{2,sw}$ was calculated using the *seacarb* package (Gattuso et al., 2017) in R using the T, S, TA, and pH as input variables. The uncertainty was fully propagated using the Monte Carlo approach with 10,000 realizations varying the SST, sea surface salinity (SSS), and TA (**Table 2-7**). The estimated uncertainty of this approach was ± 42 μatm.

**Table 2-4.** $\delta^{11}B$ data from coretop foraminiferal calcite, comparison with variables and calibrated results.

| core/species | coretop study locations[a] | depth for T,S ([b]GLODAP) (m) | T (°C) | S (psu) | pH (Total) | $pK_B^*$ | $\delta^{11}B_{calcite}$ (‰) | $\delta^{11}B_{borate}$ (‰) | $\delta^{11}B_{calcite}$ by calibration[a] (‰) | $\delta^{11}B_{calcite}$ uncertainty by calibration (1 sd) (‰) |
|---|---|---|---|---|---|---|---|---|---|---|
| NPGM1302-1B, 0-1cm, *G.bulloides* | East Equatorial Pacific | 9.9 | 27.72 | 34.4 | 8.17 | 8.57 | 18.33 | 19.77 | 17.68 | 0.65 |
| NPGM1302-1B, 0-1cm, *N.pachyderma* | North Pacific | 9.9 | 27.72 | 34.4 | 8.17 | 8.57 | 16.87 | 19.77 | 16.39 | 0.48 |
| NPGM1302-1B, 0-1cm, *T.sacculifer* | East Equatorial Pacific | 101 | 21.10 | 34.8 | 8.08 | 8.64 | 18.53 | 17.84 | 18.57 | 0.04 |

[a]Refitted data and calibrations Henehan et al., (2016)

[b]Station 48292 in GLODAP data (Key et al., 2004); 155.04°E 32.001°N

**Table 2-5.** Reconstructed surface (0-50m) temperature, salinity, alkalinity from $\delta^{18}O_{G.ruber}$ and $\delta^{18}O_{Uvigerina\ spp.}$

| Age (ka) | $\Delta^{18}O_{Uvigerina\text{-}G.ruber}$ (‰) | [a]T by $\Delta^{18}O$ (Surface; ℃) | [a]1s (Surface; ℃) | [b]S by $\delta^{18}O_{G.\ ruber}$ (Surface; psu) | [b]1s (Surface; psu) | [c]Total alkalinity (Surface; μmol $kg^{-1}$) | [c]1s (Surface; μmol $kg^{-1}$) |
|---|---|---|---|---|---|---|---|
| 0.69 | 3.9 | 18.9 | 0.37 | 34 | 1 | 2267 | 9 |
| 1.91 | 3.4 | 16.2 | 0.37 | 35 | 1 | 2342 | 9 |
| 3.12 | 5.1 | 26.8 | 0.37 | 33 | 1 | 2098 | 9 |
| 4.34 | 4.3 | 21.9 | 0.37 | 31 | 1 | 2094 | 9 |
| 5.55 | 4.3 | 21.9 | 0.37 | 32 | 1 | 2154 | 9 |
| 7.98 | 4.4 | 20.3 | 0.37 | 33 | 1 | 2211 | 9 |
| 9.20 | 4.5 | 19.5 | 0.37 | 33 | 1 | 2202 | 9 |
| 10.41 | 4.5 | 18.7 | 0.37 | 35 | 1 | 2297 | 9 |
| 11.63 | 5.3 | 23.3 | 0.37 | 33 | 1 | 2139 | 9 |
| 12.84 | 5.8 | 26.9 | 0.37 | 32 | 1 | 2073 | 9 |
| 13.11 | 5.1 | 22.4 | 0.37 | 33 | 1 | 2188 | 9 |
| 13.37 | 5.2 | 23.2 | 0.37 | 33 | 1 | 2175 | 9 |
| 13.63 | 6.2 | 30.1 | 0.37 | 34 | 1 | 2068 | 9 |
| 13.90 | 5.6 | 25.9 | 0.37 | 34 | 1 | 2141 | 9 |
| 14.88 | 5.2 | 23.2 | 0.37 | 34 | 1 | 2211 | 9 |

*$\Delta^{18}O$: $\delta^{18}O$ defference between benthic - planktonic foraminifera. $\delta^{18}O$ values from specific foraminifera data from Seo et al., (2018)

[a]T: Temperature based on Oba and Murayama (2004); $T= 0.331 \times \Delta(\delta^{18}O_{Uvigerina\ spp.} - \delta^{18}O_{G.ruber})^2 + 3.643 \times \Delta(\delta^{18}O_{Uvigerina\ spp.} - \delta^{18}O_{G.ruber}) - 0.14$

[b]S: Salinity based on Oba and Murayama (2004); $S= (\delta^{18}O_{G.ruber} + 17.955) / 0.521$

[c]TA: Alkalinity based on Lee et al., (2006); $TA= 2305 + 53.23 \times (S - 35) + 1.85 \times (S - 35)2 -14.72 \times (T - 20) - 0.158 \times (T-20)2 + 0.062 \times (T - 20)$

**Table 2-5.** (Continued)

| Age (ka) | $\Delta^{18}O_{Uvigerina\text{-}G.ruber}$ (‰) | [a]T by $\Delta^{18}O$ (Surface; ℃) | [a]1s (Surface; ℃) | [b]S by $\delta^{18}O_{G.\ ruber}$ (Surface; psu) | [b]1s (Surface; psu) | [c]Total alkalinity (Surface; μmol $kg^{-1}$) | [c]1s (Surface; μmol $kg^{-1}$) |
|---|---|---|---|---|---|---|---|
| 15.86 | 4.8 | 20.6 | 0.37 | 35 | 1 | 2280 | 9 |
| 16.85 | 4.4 | 18.0 | 0.37 | 35 | 1 | 2348 | 9 |
| 17.83 | 4.0 | 15.3 | 0.37 | 36 | 1 | 2415 | 9 |
| 17.99 | 4.5 | 18.2 | 0.37 | 35 | 1 | 2321 | 9 |
| 18.15 | 4.7 | 19.5 | 0.37 | 35 | 1 | 2286 | 9 |
| 18.31 | 4.4 | 17.6 | 0.37 | 35 | 1 | 2344 | 9 |
| 18.47 | 4.9 | 20.8 | 0.37 | 34 | 1 | 2256 | 9 |
| 18.97 | 4.0 | 15.2 | 0.37 | 36 | 1 | 2408 | 9 |
| 19.20 | 4.9 | 20.7 | 0.37 | 34 | 1 | 2242 | 9 |
| 19.42 | 4.6 | 18.8 | 0.37 | 35 | 1 | 2328 | 9 |
| 19.43 | 4.7 | 20.0 | 0.37 | 35 | 1 | 2287 | 9 |
| 19.49 | 4.4 | 17.8 | 0.37 | 35 | 1 | 2348 | 9 |
| 19.62 | 4.3 | 17.0 | 0.37 | 35 | 1 | 2360 | 9 |
| 19.74 | 5.1 | 22.4 | 0.37 | 34 | 1 | 2204 | 9 |
| 19.99 | 4.0 | 15.5 | 0.37 | 35 | 1 | 2391 | 9 |

*$\Delta^{18}O$: $\delta^{18}O$ defference between benthic - planktonic foraminifera. $\delta^{18}O$ values from specific foraminifera data from Seo et al., (2018)

[a]T: Temperature based on Oba and Murayama (2004); $T= 0.331 \times \Delta(\delta^{18}O_{Uvigerina\ spp.} - \delta^{18}O_{G.ruber})^2 + 3.643 \times \Delta(\delta^{18}O_{Uvigerina\ spp.} - \delta^{18}O_{G.ruber}) - 0.14$

[b]S: Salinity based on Oba and Murayama (2004); $S= (\delta^{18}O_{G.ruber} + 17.955) / 0.521$

[c]TA: Alkalinity based on Lee et al., (2006); $TA= 2305 + 53.23 \times (S - 35) + 1.85 \times (S - 35)2 -14.72 \times (T - 20) - 0.158 \times (T-20)2 + 0.062 \times (T - 20)$

**Table 2-6.** Reconstructed lower thermocline (~100 m) temperature, salinity, alkalinity from $\delta^{18}O_{N.incompta}$ and $\delta^{18}O_{Uvigerina\ spp.}$

| Age (ka) | $\Delta^{18}O_{Uvigerina\text{-}N.incompta}$ (‰) | [a]T by $\Delta^{18}O$ (thermocline; ℃) | [a]1s (thermocline; ℃) | [b]S by $\delta^{18}O_{N.incompta}$ (thermocline; psu) | [b]1s (thermocline; psu) | [c]Total alkalinity (thermocline; μmol $kg^{-1}$) | [c]1s (thermocline; μmol $kg^{-1}$) |
|---|---|---|---|---|---|---|---|
| 0.69 | 3.2 | 15.1 | 0.37 | 35.2 | 0.70 | 2383 | 9 |
| 1.91 | 3.1 | 14.2 | 0.37 | 35.4 | 0.70 | 2404 | 9 |
| 3.12 | 3.9 | 19.2 | 0.37 | 35.2 | 0.70 | 2329 | 9 |
| 4.34 | 2.4 | 10.3 | 0.37 | 34.8 | 0.70 | 2423 | 9 |
| 5.55 | 3.2 | 15.0 | 0.37 | 34.7 | 0.70 | 2357 | 9 |
| 7.98 | 3.4 | 16.2 | 0.37 | 35.4 | 0.70 | 2379 | 9 |
| 9.20 | 3.5 | 16.8 | 0.37 | 35.4 | 0.70 | 2371 | 9 |
| 10.41 | 3.6 | 17.4 | 0.37 | 36.3 | 0.70 | 2413 | 9 |
| 11.63 | 3.4 | 16.2 | 0.37 | 36.1 | 0.70 | 2419 | 9 |
| 12.84 | 3.8 | 14.6 | 0.37 | 36.2 | 0.70 | 2446 | 9 |
| 13.11 | 3.8 | 14.1 | 0.37 | 36.0 | 0.70 | 2440 | 9 |
| 13.37 | 3.2 | 11.2 | 0.37 | 37.2 | 0.70 | 2549 | 9 |
| 13.63 | 4.7 | 19.5 | 0.37 | 36.6 | 0.70 | 2402 | 9 |
| 13.90 | 4.0 | 15.6 | 0.37 | 36.7 | 0.70 | 2459 | 9 |
| 14.88 | 3.8 | 14.3 | 0.37 | 36.9 | 0.70 | 2490 | 9 |

*$\Delta^{18}O$: $\delta^{18}O$ defference between benthic - planktonic foraminifera. $\delta^{18}O$ values from specific foraminifera data from Seo et al., (2018)

[a]T: Temperature based on Oba and Murayama (2004); $T= 0.331 \times \Delta(\delta^{18}O_{Uvigerina\ spp.} - \delta^{18}O_{N.incompta})^2 + 3.643 \times \Delta(\delta^{18}O_{Uvigerina\ spp.} - \delta^{18}O_{N.incompta}) - 0.14$

[b]S: Salinity based on Oba and Murayama (2004); $S= (\delta^{18}O_{N.incompta} + 17.955) / 0.521$

[c]TA: Alkalinity based on Lee et al., (2006); TA= 2305 + 53.23 x (S - 35) + 1.85 x (S - 35)2 -14.72 x (T - 20) - 0.158 x (T-20)2 + 0.062 x (T - 20)

**Table 2-6.** (Continued)

| Age (ka) | $\Delta^{18}O_{Uvigerina\text{-}N.incompta}$ (‰) | [a]T by $\Delta^{18}O$ (thermocline; ℃) | [a]1s (thermocline; ℃) | [b]S by $\delta^{18}O_{N.incompta}$ (thermocline; psu) | [b]1s (thermocline; psu) | [c]Total alkalinity (thermocline; μmol $kg^{-1}$) | [c]1s (thermocline; μmol $kg^{-1}$) |
|---|---|---|---|---|---|---|---|
| 15.86 | 3.5 | 13.0 | 0.37 | 37.1 | 0.70 | 2520 | 9 |
| 16.85 | 3.3 | 11.7 | 0.37 | 37.3 | 0.70 | 2550 | 9 |
| 17.83 | 3.1 | 10.4 | 0.37 | 37.6 | 0.70 | 2580 | 9 |
| 17.99 | 3.0 | 9.8 | 0.37 | 37.6 | 0.70 | 2592 | 9 |
| 18.15 | 3.4 | 12.1 | 0.37 | 36.9 | 0.70 | 2521 | 9 |
| 18.31 | 3.1 | 10.5 | 0.37 | 37.5 | 0.70 | 2575 | 9 |
| 18.47 | 3.0 | 9.8 | 0.37 | 37.9 | 0.70 | 2610 | 9 |
| 18.97 | 3.5 | 12.7 | 0.37 | 36.5 | 0.70 | 2488 | 9 |
| 19.20 | 3.2 | 11.2 | 0.37 | 37.1 | 0.70 | 2540 | 9 |
| 19.42 | 3.2 | 11.2 | 0.37 | 37.6 | 0.70 | 2575 | 9 |
| 19.43 | 3.6 | 13.1 | 0.37 | 36.9 | 0.70 | 2505 | 9 |
| 19.49 | 3.5 | 12.9 | 0.37 | 36.8 | 0.70 | 2506 | 9 |
| 19.62 | 3.2 | 11.2 | 0.37 | 37.2 | 0.70 | 2547 | 9 |
| 19.74 | 3.6 | 13.4 | 0.37 | 36.5 | 0.70 | 2481 | 9 |
| 19.86 | 4.2 | 16.7 | 0.37 | 37.0 | 0.70 | 2465 | 9 |
| 19.99 | 3.3 | 11.4 | 0.37 | 36.9 | 0.70 | 2527 | 9 |

*$\Delta^{18}O$: $\delta^{18}O$ defference between benthic - planktonic foraminifera. $\delta^{18}O$ values from specific foraminifera data from Seo et al., (2018)

[a]T: Temperature based on Oba and Murayama (2004); $T= 0.331 \times \Delta(\delta^{18}O_{Uvigerina\ spp.} - \delta^{18}O_{N.incompta})^2 + 3.643 \times \Delta(\delta^{18}O_{Uvigerina\ spp.} - \delta^{18}O_{N.incompta}) - 0.14$

[b]S: Salinity based on Oba and Murayama (2004); $S= (\delta^{18}O_{N.incompta} + 17.955) / 0.521$

[c]TA: Alkalinity based on Lee et al., (2006); TA= 2305 + 53.23 x (S - 35) + 1.85 x (S - 35)2 -14.72 x (T - 20) - 0.158 x (T-20)2 + 0.062 x (T - 20)

**Table 2-7.** $\delta^{11}B_{calcite}$ of planktonic foraminifera and variables for carbonate chemistry calculation

| No. | Species | Depth (mean, cm) | Age (ka) | $\delta^{11}B_{calcite}$ (‰) | 1s (‰) | T (℃) | S (psu) | Total alkalinity (μmol $kg^{-1}$) | $pK_B$ | pH (total) | 1s (total) | seawater $pCO_2$ (μatm) | 1s (μatm) | $\Delta pCO_2$ (μatm) | 1s (μatm) |
|---|---|---|---|---|---|---|---|---|---|---|---|---|---|---|---|
| 1 | *G.bulloides* | 20.5 | 12.54 | 15.77 | 0.32 | 25.1 | 32.5 | 2107 | 8.61 | 8.05 | 0.02 | 271 | 20 | 24 | 20 |
| 2 | *G.bulloides* | 26.5 | 14.86 | 16.89 | 0.3 | 15.3 | 35.8 | 2415 | 8.71 | 8.17 | 0.02 | 201 | 16 | -32 | 16 |
| 3 | *G.bulloides* | 34.5 | 17.45 | 16.85 | 0.35 | 18.2 | 34.8 | 2321 | 8.68 | 8.15 | 0.02 | 217 | 18 | 25 | 18 |
| 4 | *G.bulloides* | 36.5 | 17.76 | 17.79 | 0.44 | 18.2 | 34.8 | 2321 | 8.68 | 8.21 | 0.02 | 195 | 18 | 3 | 18 |
| 5 | *G.bulloides* | 44.5 | 18.64 | 16.42 | 0.42 | 17.9 | 34.8 | 2325 | 8.68 | 8.09 | 0.02 | 239 | 17 | 48 | 17 |
| 6 | *G.bulloides* | 45.5 | 18.73 | 17.4 | 0.4 | 17.9 | 34.8 | 2325 | 8.68 | 8.18 | 0.02 | 207 | 19 | 15 | 19 |
| 7 | *G.bulloides* | 47.5 | 18.93 | 16.97 | 0.4 | 17.9 | 34.8 | 2325 | 8.68 | 8.15 | 0.02 | 214 | 18 | 24 | 18 |
| 8 | *G.bulloides* | 48.5 | 18.96 | 16.69 | 0.38 | 20.7 | 34.0 | 2242 | 8.65 | 8.13 | 0.02 | 225 | 18 | 33 | 18 |
| 9 | *G.bulloides* | 51.5 | 19.06 | 17.91 | 0.4 | 20.0 | 34.4 | 2274 | 8.66 | 8.23 | 0.02 | 181 | 16 | -11 | 16 |
| 10 | *G.bulloides* | 54.5 | 19.16 | 16.7 | 0.34 | 20.0 | 34.4 | 2274 | 8.66 | 8.14 | 0.02 | 224 | 19 | 33 | 19 |
| 11 | *G.bulloides* | 58.5 | 19.48 | 16.82 | 0.34 | 18.5 | 35.2 | 2338 | 8.67 | 8.15 | 0.02 | 210 | 17 | 20 | 17 |
| 12 | *G.bulloides* | 68.5 | 20.77 | 18.4 | 0.26 | 15.5 | 34.9 | 2360 | 8.71 | 8.22 | 0.02 | 190 | 21 | -1 | 21 |
| 13 | *G.bulloides* | 72.5 | 21.29 | 17.62 | 0.29 | 15.5 | 34.9 | 2360 | 8.71 | 8.21 | 0.02 | 205 | 18 | 17 | 18 |

**Table 2-7.** (Continued)

| No. | Species | Depth (mean, cm) | Age (ka) | $\delta^{11}B_{calcite}$ (‰) | 1s (‰) | T (°C) | S (psu) | Total alkalinity (μmol $kg^{-1}$) | $pK_B$ | pH (total) | 1s (total) | seawater $pCO_2$ (μatm) | 1s (μatm) | $\Delta pCO_2$ (μatm) | 1s (μatm) |
|---|---|---|---|---|---|---|---|---|---|---|---|---|---|---|---|
| 1 | *N.pachyderma* | 5.5 | 3.36 | 15.43 | 0.3 | 26.8 | 33.0 | 2098 | 8.59 | 8.12 | 0.02 | 266 | 22 | -8 | 22 |
| 2 | *N.pachyderma* | 10.5 | 6.42 | 15.12 | 0.29 | 21.8 | 34.5 | 2250 | 8.64 | 8.08 | 0.02 | 268 | 24 | 6 | 24 |
| 3 | *N.pachyderma* | 23.5 | 13.88 | 16.32 | 0.31 | 18.0 | 35.3 | 2348 | 8.68 | 8.19 | 0.02 | 216 | 23 | -22 | 23 |
| 4 | *N.pachyderma* | 26.5 | 14.86 | 15.35 | 0.32 | 15.3 | 35.8 | 2415 | 8.71 | 8.11 | 0.02 | 260 | 25 | 27 | 25 |
| 5 | *N.pachyderma* | 30.5 | 16.84 | 15.18 | 0.35 | 18.2 | 34.8 | 2321 | 8.68 | 8.11 | 0.02 | 251 | 22 | 46 | 22 |
| 6 | *N.pachyderma* | 33.5 | 17.30 | 16.65 | 0.34 | 18.2 | 34.8 | 2321 | 8.68 | 8.24 | 0.02 | 181 | 18 | -14 | 18 |
| 7 | *N.pachyderma* | 34.5 | 17.45 | 15.25 | 0.35 | 18.2 | 34.8 | 2321 | 8.68 | 8.11 | 0.02 | 245 | 21 | 53 | 21 |
| 8 | *N.pachyderma* | 36.5 | 17.76 | 15.88 | 0.41 | 18.2 | 34.8 | 2321 | 8.68 | 8.15 | 0.02 | 222 | 19 | 31 | 19 |
| 10 | *N.pachyderma* | 44.5 | 18.64 | 15.3 | 0.41 | 17.9 | 34.8 | 2325 | 8.68 | 8.10 | 0.02 | 265 | 25 | 74 | 25 |
| 11 | *N.pachyderma* | 46.5 | 18.83 | 17.05 | 0.38 | 17.9 | 34.8 | 2325 | 8.68 | 8.26 | 0.02 | 213 | 28 | 24 | 28 |
| 12 | *N.pachyderma* | 48.5 | 18.96 | 15.44 | 0.38 | 20.7 | 34.0 | 2242 | 8.65 | 8.13 | 0.02 | 237 | 21 | 46 | 21 |
| 13 | *N.pachyderma* | 50.5 | 19.03 | 15.16 | 0.4 | 20.0 | 34.4 | 2274 | 8.66 | 8.09 | 0.02 | 266 | 24 | 74 | 24 |

**Table 2-7.** (Continued)

| No. | Species | Depth (mean, cm) | Age (ka) | $\delta^{11}B_{calcite}$ (‰) | 1s (‰) | T (°C) | S (psu) | Total alkalinity (μmol $kg^{-1}$) | $pK_B$ | pH (total) | 1s (total) | seawater $pCO_2$ (μatm) | 1s (μatm) | $\Delta pCO_2$ (μatm) | 1s (μatm) |
|---|---|---|---|---|---|---|---|---|---|---|---|---|---|---|---|
| 14 | *N.pachyderma* | 51.5 | 19.06 | 16.96 | 0.41 | 20.0 | 34.4 | 2274 | 8.66 | 8.25 | 0.02 | 199 | 24 | 7 | 24 |
| 15 | *N.pachyderma* | 52.5 | 19.09 | 15.92 | 0.41 | 20.0 | 34.4 | 2274 | 8.66 | 8.16 | 0.02 | 238 | 25 | 46 | 25 |
| 16 | *N.pachyderma* | 53.5 | 19.13 | 15.52 | 0.42 | 20.0 | 34.4 | 2274 | 8.66 | 8.12 | 0.02 | 259 | 25 | 67 | 25 |
| 17 | *N.pachyderma* | 54.5 | 19.16 | 15.49 | 0.35 | 20.0 | 34.4 | 2274 | 8.66 | 8.14 | 0.02 | 241 | 23 | 50 | 23 |
| 18 | *N.pachyderma* | 55.5 | 19.19 | 15.15 | 0.33 | 18.8 | 35.1 | 2328 | 8.67 | 8.12 | 0.02 | 234 | 19 | 43 | 19 |
| 19 | *N.pachyderma* | 56.5 | 19.23 | 15.12 | 0.33 | 19.4 | 34.9 | 2307 | 8.66 | 8.10 | 0.02 | 231 | 16 | 40 | 16 |
| 20 | *N.pachyderma* | 58.5 | 19.48 | 15.96 | 0.3 | 18.5 | 35.2 | 2338 | 8.67 | 8.20 | 0.02 | 204 | 20 | 13 | 20 |
| 21 | *N.pachyderma* | 59.5 | 19.61 | 15.58 | 0.32 | 22.4 | 33.7 | 2204 | 8.64 | 8.16 | 0.02 | 220 | 20 | 30 | 20 |
| 22 | *N.pachyderma* | 68.5 | 20.77 | 16.23 | 0.26 | 15.5 | 34.9 | 2360 | 8.71 | 8.17 | 0.02 | 180 | 20 | -11 | 20 |
| 23 | *N.pachyderma* | 72.5 | 21.29 | 16.78 | 0.25 | 15.5 | 34.9 | 2360 | 8.71 | 8.22 | 0.02 | 192 | 17 | 4 | 17 |
| 1 | *T.sacculifer* | 10.5 | 6.42 | 18.61 | 0.2 | 14.7 | 35.0 | 2381 | 8.72 | 8.07 | 0.02 | 262 | 22 | 0 | 22 |
| 2 | *T.sacculifer* | 14.5 | 8.87 | 20.05 | 0.32 | 14.4 | 35.5 | 2409 | 8.72 | 8.13 | 0.02 | 216 | 22 | -44 | 22 |
| 3 | *T.sacculifer* | 20.5 | 12.54 | 18.45 | 0.31 | 13.4 | 36.2 | 2458 | 8.73 | 8.02 | 0.02 | 291 | 21 | 43 | 21 |
| 4 | *T.sacculifer* | 23.5 | 13.88 | 19.36 | 0.31 | 11.7 | 37.3 | 2550 | 8.75 | 8.10 | 0.02 | 235 | 20 | -4 | 20 |

**Table 2-7.** (Continued)

| No. | Species | Depth (mean, cm) | Age (ka) | $\delta^{11}B_{calcite}$ (‰) | 1s (‰) | T (°C) | S (psu) | Total alkalinity (μmol $kg^{-1}$) | $pK_B$ | pH (total) | 1s (total) | seawater $pCO_2$ (μatm) | 1s (μatm) | $\Delta pCO_2$ (μatm) | 1s (μatm) |
|---|---|---|---|---|---|---|---|---|---|---|---|---|---|---|---|
| 5 | *T.sacculifer* | 26.5 | 14.86 | 19.19 | 0.29 | 10.4 | 37.6 | 2580 | 8.76 | 8.11 | 0.02 | 249 | 24 | 16 | 24 |
| 6 | *T.sacculifer* | 30.5 | 16.84 | 18.24 | 0.34 | 9.8 | 37.6 | 2592 | 8.77 | 8.01 | 0.02 | 330 | 30 | 125 | 30 |
| 7 | *T.sacculifer* | 33.5 | 17.30 | 19.97 | 0.36 | 9.8 | 37.6 | 2592 | 8.77 | 8.09 | 0.02 | 192 | 20 | -4 | 20 |
| 8 | *T.sacculifer* | 34.5 | 17.45 | 19.17 | 0.34 | 9.8 | 37.6 | 2592 | 8.77 | 8.09 | 0.02 | 219 | 15 | 27 | 15 |
| 9 | *T.sacculifer* | 36.5 | 17.76 | 19.56 | 0.39 | 9.8 | 37.6 | 2592 | 8.77 | 8.10 | 0.02 | 222 | 25 | 31 | 25 |
| 10 | *T.sacculifer* | 44.5 | 18.64 | 18.95 | 0.4 | 12.0 | 36.8 | 2514 | 8.75 | 8.08 | 0.02 | 286 | 28 | 95 | 28 |
| 11 | *T.sacculifer* | 50.5 | 19.03 | 18.51 | 0.39 | 11.7 | 37.2 | 2540 | 8.75 | 8.03 | 0.02 | 273 | 17 | 81 | 17 |
| 12 | *T.sacculifer* | 51.5 | 19.06 | 18.67 | 0.4 | 11.7 | 37.2 | 2540 | 8.75 | 8.04 | 0.02 | 290 | 24 | 98 | 24 |
| 13 | *T.sacculifer* | 53.5 | 19.13 | 18.57 | 0.4 | 11.7 | 37.2 | 2540 | 8.75 | 8.03 | 0.02 | 284 | 19 | 92 | 19 |
| 14 | *T.sacculifer* | 54.5 | 19.16 | 19.14 | 0.39 | 11.7 | 37.2 | 2540 | 8.75 | 8.05 | 0.02 | 235 | 17 | 44 | 17 |
| 15 | *T.sacculifer* | 56.5 | 19.23 | 18.34 | 0.28 | 12.1 | 37.3 | 2540 | 8.74 | 8.05 | 0.02 | 258 | 15 | 67 | 15 |
| 16 | *T.sacculifer* | 58.5 | 19.48 | 18.9 | 0.37 | 11.7 | 36.8 | 2520 | 8.75 | 8.09 | 0.02 | 259 | 22 | 69 | 22 |
| 17 | *T.sacculifer* | 60.5 | 19.74 | 19.9 | 0.22 | 16.7 | 37.0 | 2465 | 8.69 | 8.16 | 0.02 | 226 | 30 | 33 | 30 |
| 18 | *T.sacculifer* | 68.5 | 20.77 | 20.27 | 0.24 | 9.9 | 36.4 | 2512 | 8.77 | 8.19 | 0.02 | 203 | 19 | 12 | 19 |

## 2.4. Results and discussion

### 2.4.1. The pH and $pCO_2$ record for the past 22 kyr at Shatsky Rise

Over the 4 – 22 ka, our core records generally decreasing pH and increasing $pCO_2$ for the surface (*G.bulloides, N.pachyderma*; ~50 m) and the lower thermocline (*T.sacculifer*; ~125m) (**Fig. 2-7**). While the data points are relatively sparse for periods after B/A, the LGM-HS1 transition is exceptionally well preserved in the studied core (**Fig. 2-3, Fig. 2-7**). The $\delta^{11}B_{calcite}$ of each foraminifera sample from this study (**Fig. 2-7a**) represented in typical species-specific $\delta^{11}B$ ranges (Henehan et al., 2016; Raitzsch et al., 2018). Although the WNP is a $CO_2$ sink at present days, the deglacial record indicates that the WNP was a $CO_2$ source in the early deglaciation period. The time intervals when the area was a $CO_2$ sink are in late LGM (~21 ka), early HS 1 (~17 ka), and the middle Bølling-Allerod (B/A; ~13 ka) and probably most of the Holocene. In between were prolonged periods when the area acted as a $CO_2$ source – the LGM-to-HS1 transition period (19.7 – 17.5 ka), the middle HS1 (16 – 17 ka), and the Younger Dryas (**Fig. 2-7c, d**).

The reconstructed pH appears in a slightly higher range compared to the surface (~8.17 pH unit) and below-thermocline (~8.06 pH unit) values of modern seawater but within the range of the seasonal maximum (~8.25; Ishii et al., 2011). As known from the current seawater depth profile, the lower thermocline shows a record of lower pH and saturated $pCO_2$ than surface seawater (**Fig. 2-7b,c**). Our record shows that the pH is particularly low in the region corresponding to the LGM-HS1 transition (18–19 ka) and in HS1 (**Fig. 2-7b**). Among them, for LGM-HS1, the pH of the surface seawater increased once, around 18.83 ka (~8.26 pH unit), then decreased (~8.09 pH unit). In

comparison, the pH record of *T. sacculifer* living at the lower thermocline steadily decreased during this period and showed one prominent negative peak (minimum 8.03 pH unit, 19.13 ka). This difference suggests the possibility that surface water and lower thermocline water are separated environments and can only be mixed under certain conditions. When this mixing is suspected of having occurred, it is at the end of the LGM (18 ka) that the surface and the record under the thermocline appear similar. This pH feature also appears in $pCO_2$, indicating that the seawater below the thermocline was markedly saturated with $CO_2$ during the LGM-HS1 transition. However, since the atmospheric $CO_2$ at the time was relatively low, surface water with a high pH in the middle must also have been a $CO_2$ source in terms of $\Delta pCO_2$ (**Fig.2-7d**).

The significant difference is found in surface and sub-thermocline seawater during another period when WNP is a $CO_2$ source, which is middle HS1 (16.84 ka). Both *N. pachyderma* and *T. sacculifer* show significantly lower $\delta^{11}B$ values at this time. Still, the pH and $pCO_2$ of the lower thermocline represented by *T. sacculfer* indicate the most substantial level of $CO_2$ saturation (~8.01 pH units, ~ 330 μatm $pCO_2$). Even considering the uncertainties in the calculations, there would have been extreme $pCO_2$ saturation below the thermocline at this time and somewhat weaker $CO_2$ saturation in the surface water by comparison.

Another $CO_2$ source period is early YD (~12.54 ka), where $pCO_2$ increases in both surface and sub-thermocline waters (~23 μatm $\Delta pCO_2$ in surface) compared to B/A. From this point of view, WNP was a $CO_2$ source in the early YD period, but unfortunately, $pCO_2$ records for the rest of YD could not be reconstructed in this study due to a lack of foraminifera samples.

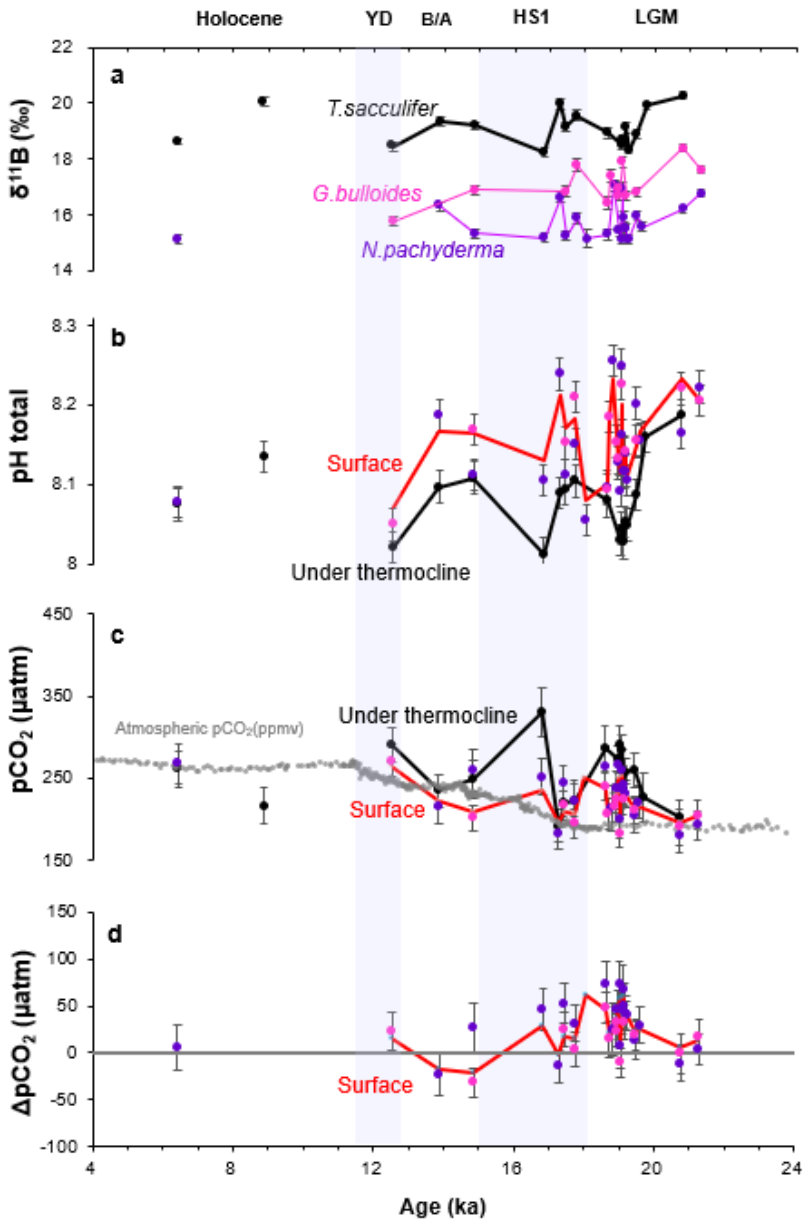


**Figure 2-7.** Carbonate system changes in seawater of Shatsky Rise over the last 4 - 22 kyr.

(a) $\delta^{11}B$ values of *G. bulloides* (pink), *N. pachyderma* (purple) and *T.sacculifer* (black) from core NPGP1302-1B with 2σ uncertainty, (b) pH calculated by $\delta^{11}B$ of planktonic foraminifera, Surface (Red line as median between two species, pH from $\delta^{11}B_{G.\ bulloides}$ as pink dots, $\delta^{11}B_{N.\ pachyderma}$ as blue dots with 2σ uncertainty) and below-thermocline (pH from $\delta^{11}B_{T.sacculifer}$ as black dots and line), (c) Reconstructed seawater $pCO_2$ of surface (red line) and under-thermocline (black line) seawater in this study and atmospheric $pCO_2$ (Bereiter et al., 2015) (d) Reconstructed $\Delta pCO_2$ of surface (red) in WNP.

To understand the reconstructed $pCO_2$ in this study at a local level, a comparison of several local proxies was made: SST (**Fig. 2-8**) and TA (**Fig. 2-8**) used to calculate pH and $pCO_2$, and SPG can indicate extension. The abundance of cold water species (**Fig. 2-8**), marine TOC, and terrestrial TOC data from the STG area (KC-dominant; 31° 23.94' N 134°49.86 E) indicating KC transportation and terrestrial input (**Fig. 2-8**). Among them, SST and TA were calculated from the foraminiferal $\delta^{18}O$ of the studied core (**Table 2-5, Table 2-6**). The $pCO_2$ record in this study does not change significantly at the peak point of SST or TA, so it can be confirmed that the calculated value of pH and $pCO_2$ is more strongly related to the $\delta^{11}B$ value than the SST or TA (**Fig. 2-7a**). In the case of the SPG-STG transition region, such as Shatsky Rise, a decrease in SST can be interpreted as an SPG expansion. Still, in the case of alkenone-derived SST in a nearby region, the overall change in the last deglaciation period has increased due to global warming (Harada et al., 2004). On the other hand, higher TA is often interpreted as an expansion of the SPG in the SPG-STG transition region (Ishii et al., 2011; Jin, 1997; Minoshima et al., 2007). A higher proportion of cold water species can also indicate the extended state of SPG. In addition, the high marine TOC with high terrestrial TOC in the last deglaciation can be interpreted as activated mixing between nutrient-rich SPG and oligotrophic STG water mass, with active transport from continent and islands (Ikehara et al., 2009; Shimoto and Matsumura, 1992). Unlike the aeolian dust fraction, terrestrial TOC is mainly transported by the surface current along the coastal area, which indicates strengthened KC in WNP with higher terrestrial TOC (Ikehara et al., 2009).

From this point of view, the calculated TA (**Fig. 2-8c**) in this study shows a similar SPG expansion

state to previous foraminifera (**Fig. 2-8d**) and TOC (**Fig. 2-8e**) studies. In particular, from the HS1-LGM transition period (18-19 ka) to the middle HS1 (~16.84 ka), it shows a high distribution of coldwater species with high TA, revealing the tendency of the expanded SPG to retreat gradually. The area reporting TOC near KE (**Fig. 2-8e**) is located south of our study area, and STG is dominant (PC8). At this point, as the cause of the high bio-productivity during the HS1-LGM transition period, the active mixing of STG-SPG water and detrital input, which must have been actively supplied by eolian and coastal currents (Ikehara et al., 2009; Li et al., 2004; Minoshima et al., 2007). The nutrient sources are limited in oligotrophic STG, and if the features of low terrestrial TOC and high marine TOC appear in the STG area, it is considered that the nutrient should be provided by eolian input or mixing of nutrient-rich intermediate water (Kobari et al., 2020; Kouketsu et al., 2016; Saito, 2019). In addition, during the HS1-LGM transition period, the terrestrial TOC gradually increases, and the marine TOC is very high compared to the present and then gradually decreases, which could be the effect of the progressively stronger transport of STG water (KC). It has been mentioned that the remarkably rapid increase in terrestrial TOC during this period is related to sea-level rise (Ikehara et al., 2009).

One of the interesting points is that all of our positive $pCO_2$ peaks in LGM-HS1 appeared when the marine TOC was high as the terrestrial TOC gradually increased, that is, when STG expansion and mixing were active. In addition, for surface water $pCO_2$, negative $pCO_2$ peaks ($CO_2$ sink signal) appear in some of the peaks in which the terrestrial TOC rapidly increased. Representatively, a short period (19.06 ka) of late LGM where $pCO_2$ drop appeared only on the surface, including early HS1, B/A with thermocline $pCO_2$ decreasing. In this respect, the surface water of WNP appears to respond

sensitively to the influx of continent-derived nutrients, and it tends to absorb $CO_2$ as the TOC delivered from the coastal current increases. However, the period when WNP is a $CO_2$ source is characterized by a significant rise in $pCO_2$ in the lower thermocline seawater over a relatively long period. At this time, the terrestrial TOC gradually increases on a long-term time scale, and the marine TOC appears exceptionally high. If the increased inflow and mixing of $CO_2$-rich intermediate water supplied nutrients to the high bio-productivity of WNP, the simultaneous increase in $CO_2$ in the surface layer and near the thermocline could be explained to some extent. This consideration will be compared to the NP and the surrounding Pacific records, which supply intermediate water to WNP.

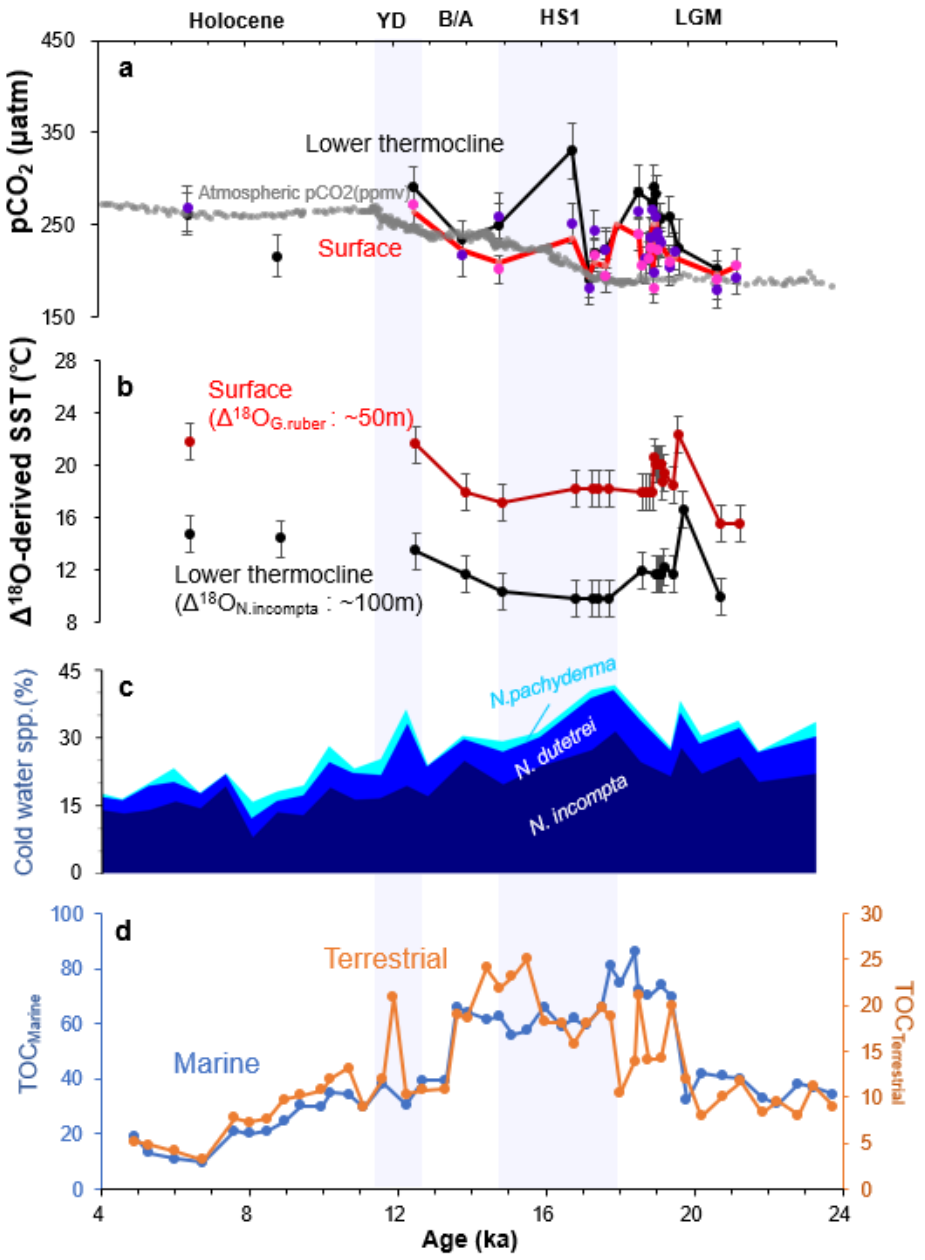


**Figure 2-8.** Paleoceanographic variables in Shatsky Rise over the last 4 - 22 kyr.

(a) Reconstructed seawater $pCO_2$ of surface (red line) and under-thermocline (black line) seawater in this study and atmospheric $pCO_2$ (Bereiter et al., 2015), (b) $\Delta^{18}O$-based SST of surface (red) and lower thermocline (black) (c) Abundance of cold water species in core NPGP1302-1B, same core with this study (Seo et al., 2018), (d) Total organic carbon (TOC) in Kuroshio-dominant area, core PC8, Marine (blue) and Terrestrial (orange) in mass accumulate rate (MAR; mg $cm^2$ $kyr^{-1}$) (Ikehara et al., 2009; Minoshima et al., 2007).

### 2.4.2. · Comparison of the Pacific $\Delta pCO_2$ data in the Northern Hemisphere

WNP $\Delta pCO_2$ data from the surface show that strong $CO_2$ degassing (maximum ~73 µatm) occurred in late LGM (19.5-17.5 ka) and a weaker one (~45 µatm) in middle HS1. Drawdown of $CO_2$ (~28 µatm) occurred in late LGM, early HS1, and middle B/A and throughout the Holocene (**Fig. 2-9**). Here, we compare $\Delta pCO_2$ data with literature data for other locations of the Pacific Ocean in the Northern Hemisphere – the NP (*N. pachyderma*; Gray et al.,2018), WEP (*G. ruber*; Kubota et al., 2019), and EEP (*G. sacculifer*; Martinez-Boti et al., 2015). Although the dominant foraminiferal species and their depth of habitat differ between the four sites, the sub-dwelling depths of the planktonic foraminifera used in each of the studies do not exceed the thermocline depth (~150 m). In addition, while the SST, S, pH and $\delta^{11}B_{borate}$ are for local seawater, $pCO_{2,sw}$ data can be compared globally, as has been demonstrated for the global $\Delta pCO_2$ comparison study (Shao et al., 2019; Shuttleworth. et al., 2022).

Considering the surface $\Delta pCO_2$ source peaks in WNP (**Fig. 2-8d**) coincide with rapid saturation of below thermocline $pCO_2$, the $\Delta pCO_2$ records from NP are vital as a significant source of intermediate water in the Northern Hemisphere. When WNP was a strong source ($\Delta pCO_2$ ~ 73 µatm) in the LGM-to-HS1 transition period (19.6 – 17.5 ka), the NP reached a fairly high $\Delta pCO_2$ of ~ 83 µatm (**Fig. 2-9a**). The NP-WNP coincidence of high $\Delta pCO_2$ also appears in middle HS1 and early YD, the time interval of rapid increase of atmospheric $pCO_2$. These observations have some implications in global warming of the last deglaciation, as the circulation and $CO_2$ degassing relationship between NP and WNP in rapid $CO_2$ increasing HS1 and YD.

In the case of WEP (**Fig. 2-9b**)**,** the surface water shows $CO_2$ sink signals during the last deglaciation. Unless the upper-thermocline $pCO_2$ records in WEP indicate large-scale $pCO_2$ saturation (~maximum 420 μatm) during 4-20 ka, as the intermediate water from the increasing $CO_2$ in Sub-Antarctic mode water (SAMW) (Kubota et al., 2019; Shuttleworth et al., 2021). The $CO_2$ records from WEP show quite different local patterns (Kubota et al., 2019; Palmer and Pearson, 2003; Xiong et al., 2022), hypothesized the various environments by regional upwelling, riverine input, and ENSO influence (Xiong et al., 2022). The $CO_2$ increase in intermediate water from SAMW is more represented by EEP (**Fig. 2-9c**) because of the active upwelling in the last deglaciation (Kubota et al., 2021; Martínez-Botí et al., 2015).

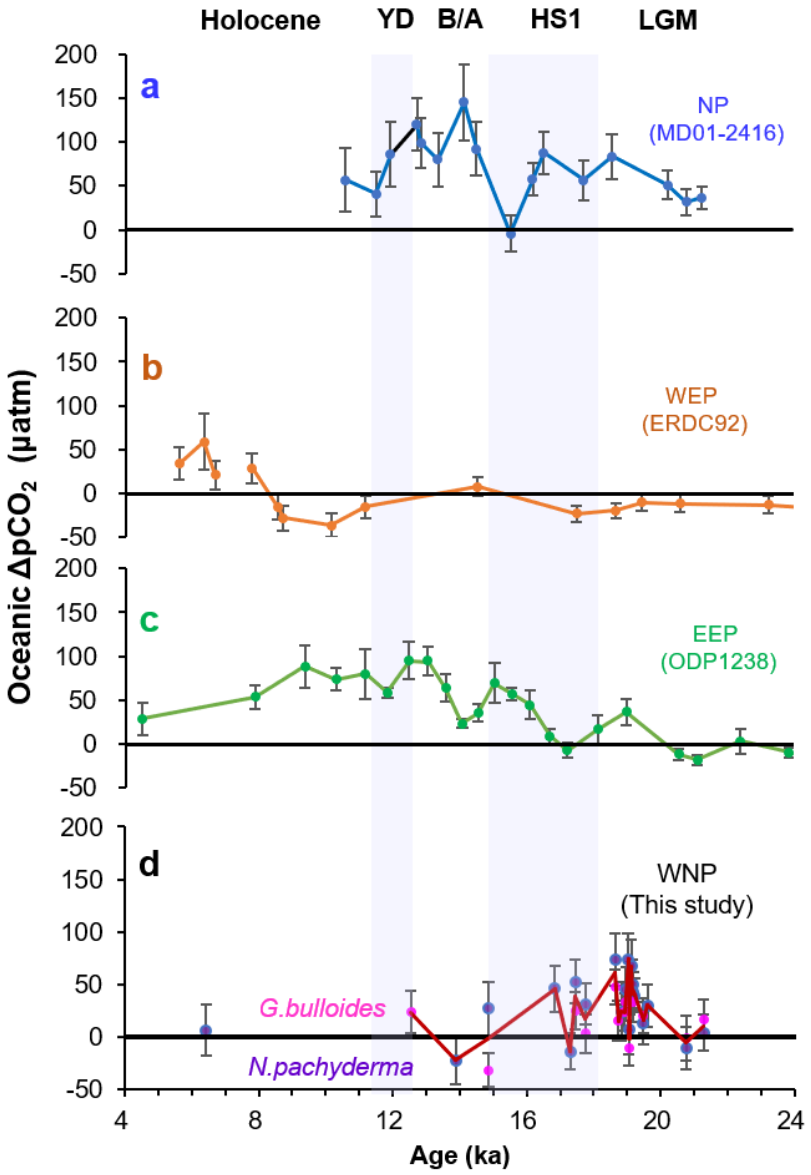


**Figure 2-9.** Comparison with $\Delta pCO_2$ data from previous studies of the Pacific area.
(a) North Pacific (Gray et al., 2018), (b) west equatorial Pacific (WEP; Kubota et al., 2019) (c) east equatorial Pacific (EEP; Martínez-Botí et al., 2015), (d) western North Pacific (WNP) from this study.

### 2.4.3. Surface circulation events of the Pacific during the last deglaciation

Since the significant $CO_2$ source peaks from WNP data have close relationships between SPG-STG mixing and North Pacific intermediate water, $CO_2$ pool and intermediate exchange models from WEP (Kubota et al., 2019) and NP (Rae et al., 2020) are combined and interpreted for this study (**Fig. 2-10**).

In this model, the SPG area in the surface seawater widens by cooling or ENSO effects (LGM; **Fig. 2-10a**). The upwelling of NP is activated, and $CO_2$ in intermediate water is released to surface SPG seawater. However, this $CO_2$ saturation is more activated on the surface of NP. The $CO_2$ transport by intermediate water might be isolated in WNP, considering the low $pCO_2$ surrounding the lower thermocline in WNP (LGM, early HS1).

On the other hand, STG water mass rises to the north in the episodic warming or strengthening of the KC (LGM-HS1 transition, middle HS1, YD; **Fig. 2-10b**) in the surface. At this time, SPG retreats to the surface but moves below the thermocline depth of the SPG-STG transition zone due to the relatively higher density than STG water, as the flow is known as lateral transport (Gray et al., 2020; Rae et al., 2020). In this case, the $CO_2$ pool is located in the shallower depth due to weak sinking and lateral transport, which can be considered the cause of the rapid saturation of $pCO_2$ below the thermocline in WNP. This $CO_2$-saturated seawater might be well-circulated and provide nutrients to the SPG-STG transition zone, indicated by high productivity. Also, the increased $CO_2$ of SAMW was transported to the equatorial area, recorded in the gradual $pCO_2$ increase in EEP and upper-thermocline WEP (Kubota et al., 2019).

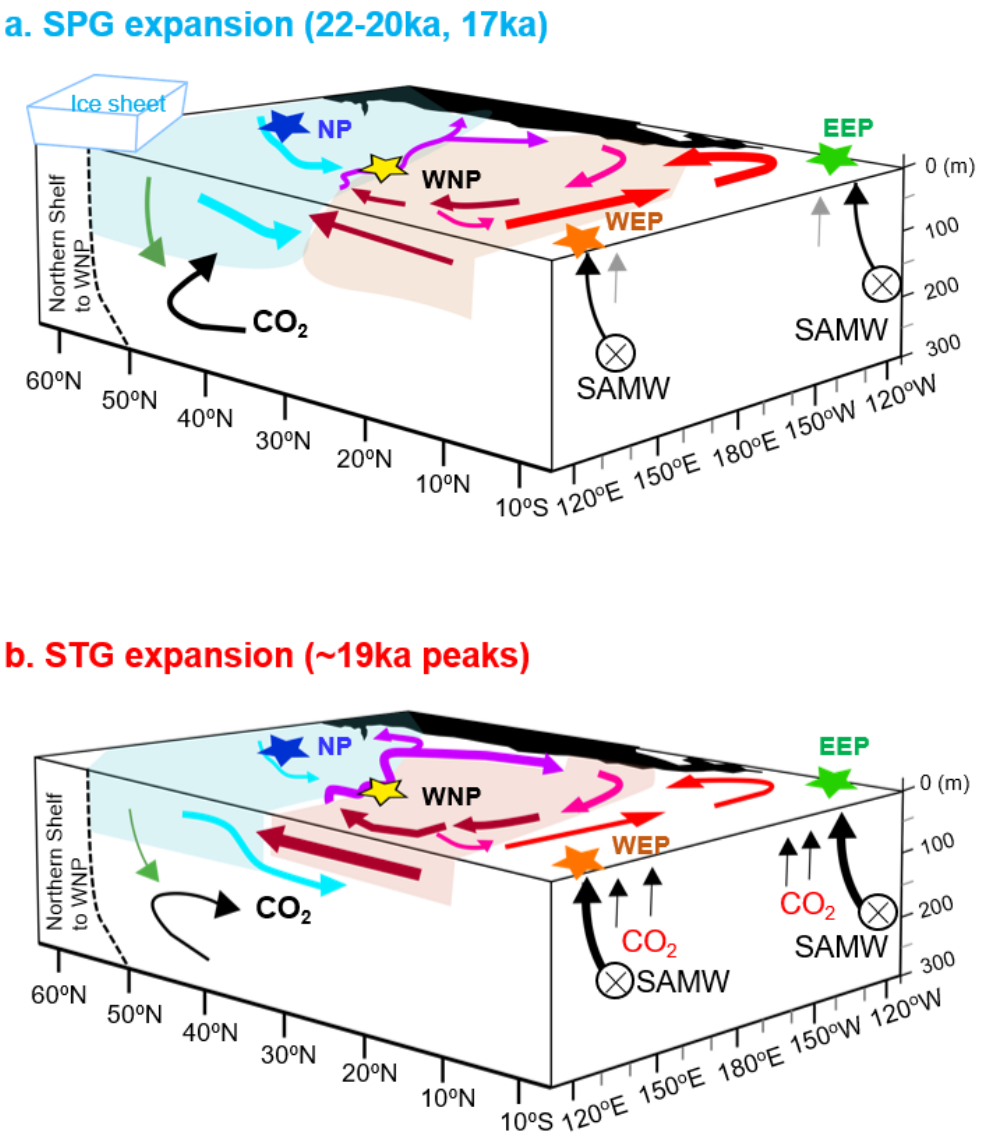


**Figure 2-10.** Schematic descriptions of circulation in the Northern Hemisphere Pacific during the last deglaciation. Each location of deglacial Pacific $pCO_2$ studies are indicated in the figure as follows; WNP (NPGP1302-1B; this study) as yellow star symbol, Blue star symbol as NP (MD01-2416; Gray et al., 2018), Orange star symbol as WEP (KR05-15; Kubota et al., 2019), and EEP as green star symbol (ODP1238; Martinez-Boti et al., 2015). **SAMW**, Sub-Antarctic mode water.

## 2.5. Conclusion

The Kyroshio extension and its transition zone are significant exchanges of $CO_2$ with the atmosphere in the modern ocean. In the western North Pacific (WNP), this area has a specific position where sub-tropical and sub-polar gyre (STG-SPG) water masses mix, and the processes of oceanographic change are related to gyre transition reflecting climate change. Comparing the timing of changes in these factors with the $CO_2$ storage capacity will provide a more detailed understanding of the Northwest Pacific climate system. The post-LGM is a period in which these control factors in the western North Pacific (WNP) can be closely observed through the well-known glacial-interglacial events.

This study reconstructed new high-resolution boron isotope-derived $pCO_{2,sw}$ record for 4-22 ka at Shatsky Rise core NPGP1302-1B (32° 16′N, 158° 13′ E; 2514 m water depth), western North Pacific (WNP). This area is known as the Kuroshio Extension and subpolar-subtropical gyre boundary system, one of the Pacific's largest surface current mixing areas. Our records were reconstructed from multi-species planktonic foraminifera, each representing water mass at different habitat depths: *G. sacculifer* (n=21), *G. bulloides* (n=16), and *N. Pachyderma* (n=26).

The planktonic foram data showed that the northwest Pacific actively released $CO_2$ into the atmosphere during LGM to HS1 and the middle HS1 and absorbed $CO_2$ from the atmosphere in early HS1 and early YD. The WNP $\Delta pCO_{2,sw}$ have a close relationship with North Pacific by the mechanism of SPG-STG expansion. The combined circulation model from North Pacific and Equatorial Pacific areas suggests SPG-related $pCO_2$ pool in WNP.

## 2.6. References


Bereiter, B., Eggleston, S., Schmitt, J., Nehrbass-Ahles, C., Stocker, T.F., Fischer, H., Kipfstuhl, S., Chappellaz, J., 2015. Revision of the EPICA Dome C CO2 record from 800 to 600 kyr before present. Geophysical Research Letters 42, 542-549.

Clarkson, M., Kasemann, S.A., Wood, R., Lenton, T., Daines, S., Richoz, S., Ohnemueller, F., Meixner, A., Poulton, S.W., Tipper, E., 2015. Ocean acidification and the Permo-Triassic mass extinction. Science 348, 229-232.

Darling, K.F., Wade, C.M., Siccha, M., Trommer, G., Schulz, H., Abdolalipour, S., Kurasawa, A., 2017. Genetic diversity and ecology of the planktonic foraminifers Globigerina bulloides, Turborotalita quinqueloba and Neogloboquadrina pachyderma off the Oman margin during the late SW Monsoon. Marine Micropaleontology 137, 64-77.

De Boer, A.M., Graham, R.M., Thomas, M.D., Kohfeld, K.E., 2013. The control of the Southern Hemisphere Westerlies on the position of the Subtropical Front. Journal of Geophysical Research: Oceans 118, 5669-5675.

Foster, G.L., 2008. Seawater pH, pCO2 and [CO2− 3] variations in the Caribbean Sea over the last 130 kyr: A boron isotope and B/Ca study of planktic foraminifera. Earth and Planetary Science Letters 271, 254-266.

Foster, G.L., Marschall, H.R., Palmer, M.R., 2018. Boron isotope analysis of geological materials, Boron Isotopes. Springer, pp. 13-31.

Foster, G.L., Rae, J.W., 2016. Reconstructing ocean pH with boron isotopes in foraminifera. Annual Review of Earth and Planetary Sciences 44, 207-237.

Gattuso, J.-P., Lavigne, H., 2009. Approaches and software tools to investigate the impact of ocean acidification. Biogeosciences 6, 2121-2133.

Gray, W.R., Rae, J.W., Wills, R.C., Shevenell, A.E., Taylor, B., Burke, A., Foster, G.L., Lear, C.H., 2018. Deglacial upwelling, productivity and CO2 outgassing in the North Pacific Ocean. Nature Geoscience 11, 340-344.

Gray, W.R., Wills, R.C., Rae, J.W., Burke, A., Ivanovic, R.F., Roberts, W.H., Ferreira, D., Valdes, P.J., 2020. Wind-driven evolution of the North Pacific subpolar gyre over the last deglaciation. Geophysical Research Letters 47, e2019GL086328.

Foster, G.L., 2017. A record of Neogene seawater $\delta^{11}$ B reconstructed from paired $\delta^{11}$B analyses on benthic and

planktic foraminifera. Climate of the Past 13, 149-170.

Hain, M.P., Sigman, D.M., Higgins, J.A., Haug, G.H., 2015. The effects of secular calcium and magnesium concentration changes on the thermodynamics of seawater acid/base chemistry: Implications for Eocene and Cretaceous ocean carbon chemistry and buffering. Global Biogeochemical Cycles 29, 517-533.

Harada, N., Ahagon, N., Uchida, M., Murayama, M., 2004. Northward and southward migrations of frontal zones during the past 40 kyr in the Kuroshio-Oyashio transition area. Geochemistry, Geophysics, Geosystems 5.

Henehan, M.J., Foster, G.L., Bostock, H.C., Greenop, R., Marshall, B.J., Wilson, P.A., 2016. A new boron isotope-pH calibration for Orbulina universa, with implications for understanding and accounting for 'vital effects'. Earth and Planetary Science Letters 454, 282-292.

Hu, D., Wu, L., Cai, W., Gupta, A.S., Ganachaud, A., Qiu, B., Gordon, A.L., Lin, X., Chen, Z., Hu, S., 2015. Pacific western boundary currents and their roles in climate. Nature 522, 299-308.

Ikehara, M., Akita, D., Matsuda, A., 2009. Enhanced marine productivity in the Kuroshio region off Shikoku during the last glacial period inferred from the accumulation and carbon isotopes of sedimentary organic matter. Journal of Quaternary Science: Published for the Quaternary Research Association 24, 848-855.

Ishii, M., Kosugi, N., Sasano, D., Saito, S., Midorikawa, T., Inoue, H.Y., 2011. Ocean acidification off the south coast of Japan: A result from time series observations of CO2 parameters from 1994 to 2008. Journal of Geophysical Research: Oceans 116.

Jin, F.-F., 1997. A theory of interdecadal climate variability of the North Pacific ocean–atmosphere system. Journal of Climate 10, 1821-1835.

Kasemann, S., Erzinger, J., Franz, G., 2000. Boron recycling in the continental crust of the central Andes from the Palaeozoic to Mesozoic, NW Argentina. Contributions to Mineralogy and Petrology 140, 328-343.

Kawahata, H., Ohshima, H., 2002. Small latitudinal shift in the Kuroshio Extension (Central Pacific) during glacial times: evidence from pollen transport. Quaternary Science Reviews 21, 1705-1717.

Key, R.M., Kozyr, A., Sabine, C.L., Lee, K., Wanninkhof, R., Bullister, J.L., Feely, R.A., Millero, F.J., Mordy, C., Peng, T.H., 2004. A global ocean carbon climatology: Results from Global Data Analysis Project (GLODAP). Global biogeochemical cycles 18.

Klochko, K., Kaufman, A.J., Yao, W., Byrne, R.H., Tossell, J.A., 2006. Experimental measurement of boron isotope fractionation in seawater. Earth and Planetary Science Letters 248, 276-285.

Kobari, T., Honma, T., Hasegawa, D., Yoshie, N., Tsutsumi, E., Matsuno, T., Nagai, T., Kanayama, T., Karu, F., Suzuki, K., 2020. Phytoplankton growth and consumption by microzooplankton stimulated by turbulent nitrate flux suggest rapid trophic transfer in the oligotrophic Kuroshio. Biogeosciences 17, 2441-2452.

Kouketsu, S., Kaneko, H., Okunishi, T., Sasaoka, K., Itoh, S., Inoue, R., Ueno, H., 2016. Mesoscale eddy effects on temporal variability of surface chlorophyll a in the Kuroshio Extension. Journal of Oceanography 72, 439-451.

Kubota, K., Ishikawa, T., Nagaishi, K., Kawai, T., Sagawa, T., Ikehara, M., Yokoyama, Y., Yamazaki, T., 2021. Comprehensive analysis of laboratory boron contamination for boron isotope analyses of small carbonate samples. Chemical Geology 576, 120280.

Kubota, K., Yokoyama, Y., Ishikawa, T., Sagawa, T., Ikehara, M., Yamazaki, T., 2019. Last deglacial pCO2 reconstruction in the western equatorial Pacific: new findings and issues of boron isotope proxy, Geophysical Research Abstracts.

Li, T., Masuzawa, T., Kitagawa, H., 2004. Seasonal variations in settling fluxes of major components in the oligotrophic Shikoku Basin, the western North Pacific: coincidence of high biogenic flux with Asian dust supply in spring. Marine Chemistry 91, 187-210.

Martínez-Botí, M.A., Marino, G., Foster, G.L., Ziveri, P., Henehan, M.J., Rae, J.W., Mortyn, P.G., Vance, D., 2015. Boron isotope evidence for oceanic carbon dioxide leakage during the last deglaciation. Nature 518, 219-222.

McCulloch, M.T., Holcomb, M., Rankenburg, K., Trotter, J.A., 2014. Rapid, high-precision measurements of boron isotopic compositions in marine carbonates. Rapid Communications in Mass Spectrometry 28, 2704-2712.

Minoshima, K., Kawahata, H., Ikehara, K., 2007. Changes in biological production in the mixed water region (MWR) of the northwestern North Pacific during the last 27 kyr. Palaeogeography, Palaeoclimatology, Palaeoecology 254, 430-447.

Mizuno, K., White, W.B., 1983. Annual and interannual variability in the Kuroshio current system. Journal of physical oceanography 13, 1847-1867.

Na, H., Kim, K.-Y., Minobe, S., Sasaki, Y.N., 2018. Interannual to decadal variability of the upper-ocean heat content in the western North Pacific and its relationship to oceanic and atmospheric variability. Journal of Climate 31, 5107-5125.

Ohkushi, K.i., Thomas, E., Kawahata, H., 1999. Abyssal benthic foraminifera from the northwestern Pacific (Shatsky Rise) during the last 298 kyr. Marine Micropaleontology 38, 119-147.

Palmer, M., Pearson, P.N., 2003. A 23,000-year record of surface water pH and P CO2 in the western equatorial Pacific Ocean. Science 300, 480-482.

Paris, G., Bartolini, A., Donnadieu, Y., Beaumont, V., Gaillardet, J., 2010. Investigating boron isotopes in a middle Jurassic micritic sequence: Primary vs. diagenetic signal. Chemical Geology 275, 117-126.

Qiu, B., Chen, S., 2010. Interannual variability of the North Pacific Subtropical Countercurrent and its associated mesoscale eddy field. Journal of Physical Oceanography 40, 213-225.

Qiu, B., Chen, S., Powell, B.S., Colin, P.L., Rudnick, D.L., Schönau, M.C., 2019. Nonlinear short-term upper ocean circulation variability. Oceanography 32, 22-31.

Rae, J.W., Gray, W., Wills, R., Eisenman, I., Fitzhugh, B., Fotheringham, M., Littley, E., Rafter, P., Rees-Owen, R., Ridgwell, A., 2020. Overturning circulation, nutrient limitation, and warming in the Glacial North Pacific. Science advances 6, eabd1654.

Rae, J.W., Zhang, Y.G., Liu, X., Foster, G.L., Stoll, H.M., Whiteford, R.D., 2021. Atmospheric CO2 over the past 66 million years from marine archives. Annual Review of Earth and Planetary Sciences 49, 609-641.

Raitzsch, M., Bijma, J., Benthien, A., Richter, K.-U., Steinhoefel, G., Kučera, M., 2018. Boron isotope-based seasonal paleo-pH reconstruction for the Southeast Atlantic–A multispecies approach using habitat preference of planktonic foraminifera. Earth and Planetary Science Letters 487, 138-150.

Roden, G.I., 1991. Subarctic-subtropical transition zone of the North Pacific: large-scale aspects and mesoscale structure. NOAA technical report NMFS 105, 1-38.

Sadekov, A., Lloyd, N.S., Misra, S., Trotter, J., D'Olivo, J., McCulloch, M., 2019. Accurate and precise microscale measurements of boron isotope ratios in calcium carbonates using laser ablation multicollector-ICPMS. Journal of Analytical Atomic Spectrometry 34, 550-560.

Saito, H., 2019. The Kuroshio: its recognition, scientific activities and emerging issues. Kuroshio current: Physical, biogeochemical, and ecosystem dynamics, 1-11.

Sakamoto, T.T., Hasumi, H., Ishii, M., Emori, S., Suzuki, T., Nishimura, T., Sumi, A., 2005. Responses of the Kuroshio and the Kuroshio Extension to global warming in a high-resolution climate model. Geophysical Research Letters 32.

Scott, G.H., 2020. Zooplankters in an oligotrophic ocean: contrasts in the niches of Globigerinoides ruber and Trilobatus sacculifer (Foraminifera: Globigerinida) in the South Pacific. Ecoscience 27, 269-278.

Seo, I., Lee, Y., Yoo, C.M., Hyeong, K., 2018. Migration of the Kuroshio Extension in the Northwest Pacific

since the last glacial maximum. Palaeogeography, Palaeoclimatology, Palaeoecology 496, 323-331.

Shao, J., Stott, L.D., Gray, W.R., Greenop, R., Pecher, I., Neil, H.L., Coffin, R.B., Davy, B., Rae, J.W., 2019. Atmosphere-ocean CO2 exchange across the last deglaciation from the Boron Isotope Proxy. Paleoceanography and Paleoclimatology 34, 1650-1670.

Shimoto, A., Matsumura, S., 1992. Primary productivity in a cold water mass and the neighborhood area occurring off Enshu-Nada in the late summer of 1989. Journal of Oceanography 48, 105-115.

Shuttleworth, R., Bostock, H., Chalk, T.B., Calvo, E., Jaccard, S., Pelejero, C., Martínez-García, A., Foster, G., 2021. Early deglacial CO2 release from the Sub-Antarctic Atlantic and Pacific oceans. Earth and planetary science letters 554, 116649.

Sosdian, S.M., Greenop, R., Hain, M., Foster, G.L., Pearson, P.N., Lear, C.H., 2018. Constraining the evolution of Neogene ocean carbonate chemistry using the boron isotope pH proxy. Earth and Planetary Science Letters 498, 362-376.

Thompson, P.R., 1981. Planktonic foraminifera in the western North Pacific during the past 150 000 years: comparison of modern and fossil assemblages. Palaeogeography, Palaeoclimatology, Palaeoecology 35, 241-279.

Ujiié, Y., Asahi, H., Sagawa, T., Bassinot, F., 2016. Evolution of the North Pacific Subtropical Gyre during the past 190 kyr through the interaction of the Kuroshio Current with the surface and intermediate waters. Paleoceanography 31, 1498-1513.

# Chapter 3. Comparison of Darriwilian $\delta^{13}C$ and $\delta^{11}B$ records in the Taebaeksan basin, Korea: carbonate platform anoxia and ocean acidification

## 3.1. Introduction

The boron isotopes compositions analyzed in ocean carbonates enable the modeling of the partial pressure of dissolved $CO_2$ in seawater based on carbonate chemical systems by restoring the pH of the past ocean (Foster et al., 2018; Kasemann et al., 2005). Recently, analytical methods for boron isotopes have been actively developed, and the studies applied to reconstructing the palaeoclimatic/paleoceanographic records of that period in various Cenozoic sediments have increased (Greenop et al., 2017; Misra and Froelich, 2012; Rae et al., 2021; Shuttleworth et al., 2021). On the other hand, attempts have been made to restore the pH of the Paleozoic and Proterozoic oceans with boron isotopes, but there are still a few cases (Clarkson et al., 2015; Jurikova et al., 2020; Kasemann et al., 2000; Paris et al., 2010).

In this point of view, the Middle Ordovician is one of the time intervals with the middle Darriwilian isotopic carbon excursion (MDICE) that appears during the onset of long-term cooling and rapid biodiversity of the Middle Ordovician. There are large carbon excursions from the Middle-Late Ordovician with the most extensive glaciation and mass extinction (**Fig. 3-1**). Meanwhile, another characteristic of the Middle Ordovician is the Great Ordovician Biodiversification Event (GOBE). This is one of the most significant events of marine species speciation throughout the Phanerozoic as well as the Paleozoic and is known to have started at the same time as MDICE (Algeo et al., 2016a;

Deng et al., 2021; Rasmussen et al., 2016; Servais and Harper, 2018). However, the cause that triggered GOBE still needs to be clarified in Middle Ordovician studies. Although long-term cooling can be suspected, cooling itself during the MDICE period did not appear significantly, so it is a rather orbital cooling with slow change to be seen as a cause for the rapid occurrence of GOBE (**Fig. 3-1**) (Dronov, 2013; Fang et al., 2019; Trotter et al., 2008). Also, during this period, long-term sea-level elevation began, and how this change is related to MDICE and GOBE is being actively discussed locally and globally (Guo et al., 2020a; Haq and Schutter, 2008; Rasmussen et al., 2021; Schmitz et al., 2019; Witzke and Bunker, 1996; Xiong et al., 2019).

The middle Darriwilian isotopic carbon excursion (MDICE) is the positive carbon isotope excursion (with a difference within 2‰ depending on the region) that appears in the Middle Darriwilian Stage (Ainsaar et al., 2020). In sections from the paleo-continents Laurentia and Baltica, MDICE was defined as a three-peak carbon isotope excursion in a biozone between E.suecicus and P.serra, in some early studies (Ainsaar et al., 2010; Ainsaar et al., 2004; Lehnert et al., 2014). However, the sections with the part of carbon isotopic excursion by Erosion or unconformity, for example, in Argentine Precordillera (Albanesi et al., 2013), Siberia (Ainsaar et al., 2015), South China (Munnecke et al., 2011; Schmitz et al., 2010), North China (Bang and Lee, 2020; Jing et al., 2022) and Tarim Basin (Zhang and Munnecke, 2015) were reported. Therefore, the reported MDICE sections show at least one carbon isotope excursion of +2‰ or higher in middle Darriwilian and considered these positive carbon excursions to MDICE as a global carbon isotopic event.

According to the $\delta^{13}C$, $\delta^{15}N$ with paleoceanic parameters from Bang and Lee (2020), the MDICE of

the Taebaek section was a time interval accompanied by rapid rainfall-derived weathering, seawater stratification, oceanic anoxia, and salinity-driven downwelling in a situation where the global sea level increased. Judging from this point, it was expected that acidification and its changes with time could be sufficiently observed on the local scale. In this study, we updated the biostratigraphy of MDICE containing the Taebaek section and reconstructed the seawater boron isotope-pH record from the same samples of Taebaek MDICE. This new approach will enrich the interpretation of shallow marine environmental change currently being attempted by Middle Ordovician studies.

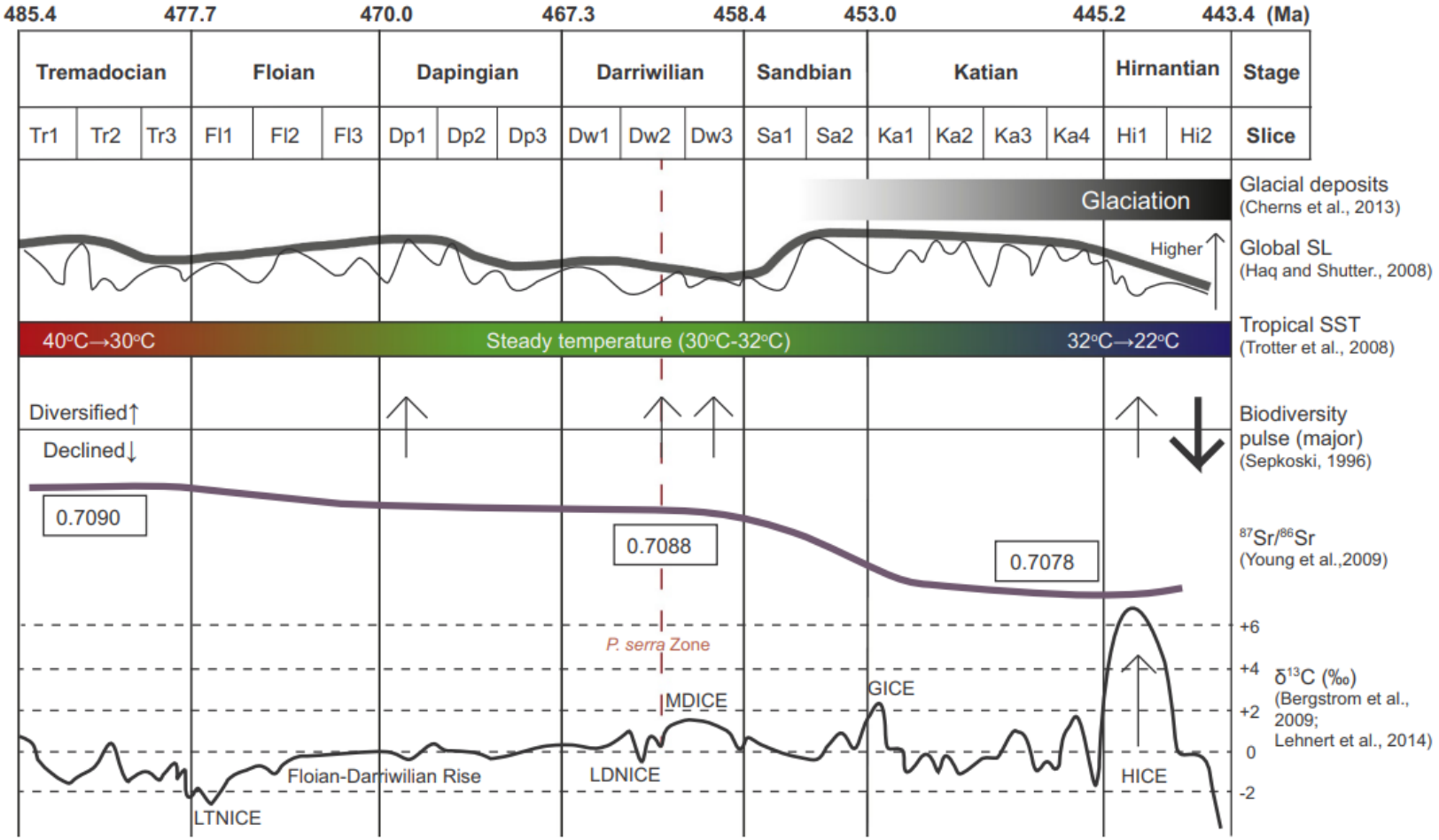


**Figure 3-1.** The Ordovician global environmental signals (modified after Bang and Lee, 2020). SL: sea level; SST: sea surface temperature (Bergstroem et al., 2009; Cherns et al., 2013; Gradstein et al., 2020; Haq and Schutter, 2008; Trotter et al., 2008; Young et al., 2009)

### 3.2. Study Area

The Korean Peninsula during the Paleozoic was part of the Sino-Korean Block (SKB; also called the North China Block), which was located in the equatorial northeastern peri-Gondwana region during the early Paleozoic. Lower Paleozoic sediments were deposited in epeiric sea environments. Biostratigraphic details of Middle Ordovician strata of the southern Korean Peninsula (the Taebaeksan Basin) have been studied extensively (Cho et al., 2021; Choi and Chough, 2005; Lee et al., 2022; Lee, 1989; Lee and Lee, 1986). Trilobites and conodonts biostratigraphically constrain Middle Ordovician strata in the Taebaeksan Basin to have been deposited in the Dapingian–Darriwilian age, and some strata in the western part extended to the early Sandbian. With these biostratigraphic constraints, a detailed chemostratigraphic correlation of the Korean Middle Ordovician strata with the global carbon-isotopic reference profiles is possible.

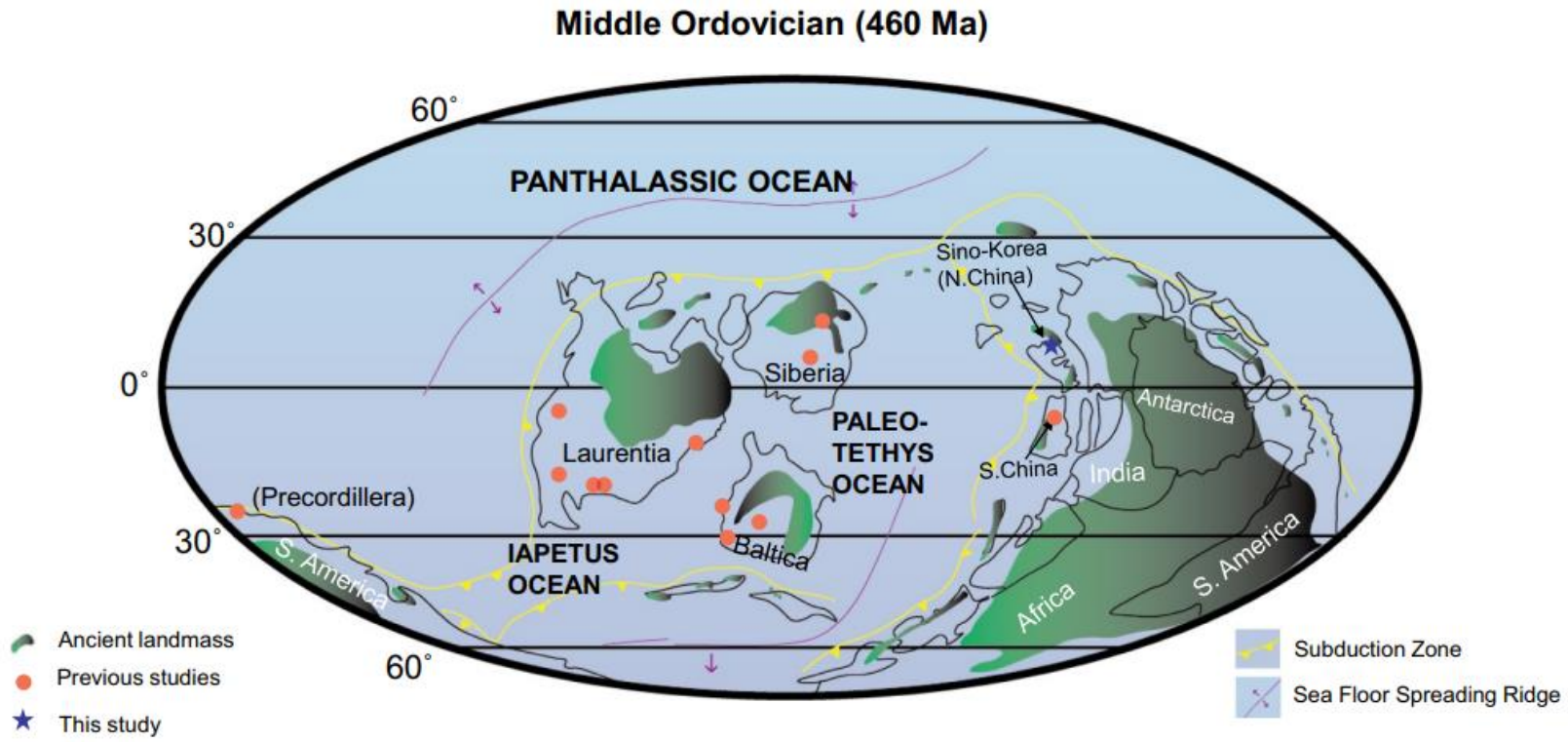


**Figure 3-2.** The Middle Ordovician paleogeographic map showing locations of previously studied MDICE sections (red dots) and sections of this study (blue star). Studied sections (Ainsaar et al., 2010; Albanesi et al., 2013; Jing et al., 2022; Kaljo et al., 2007; Lehnert et al., 2014; Sial et al., 2013; Thompson and Kah, 2012; Zhang and Munnecke, 2015). The paleogeographic map is based on Scotese and Golonka (1997), Torsvik and Cocks (2013), Yao et al. (2015), and Lee et al. (2016); modified from Bang and Lee (2020)

The SKB is one of the major crustal blocks in East Asia, and in present-day coordinates, the Korean Peninsula forms the southeastern part of the SKB. During the early Paleozoic, the SKB was located in the equatorial peri-Gondwana region, the northern part of Australia, as part of a large epicontinental sea developed on the north of the Gondwana margin (**Fig. 3-2**). The Taebaeksan Basin is located in central-eastern Korea, and its lower Paleozoic basin fill is called the Joseon Supergroup (**Table 3-1**). This supergroup is a 1.5 km-thick mixed siliciclastic-carbonate package deposited in a passive margin or intracratonic basin setting (Lee et al., 2016).

The Joseon Supergroup is known to be of marine origin, dominated by shallow platform carbonate rocks with interbedded siliciclastic rocks. Deposition of the Joseon Supergroup is interpreted to have been controlled mainly by eustatic changes, and the sequence shows cyclic sedimentation patterns (Choi et al., 2004; Kwon et al., 2006). In the Taebaeksan Basin, the Joseon Supergroup is conventionally subdivided into five groups based on distinct lithological successions and geographic distributions: the Taebaek, Yeongweol, Yongtan, Pyeongchang, and Mungyeong groups (**Table 3-1**; Choi et al., 2004). The Taebaek Group (also called the Duwibong Unit) is distributed in the eastern Taebaeksan Basin with a thickness of 1.5 km and represents proximal facies. It forms the type sequence of the early Paleozoic in South Korea, subdivided into ten lithostratigraphic units: the Myeonsan, Myobong, Daegi, Sesong, Hwajeol, Dongjeom, Dumugol, Makgol, Jigunsan, and Duwibong Formations with decreasing age (Lee et al., 2016). Among these strata, the Makgol, Jigunsan, and Duwibong Formations, corresponding to the Middle Ordovician age, are the subjects of this study.

**Table 3-1.** The Ordovician time scale and stratigraphic division of the Taebaek strata of the Joseon Supergroup (modified from Choi et al., 2004, Cho et al., 2021)

| Geologic Age | | | Taebaek Group |
|---|---|---|---|
| Ordovician | Upper | Hirnantian | |
| | | Katian | |
| | | Sandbian | |
| | Middle | Darriwilian | Duwibong Fm. |
| | | | Jigunsan Fm. |
| | | Dapingian | Makgol Fm. |
| | Lower | Floian | Dumugol Fm. |
| | | Tremadocian | Dongjeom Fm. |

## 3.3. Analytical Method

### 3.3.1. Sample Information

This study analyzed $\delta^{11}B$ and trace elements from 20 carbonate rocks of the upper Makgol, Jigunsan, and Duwibong Formation of the Taebaek section (37° 05' 09" N, 129° 08' 26″ E), which have been described in detail by Bang and Lee (2020). $\delta^{13}C$ and $\delta^{15}N$, $\delta^{18}O$, clay mineral (%), TIC, TOC, and TN data of the carbonates were reported by Bang and Lee (2020).

The powdered samples with high $CaCO_3$ content (50-95 %) were selected at an interval of 3-4 m at a stratigraphic thickness of about 100 m, including the upper part of the Makgol Formation, the Jigunsan Formation, and the Duwibong Formation (**Fig. 3-3, Fig. 3-4**).

The lithology of the uppermost 10 m of the Makgol Formation was reported as crudely laminated lime mudstone, bioturbated wackestone to grainstone, finely laminated dolomitic lime mudstone, and

oncoid/ooid grainstone in ascending order (Bang and Lee, 2020; Choi et al., 2004). The boundary with the overlying Jigunsan Formation was set at the horizon between the massive oncoid/ooid grainstone to packstone bed below and the dark gray homogeneous mudstone bed above.

The lower Jigunsan Formation unit is about 10 m thick, composed of organic-rich beds in the lower part and an alternation of dark gray mudstone and crudely laminated lime mudstone in the upper part. Several cm-long calcareous nodules occur along the bedding planes in the lower unit and contain some brachiopod and gastropod shells within them (Woo and Chough, 2007). Characteristically, the outer rims of calcareous nodules are replaced by abundant pyrites. The middle unit of the studied sequence (~20 m thick) comprises an alternation of dark gray to greenish-gray homogeneous mudstones with laminated grainstone. Mudstone gradually changes color from dark gray to greenish-gray with increasing bioturbation. Thinly laminated grainstone beds show basal scour, indicating that these sedimentary structures were generated by upper flow regime currents, possibly due to storm activity. The upper unit consists of greenish-gray mudstones to siltstones intercalated frequently with relatively thin massive packstone to grainstones and limestone pebble conglomerates.

The measured Duwibong Formation is about 45 m thick and consists of oncoid/ooid grainstone, massive bioclastic packstone to grainstone, bioturbated wackestone to packstone, and a limestone-shale couplet. Among these lithofacies, massive bioturbated wackestone to packstone is predominant. A fault bounds the top of the measure section. Biostratigraphically, the upper part of the Makgol Formation contains conodonts of Middle Ordovician age (*Aurilobodus leptosomatus* Zone; Darriwilian) (Lee, 1990), and the overlying Jigunsan Formation is characterized by a single trilobite

biozone (*Dolerobasilicus Zone*; Choi et al., 2001) and the *E. suecicus–E. jigunsanensis* conodont Zone of Darriwilian age (Lee, 1990; Lee and Lee, 1986). In recent studies, the biostratigraphy was updated to *Tangshanodus tanshanensis* zone to upper Makgol and lower Jigunsan Formation, and *E. suecicus* biozone as upper Jigunsan and Duwibong Formation as endemic biozone (**Fig. 3-4**) (Cho et al., 2021; Lee et al., 2022). The uppermost Duwibong Formation has unclear verification for the *A.serratus zone*, which correlated to slope setting *Pygodus serra* and cosmopolitan conodont zone (Cho et al., 2021; Jing et al., 2015).

This study considered clay mineral compositions as weathering proxies, especially the contents of the kaolinite and illite. The 2N HCl dissolution method has the possibility of dissolving chlorite and Na-rich smectite. Still, when the clay mineral is dissolved, the XRD peak appears reduced compared to the background at the corresponding position and is not denatured in the form of a kaolinite peak (Hu et al., 2022; Komadel and Madejová, 2006). It is known that illite has only partial solubility when treated with HCl, and kaolinite is almost insoluble (Hu et al., 2022). In addition, the crystal factor was also measured for illite, so the effect of dissolution can be identified by referring to the relevant part, which is not found to be high (Bang and Lee, 2020).

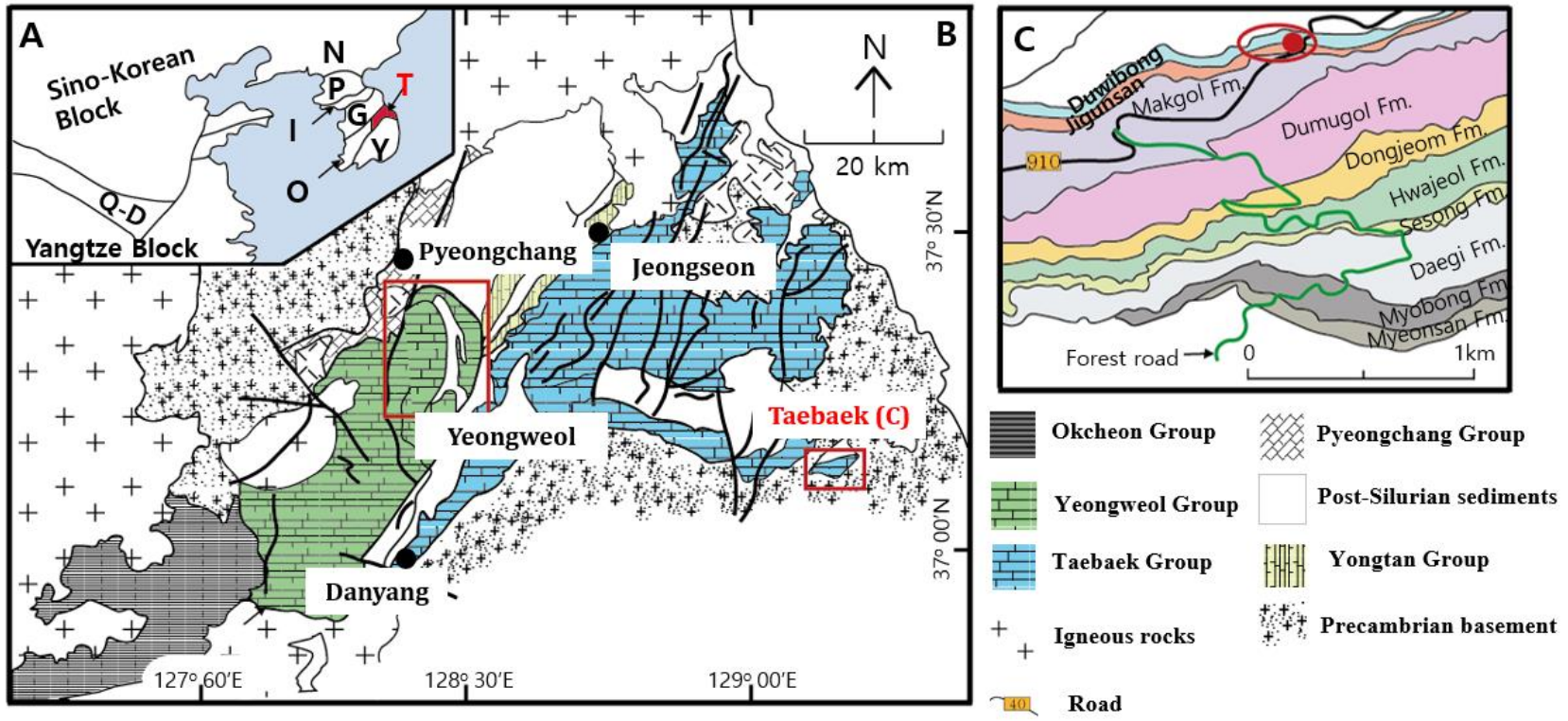


**Figure 3-3.** Map showing central eastern Korea and studied sections. (A) The inset shows the tectonic divisions of the Korean Peninsula and the location of the Taebaeksan Basin (I: Imjingang Belt; G: Gyeonggi Massif; N: Nangnim Massif; O: Okcheon Belt; P: Pyeongnam Basin; Q–D: Qinling–Dabie Belt; T: Taebaeksan Basin; Y: Yeongnam Massif). (B) Location of the Taebaeksan Basin (modified after Choi and Chough, 2005). The studied sections are marked by red dots in the (C) Taebaek (after Lee and Lee, 1986) areas. (modified from Bang and Lee, 2020)

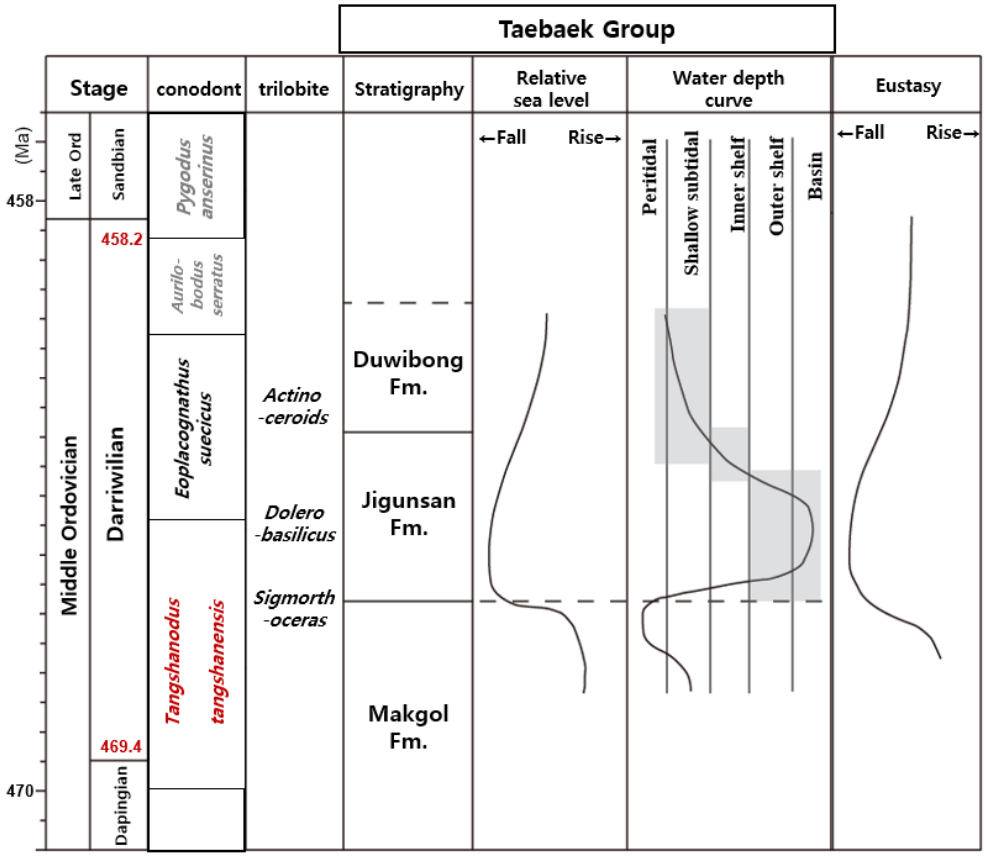


**Figure 3-4.** Updated age model of Taebaek group Makgol, Jigunsan, Duwigon Formation (Modified after Bang and Lee, 2020), applying new biostratygraphy (Cho et al., 2021), Middle Ordovician timescale (Gradstein et al., 2020), Sequence stratigraphy from (Kwon and Kwon, 2020).

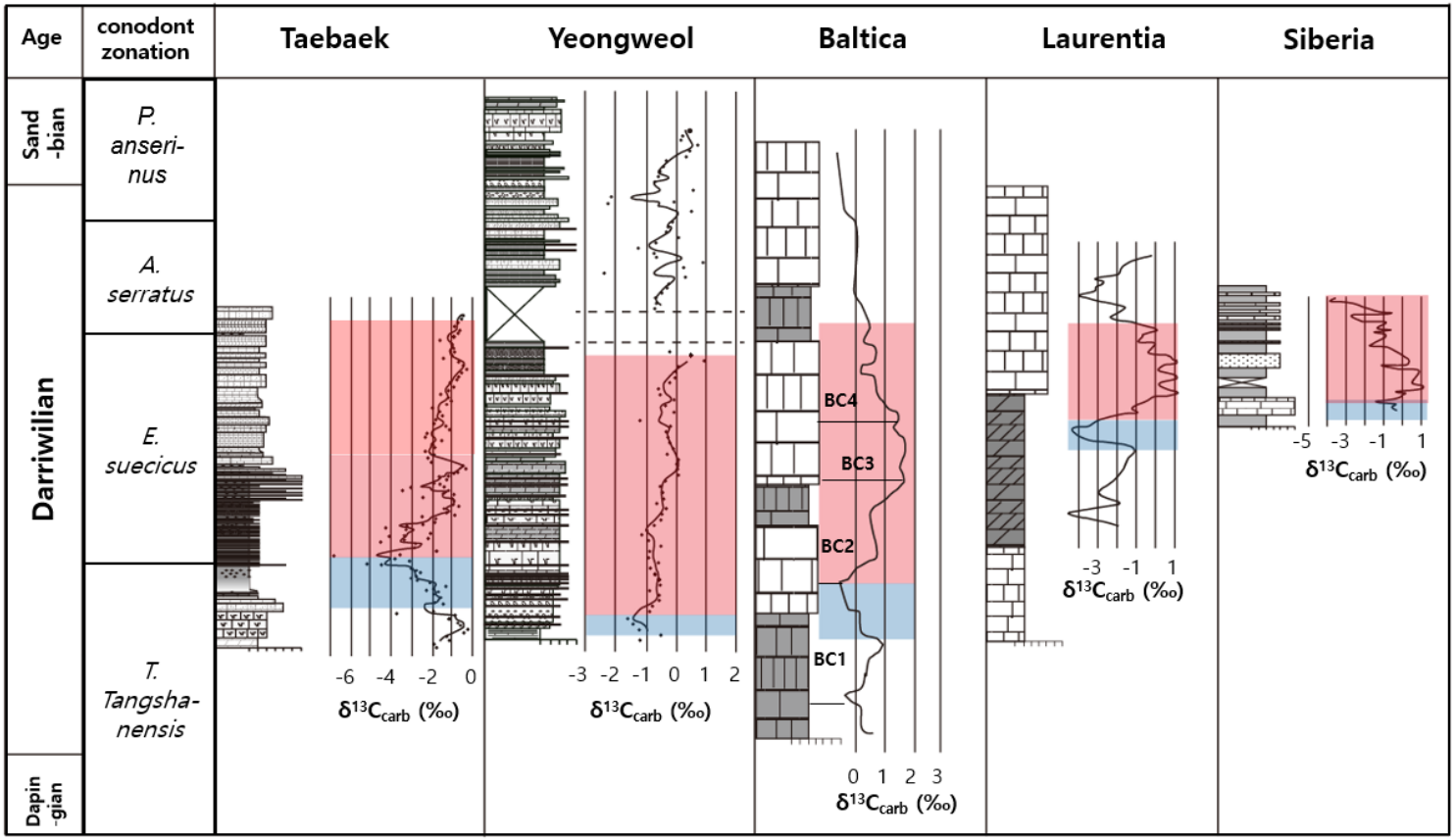


**Figure 3-5.** Correlation of biostratigraphy, carbon isotope chemostratigraphy, and lithostratigraphy among MDICE records in SKB (the Taebek and Yeongweol sections; Bang and Lee, 2020), Baltica (Ainsaar et al., 2010), Laurentia (Kah et al., 2015), and Siberia (Nõlvak et al., 2006). Red area: MDICE; blue area: LDNICE. modified from Bang and Lee, 2020

### 3.3.2. Pretreatment & Extraction

All dissolution and column separation processes were carried out under a ULPA-filtered laminar flow bench for the low air-born boron levels. All nitric acid was used after passing through 5 times distillations by the all-Teflon Savillex DST-1000 system.

Before powdering each sample, this study uses a grinder to cut rocks to 1x1cm cubic shape, excluding veins, microfossils, and contaminated parts. Each sample was powdered with agate mortar and pestle, as the method of selecting only the portion with suitable micrite during grinding was the same as the previous study on carbon isotopes (Bang and Lee, 2020) and boron isotopes (Clarkson et al., 2015; Paris et al., 2010).

All powdered samples were slurried and centrifuged in 50 ml Milli-Q water (**Table 3-2**; 2-3 g rock powder, 10 seconds in 500 rpm) to remove supernatant and particles in size <4 μm. This process prevented geochemical contamination by the dissolution of salt and clay minerals. The sediment after the clay removal centrifuge was dried at room temperature.

Each 600 mg of size-fraction samples (>4 μm) was dissolved in 1 ml of 1 M $HNO_3$ in a flat-bottom teflon vial for 2 hours, including 1 hour of shaking and degassing time in an ultrasonicator. The supernatants of this process were taken by micro-centrifuging in a 2 ml tube, for 10 minutes at 4400 rpm. After centrifugation, 600 μl of the supernatant was collected, 20 μl was diluted for Ca, Na, and Mg analysis, and 50 μl was diluted for Al, Mn, Ba, and Sr analysis for ICP-MS. To the remaining 530 μl of the carbonate-dissolved solution, 1.45 ml of 0.075 M $HNO_3$ was added to adjust acid

concentration for the boron separation column process.

A new method for separating boron from carbonate rock, an incredibly extremely rich Ca matrix, was developed by modifying the bed volume from the two-step column method for porite coral (McCulloch et al., 2014), two-step column for porite coral (**Fig. 3-6**). **Fig. 3-7** summarizes several tests of this separation method, and the recovery of each test was maintained at 94-106%.

The sample that went through this separation process was analyzed for boron concentration and isotope ratio using Nu Plasma 3, MC-ICPMS at the national center for inter-university research facilities (NC-IRF) at Seoul National University.

### 3.3.3. ICP-MS analysis

Major and trace elements were analyzed for Ca, Na, Mg, Al, Mn, Sr and Ba by Agilent 8900-QQQ ICPMS at the school of Earth environment science in Seoul National University. The sample solutions were diluted to 50,000-fold (for Ca, Na, Mg) and 10- fold (Al, Mn, Sr, Ba), and analyzed in concentration curve of cation standard (50-300 ppb). The uncertainty was less than 5% for all elements (**Table 3-2**). Our dissolved carbonate rock sample solutions show low Al/Ca which means no silicate mineral contamination in this study (mostly less than 3 μmol/mol, maximum 325 μmol/mol; **Table 3-2**).

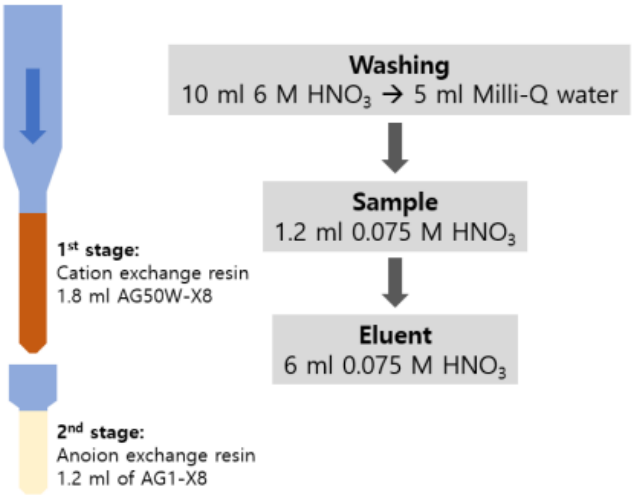


**Figure 4-6**. Schematic diagram of boron column separation method in this study

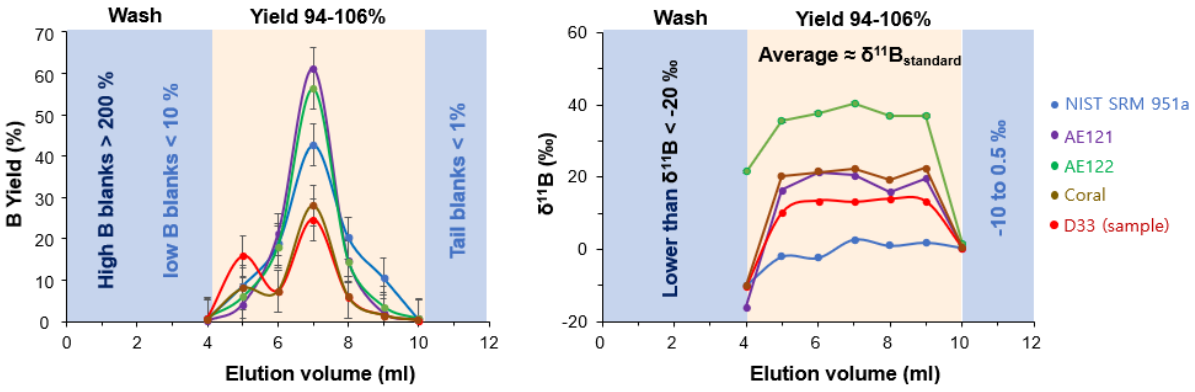


**Figure 3-7.** Boron yield (%, ±internal error, 5 %) and $\delta^{11}B_{carbonate}$ (±internal error, 0.4‰) from new column method of this study. Each standard $\delta^{11}B$: NIST SRM 951a = 0‰, AE121 = 19.6‰, AE122 = 39.6‰, Carbonate rock sample D33 was tested (Peleozoic carbonate range : 7 to 16.5‰; Clarkson et al., 2015; Yang et al., 2018; Jurikova et al., 2020).

### 3.3.4. MC-ICP-MS analysis

The boron isotope ratio was measured using the NuPlasma3 MC-ICPMS at the National Center for Inter-university Research Facilities at Seoul National University (SNU-IRF). Mass 11 boron was collected on H6 Faraday cup equipped with a $10^{-11}$ Ω resistor, and mass 10 was collected on L6 with a $10^{-12}$ Ω resistor.

All samples were analyzed by the sample-standard bracketing using NIST SRM 951a as the standard of $\delta^{11}B = 0$ ‰. The column separation recovery and isotope ratio were confirmed in **Fig. 3-7** by the boron isotope standards NIST SRM 951a ($^{11}B/^{10}B = 4.04367$; Cantazaro et al., 1970), ERM-AE121 ($\delta^{11}B = 19.9 \pm 0.6$ ‰), ERM-AE122 ($\delta^{11}B = 39.7 \pm 0.6$ ‰), and an in-house carbonate standard PR83, a *Porites* coral from a Micronesia reef ($\delta^{11}B = 22.4 \pm 0.7$ ‰). Blanks were checked before and after the sample analysis, which maintained <5% of the sample signal (for ~60 ng/g of the sample [B], <3 ng blank). The long-term reproducibility was ± 0.6‰ at the 95% confidence interval, and the maximum uncertainty of the sample is ± 1.4 ‰ (**Fig. 3-7, Fig. 3-8**).

### 3.3.5. pH calculation from $\delta^{11}B_{carbonate}$

The $\delta^{11}B$ range of modern marine biogenic carbonates has been reported to be 22.1 ±3‰ (Hemming and Hanson, 1992), and the $\delta^{11}B$ range of modern seawater is generally 39.5‰ (Swihart and Moore, 1989; Vengosh et al., 1992; Zeebe et al., 2001). In this study, considering the $\delta^{11}B$ difference (+17.4‰) between this modern carbonate and seawater, we added the corresponding value

to our $\delta^{11}B_{carb}$ value and converted it to $\delta^{11}B_{sw}$. The pH we mainly refer to in the text is the pH calculated using the value of $\delta^{11}B_{sw}$ = 29.1‰ obtained by converting the average ($\delta^{11}B_{carb}$ = 11.7‰) of our $\delta^{11}B_{carb}$ values. At this time, the case obtained using the minimum ($\delta^{11}B_{carb}$ =7.5‰) among our $\delta^{11}B_{carb}$ values is of $\delta^{11}B_{sw}$ = 24.9‰, and the pH of seawater obtained using this value appears high ($pCO_2$ low scenario). On the other hand, if the seawater value is obtained using the maximum value ($\delta^{11}B_{carb}$ = 16.2‰) among the $\delta^{11}B_{carb}$ data, $\delta^{11}B_{sw}$ = 33.6‰, and the pH of the seawater obtained using this value is low ($pCO_2$ high scenario). In this calculation, the estimated pH results of the seawater becomes lower in higher $\delta^{11}B_{sw}$, because the sample $\delta^{11}B_{carb}$ is calculated as having a relatively much lower $\delta^{11}B$ value compared to the value of higher $\delta^{11}B_{sw}$ in seawater. The fractionation factor αB of 1.0272 (Zeebe and Wolf-Gladrow, 2001) were substituted in the following equation (Foster and Rae, 2016; Vengosh et al., 1992).

$$pH = pK_B^* - \log\left(-\frac{\delta^{11}B_{seawater} - \delta^{11}B_{borate}}{\delta^{11}B_{seawater} - (\alpha B \times \delta^{11}B_{borate}) - 1000 \times (\alpha B - 1)}\right)$$

pKB* is constant from the T=25 ºC, S=35 psu. $\delta^{11}B_{sw}$ becomes the values obtained based on the average, maximum, and minimum values above. Most of marine carbonate $\delta^{11}B_{carb}$ is $\delta^{11}B_{borate}$ of seawater (Clarkson et al., 2015; Yang et al., 2018), the $\delta^{11}B_{carb}$ value of our samples are substituted in $\delta^{11}B_{borate}$ position.

## 3.4. Results and discussion

### 3.4.1. Comparison of Darriwilian $\delta^{13}C$, $\delta^{15}N$ and $\delta^{11}B$ records in the Taebaeksan basin

Comparison of $\delta^{11}B$ and $\delta^{13}C$ showed some excursions consistent with the main MDICE peak (**Fig. 3-8**), confirmed in pH simulations (**Fig.3-9**). The $\delta^{13}C$ stratigraphy of the Taebaek section (**Fig.3-8**, $\delta^{13}C$) is characterized by the appearance of three positive shifts (TC1, TC4, and TC6) and three negative shifts (TC2, TC3, and TC5). Among them, TC3 is known to have the lowest value (−6.8‰) and TC7 to have the highest value (−0.3‰). The intervals with these characteristics are the peaks reported as TC1, TC2, TC4, and TC6 in the existing $\delta^{13}C$ stratigraphy. Although this study has a lower resolution (3-4 m scale) than the $\delta^{13}C$ study (1-2 m scale; Bang and Lee, 2020), there was no great difficulty in identifying the main $\delta^{13}C$ and $\delta^{11}B$ peaks along the MDICE. However, two samples (J22, J2-10; **Table 3-2**) corresponding to TC3 in the existing carbon isotope record had Mn/Sr values exceeding 6 (ppm/ppm), so the data from these samples ($\delta^{13}C$, $\delta^{15}N$, $\delta^{11}B$, Mn, Sr, Ba) were excluded from major analyses (**Fig.3-8, Fig.3-10, Fig.3-11**). In addition, when these two samples are included, there is a high Mn/Sr correlation with two extremely negative $\delta^{13}C$ values in TC3, resulting in $R^2 = 0.7$, but in the condition of the two sample data excluded, showed very little correlation ($R^2 = 0.0224$; **Fig.3-10**). However, when the two data points are included, only $\delta^{13}C$ had a high correlation with Mn/Sr, but the correlation with other factors was very low ($R^2 < 0.1$), similar to the case when it was not excluded. Considering these points, since the correlation between stable isotopes (**Fig.3-10**; $\delta^{13}C$, $\delta^{15}N$, $\delta^{11}B$) excluding those points is very low, there is sufficient room for interpretation as a primary signal of carbonate rock overall. These low relationships indicate low

alteration signals in data regarding the contents of Sr and Ba will decrease, and Mn content will increase (Averyt et al., 2003; Wang et al., 2021) in altered carbonates. Since $\delta^{15}N$ in bulk rock is mainly contained in primary organic matter (OM), in the cases that OM is decomposed by alteration,$^{15}N$-depleted parts will be relatively absent, and the value will become much heavier than the scale in this study (+20-40‰) (Herbert, 1999; Schoeninger and DeNiro, 1984; Wang et al., 2013). Suppose alteration events with heat or hydrothermal intrusion, elemental concentrations, and isotope values would tend to be aligned according to recrystallization or alteration of the rock's micrite. However, such a phenomenon was not found in the cross plot in this study (**Fig. 3-11**).

The negative trend from $\delta^{13}C$ stratigraphy to TC1-TC2 (~10m) also appears on negative $\delta^{15}N$ and $\delta^{11}B$. This time interval suggests that a decrease in productivity and a well-circulated state occurred along with acidification in the upper part of the Makgol. In the sequence stratigraphy, this period is the period when the sea level is expected to rise rapidly from the maximum flooding of sea level (**Fig.3-4**; Woo and Chough, 2007). Due to this sea level change, the Taebaeksan Basin would have become a shallow environment with a significant effect of mixing by wind, and denitrification became challenging to occur, which can explain the value of $\delta^{15}N$ became lighter. However, the co-occurrence of the lighter $\delta^{13}C$ and $\delta^{11}B$ indicates an increased dissolved CO2 in the seawater. The onset of subduction and closure of paleo-oceans around the Tarim basin (NW China, independent peri-Gondwanan block adjacent N.China block in Middle Ordovician time scale) activated related hydrothermal activity (Guo et al., 2020a; Huang et al., 2020), and slight increasing of volcanic Hg (~1ppb in Cambrian to Middle Ordovician Dapigian, ~5ppb during Darriwilian) in Yichang section

(S.China) observed (Gong et al., 2017), and also some evidence of Taconic orogeny of Laurentia continent (Berry et al., 2002; Jin et al., 2013; Saltzman and Young, 2005; Young et al., 2015). These weak tectonic influences in early Darriwilian have some possible relationships with the negative change of $\delta^{13}C$ and $\delta^{11}B$ (Gong et al., 2017; Guo et al., 2020b; Jiu et al., 2020; Zhang and Munnecke, 2015) in TC1-TC2. However, there are very few studies on the environment of the Peri-Gonwana platform in early Darriwilian, so more research is needed in this period.

TC4 (37m height, $\delta^{13}C$ = 0.88 ‰) is a section accompanied by an excursion of TN3 (37.5 m, $\delta^{15}N$ =9.41 ‰), and in this study, minimum $d^{11}B$ (32 m, $\delta^{11}B$ =7.5 ‰, pH= ~7.98) before this section appeared, but at points TC4 and TN3, the pH recovered to (37 m, $\delta^{11}B$ =11.5, pH= ~8.29) the value of alkaline seawater. Coincidentally, the point where the lowest pH appears (32 m) is the stratigraphy near the recently assumed boundary between T. tangshanensis and E. suesicus (Cho et al., 2021; Jing et al., 2022). $\delta^{13}C$ at this point was also very low (32 m, $\delta^{13}C$ = -2.04 ‰), implying that the seawater $pCO_2$ was relatively high, just like the change in TC1-TC2. If the dominant species of conodonts decreased during this time due to the acidification of platform seawater and surface productivity increased with sea level rise, it is possible that (TC4) became the dominant species. The heavy TN3 values are understood to be due to seawater stratification, which may be caused by high surface layer productivity and processes introducing freshwater into the surface layer. This part will be further interpreted in **Section 3.4.2** with proxies for anoxia and paleosalinity.

TC6 is the highest $\delta^{13}C$ peak (51m, $\delta^{13}C$ = -0.49 ‰) and also the highest $\delta^{11}B$-pH point (51m, $\delta^{11}B$ = 16.24, pH= ~8.6) in this study. This period was well-circulated seawater conditions (lower

$\delta^{15}N$) with high productivity. It must have been a favorable condition for the invasion of carbonate and the growth of organisms with calcareous bodies. Considering that the vicinity of MDICE's highest peak often correlates with the early part of GOBE, when biodiversity was rapidly increasing, this period must have been a favorable environment for carbonate-based organisms and the species that interact with carbonate platform to thrive, at least in the Taebaek area.

Unlike other heavy $\delta^{13}C$-$\delta^{11}B$ cases, TC7 is characterized by high $\delta^{13}C$ (69m, -1.04‰), slightly lowered $\delta^{11}B$ and pH (69m, 10.6‰, ~ 8.26). Although this decrease in pH is insignificant, it is difficult to explain the other tendency of TC7 only by comparing stable isotopes in this study. In the next section, we will understand this part with anoxia and paleosalinity proxy.

Although the period we study is ~6.6 Myr, which is a much smaller time scale than the 14–20 Myr residence time of boron (Spivack and Edmond, 1987; Yang et al., 2018), local boron concentrations and isotope ratios can be more influenced by local tectonic events with additional boron supply, rather than global boron residence time (Clarkson et al., 2015; Kasemann et al., 2000; Ma et al., 2011). The major sources for the input of boron include terrigenous influx (Lemarchand et al. 2002), submarine hydrothermal activities (Spivack and Edmond 1987), trench supplement-induced divergent currents (Kopf and Deyhle 2002), and volcanic activities related to land differentiation (Hemming et al. 1998; Rose et al. 2000). In particular, these cases assumes large continental sediment influx by orogenic events at the riverine basin level, at which the carbonate platform cannot be maintained. However, our study area maintained a marl-carbonate platform environment with 30–99% $CaCO_3$, although there may have been a slight increase in the input of

weathered continental matter or interaction with the surrounding seawater. In addition, if the value of $\delta^{11}B$ of seawater has changed due to the influx of substances from the continent, it will be possible to confirm because much more negative values will be found than the $\delta^{11}B$ value of general carbonate rock, and the results are observed within the reported the $\delta^{11}B$ range of ancient carbonate rock. (Clarkson et al., 2015; Yang et al., 2018).

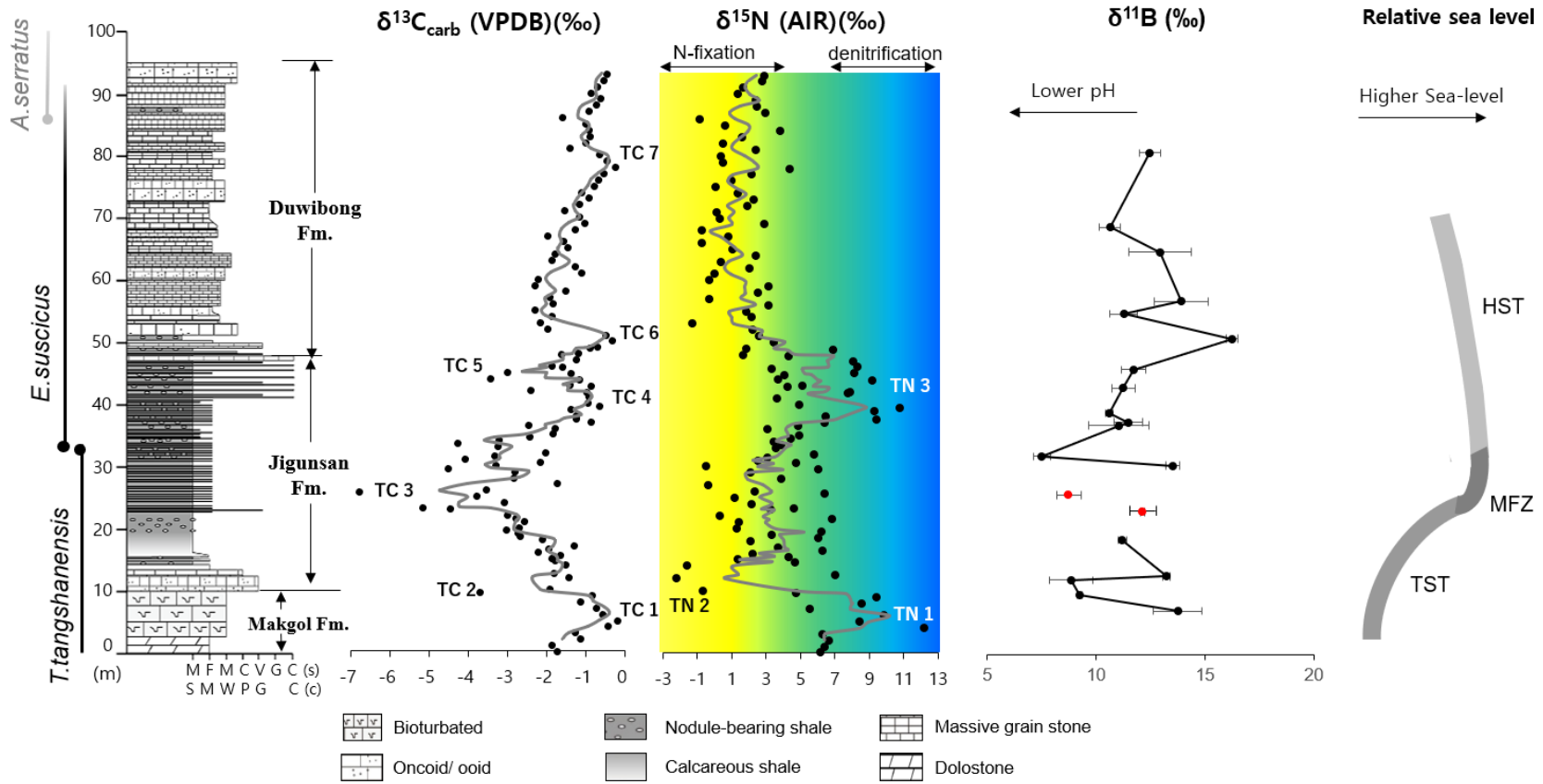


**Figure 3-8.** Biostratigraphy, lithology, $\delta^{13}C_{carb}$, $\delta^{15}N$ (Bang and Lee, 2020) and $\delta^{11}B$ from bulk carbonate rock (micrite) with relative sea level in Taebaek, Seokgaejae section (Woo and Chough, 2007)

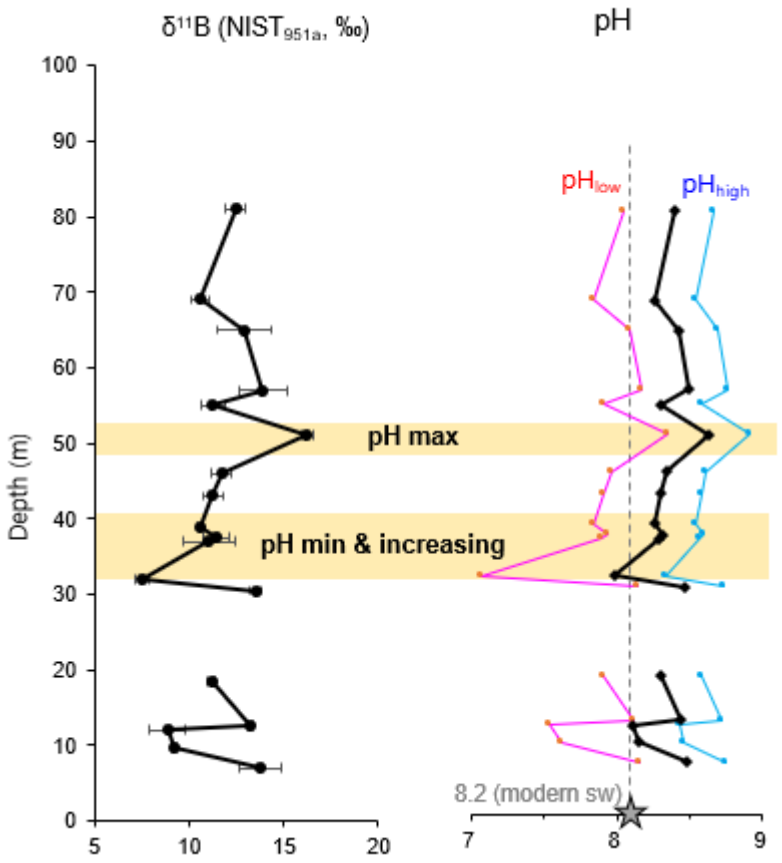


**Figure 3-9.** $\delta^{11}B$ from bulk carbonate rock (micrite) and simulated pH in this study.

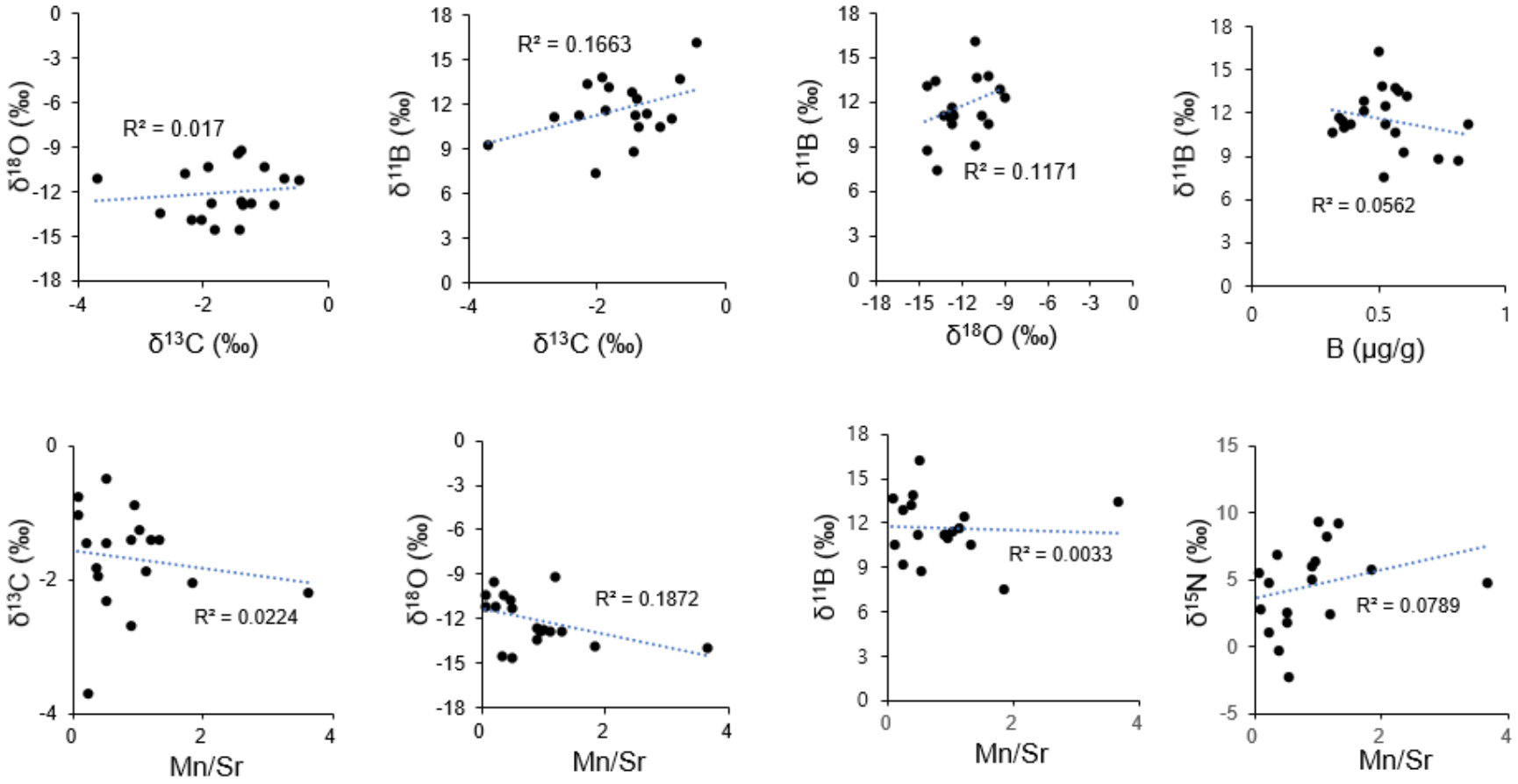


**Figure 3-10.** Comparisons of stable isotopes ( $\delta^{13}C_{carb}$, $\delta^{18}O_{carb}$, $\delta^{15}N$ and $\delta^{11}B$ from bulk carbonate) and B, Mn/Sr

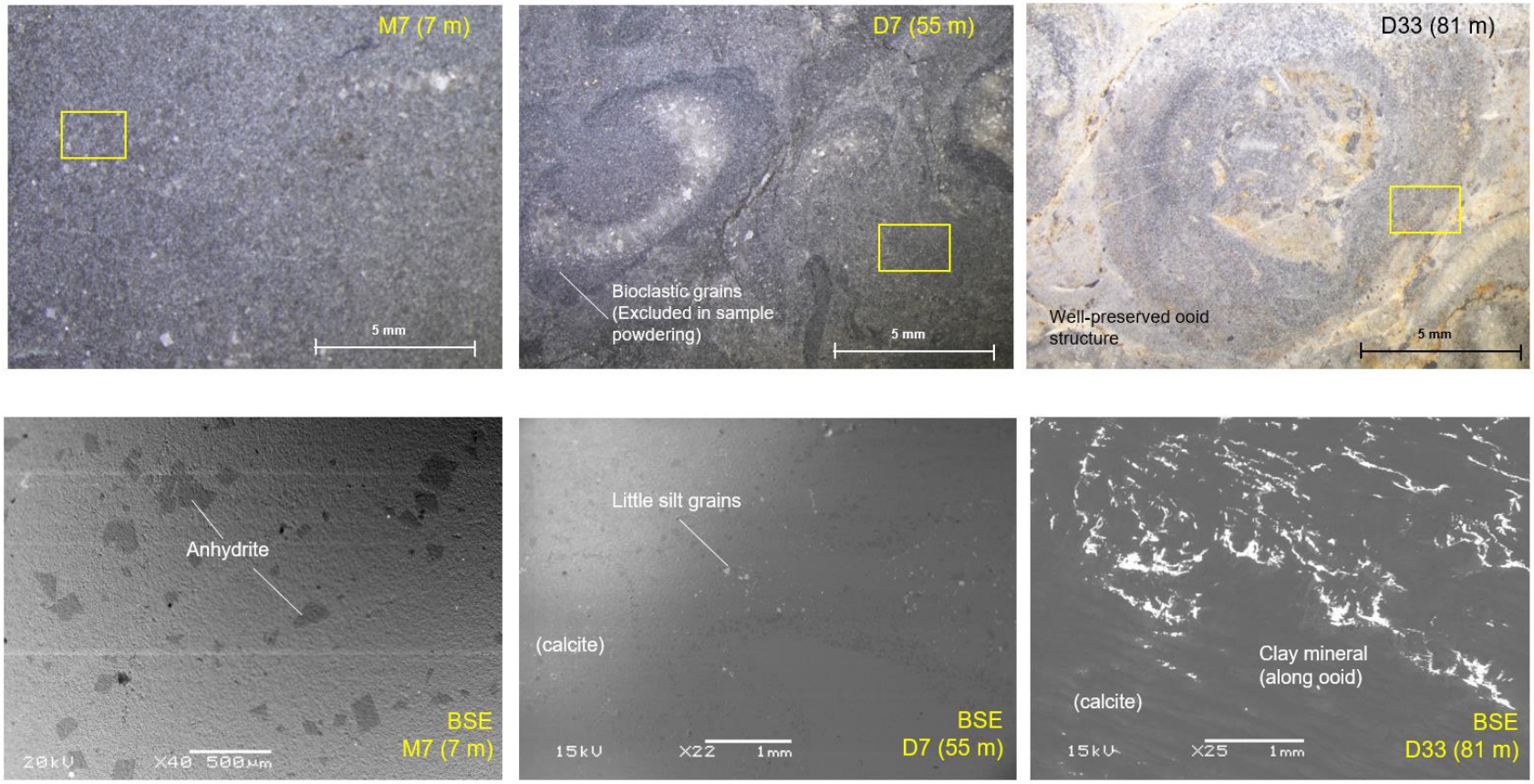


*BSE: Back scattered electron (SEM images)

**Figure 3-11.** Microscopic images (above) and back scattered elctron image (BSE; below) of samples

**Table 3-2.** Results of $\delta^{13}C_{carb}$, $\delta^{18}O_{carb}$, $\delta^{15}N_{bulk}$ (data from Bang and Lee, 2020) and $\delta^{11}B$, $\delta^{11}B$-derived pH, B, Mn, Sr (μg/g) and Al/Ca (μmol/mol).

| Sample | Height (m) | $\delta^{13}C$ (‰)* | $\delta^{18}O$ (‰)* | $\delta^{15}N$ (‰)* | $\delta^{11}B$ (‰) | 1sd for $\delta^{11}B$ | $pH_{average}$ | $pH_{pCO2low}$ | $pH_{pCO2high}$ | B (μg/g) | Mn (μg/g) | Sr (μg/g) | Al/Ca (μmol/mol) |
|---|---|---|---|---|---|---|---|---|---|---|---|---|---|
| M7 | 7 | -0.7 | -11.1 | 5.5 | 13.8 | 1.1 | 8.5 | 8.8 | 8.2 | 0.6 | 1.3 | 22.5 | 0.1 |
| J2-1 | 9.6 | -3.7 | -11.1 | 4.8 | 9.2 | 0.1 | 8.1 | 8.5 | 7.6 | 0.6 | 4.8 | 23.4 | 0.2 |
| J1 | 12 | -1.4 | -14.6 | -2.2 | 8.9 | 1.0 | 8.1 | 8.4 | 7.5 | 0.7 | 13.4 | 26.5 | 3.8 |
| J2-2 | 12.6 | -1.8 | -14.5 | 7.0 | 13.2 | 0.2 | 8.4 | 8.7 | 8.1 | 0.6 | 6.7 | 20.0 | 0.1 |
| J2-6 | 18.5 | -2.7 | -13.4 | 6.0 | 11.2 | 0.2 | 8.3 | 8.6 | 7.9 | 0.9 | 21.8 | 24.9 | 3.5 |
| J22 | 23 | -4.5 | -15.2 | 3.3 | 12.1 | 0.1 | | | | 0.4 | 102.2 | 16.9 | 10.0 |
| J2-10 | 25.7 | -6.8 | -15.7 | 6.4 | 8.8 | 0.6 | | | | 0.8 | 162.1 | 14.2 | 9.2 |
| J2-12 | 30.5 | -2.2 | -13.9 | 4.7 | 13.5 | 0.3 | 8.5 | 8.7 | 8.1 | 0.6 | 47.6 | 13.1 | 325.4 |
| J31 | 32 | -2.0 | -13.8 | 5.8 | 7.5 | 0.4 | 8.0 | 8.3 | 7.0 | 0.5 | 42.1 | 23.2 | <0.1 |
| J36 | 37 | -0.9 | -12.8 | 6.4 | 11.0 | 1.4 | 8.3 | 8.6 | 7.9 | 0.4 | 10.2 | 11.0 | <0.1 |
| J2-17 | 37.5 | -1.3 | -12.7 | 9.4 | 11.5 | 0.7 | 8.3 | 8.6 | 7.9 | 0.4 | 28.8 | 28.9 | <0.1 |
| J38 | 39 | -1.4 | -12.8 | 9.3 | 10.6 | 0.2 | 8.3 | 8.5 | 7.8 | 0.3 | 18.2 | 14.1 | <0.1 |
| J42 | 43 | -1.4 | -12.6 | 5.1 | 11.3 | 0.5 | 8.3 | 8.6 | 7.9 | 0.4 | 14.0 | 16.0 | <0.1 |
| J45 | 46 | -1.9 | -12.8 | 8.3 | 11.7 | 0.6 | 8.3 | 8.6 | 8.0 | 0.3 | 16.0 | 14.5 | <0.1 |
| D3 | 51 | -0.5 | -11.2 | 2.6 | 16.2 | 0.3 | 8.6 | 8.9 | 8.3 | 0.5 | 6.0 | 12.2 | <0.1 |
| D7 | 55 | -2.3 | -10.7 | 1.9 | 11.3 | 0.7 | 8.3 | 8.6 | 7.9 | 0.5 | 10.5 | 22.3 | <0.1 |
| D9 | 57 | -1.9 | -10.3 | -0.3 | 13.9 | 1.2 | 8.5 | 8.8 | 8.2 | 0.5 | 5.9 | 16.6 | <0.1 |
| D17 | 65 | -1.5 | -9.4 | 1.0 | 12.9 | 1.4 | 8.4 | 8.7 | 8.1 | 0.4 | 3.2 | 16.7 | <0.1 |
| D21 | 69 | -1.0 | -10.3 | 2.9 | 10.6 | 0.5 | 8.3 | 8.5 | 7.8 | 0.6 | 1.2 | 16.6 | <0.1 |
| D33 | 81 | -1.4 | -9.1 | 2.4 | 12.5 | 0.5 | 8.4 | 8.7 | 8.0 | 0.5 | 13.6 | 11.4 | <0.1 |

*data from Bang and Lee, 2020

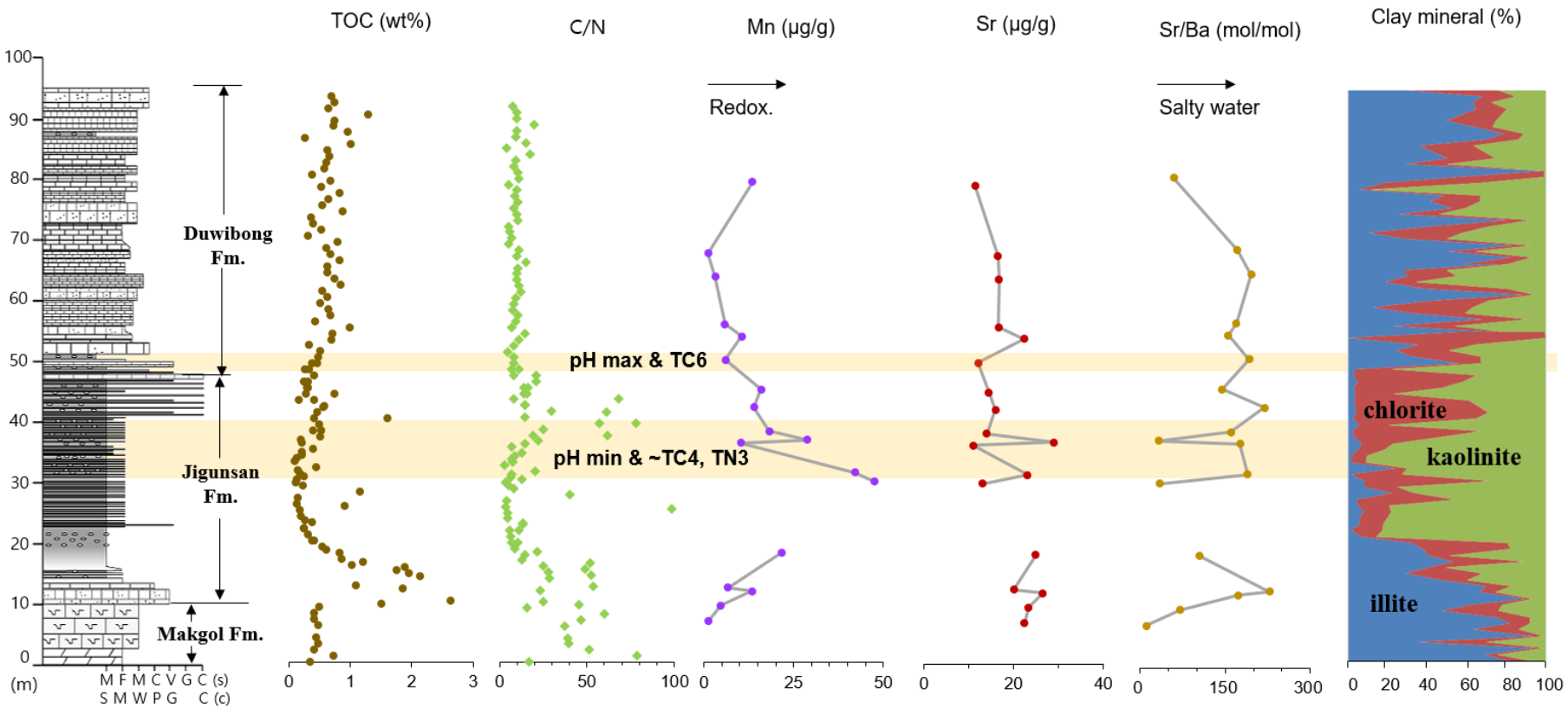


**Figure 3-12.** lithology and TOC, $C_{org}/N_{total}$ (g/g), Mn (μg/g), Sr (μg/g), Sr/Ba (mol/mol), Clay mineral (wt%)

### 3.4.2. Implications for carbonate platform anoxia and ocean acidification

The characteristics of the geochemical proxies mainly compared in this study are shown in **Fig.3-12**. In this study, high TOC (>1%) was considered as a criterion for indicating the degree of anoxia (Algeo et al., 2016b; Tyson, 1995), the high C/N ratio (> 25) was understood that there was a possibility of organic matter introduced from the land (LaPorte et al., 2009). The content of Mn was interpreted to have concentrated in the redox condition, especially anoxic environment (Lu et al., 2010; Mucci, 2004; Zhang et al., 2020). The content of Sr has a decreasing pattern and correlation with Mn, it can be interpreted as a signal of alteration (Brand et al., 2010; Brand and Veizer, 1980), or it can be interpreted as an accumulation of $Sr^{+}$ ions due to drying and evaporation in the carbonate platform environment (Averyt et al., 2003; Jiang et al., 2001; Wang et al., 2021). $Ba^{2+}$ is also one of the cations that can be accumulated by seawater evaporation; the range of values of Sr/Ba when the sediment is in seawater and freshwater environments are known to some extent in the process of burial, and it indicates what solution the sediment was in at the time of burial and early diagenesis (Chen et al., 2015; Liu et al., 2021; Song et al., 2016): In the saltwater medium, Sr/Ba is larger than 1. In the freshwater medium, Sr/Ba ratio is smaller than 0.6. If Sr/Ba is within the range of 0.6-1, the diagenetic fluid has a transitional feature between saltwater and freshwater. Overall, it was confirmed that our samples were in a typical seawater environment with no significant change in Sr content and the minimum value of Sr/Ba of 10.7 (7 m; **Fig. 3-12**). Clay mineral proxies are recently used in two directions, soli weathering profiles (Alizai et al., 2012; Sang et al., 2019) and provenance from the source terrain (Li et al., 2020; Újvári et al., 2014). In the case of climatological use, the distribution of kaolinite is prominent where there is a lot of rainfall, and illite-chlorite is the main component when

there is moderate rainfall (Singer, 1980). However, when clay minerals are used as tracers of provenance, clay minerals with similar degrees of weathering, such as illite/smectite, are usually compared (Rao and Rao, 1995). In the case of kaolinite, which has a more severe chemical weathering, it should be interpreted together with weathering. Indeed, clay minerals' composition is affected by both variations of weathering and provenance, such as examples of the South China Sea (He et al., 2020; Li et al., 2020; Sang et al., 2019).

In part corresponding to the upper part of the Makgol layer (0-10m; TC1-TC2 in $\delta^{13}C$ stratigraphy), the change in TOC was not conspicuous, rather than the highest TOC value appeared in the lower part of the Jikunsan layer (TC2-TC3 in $\delta^{13}C$ stratigraphy). This time interval was estimated through the values of $\delta^{13}C$-$\delta^{11}B$ as the shallower platform environment and increased dissolved $pCO_2$. Low $\delta^{15}N$ and low TOC and Mn contents can be understood as strong mixing by wind or surface flow. However, in the section corresponding to TC1-TC2, a high C/N ratio appeared, a low Mn content, and the lowest Sr/Ba (7 m, Sr/Ba = 10.7) value appeared. Considering this, it seems that the inflow of organic matter from the land was active along with the influx of precipitation or freshwater. However, during this period, it is thought that the rainfall was not intense because the proportion of kaolinite in the clay mineral composition was not high, and small freshwater channels may transport reworked continental organic matter into the shallow environment (Strasser, 2022; Wright, 1994).

The period where the minimum pH value appears and then recovers, followed by excursions of TC4 and TN3, is characterized by a very high Mn content and then a decrease. Considering the importance of Sr/Ba, it is thought that the inflow of precipitation or freshwater was quite large, then it

was affected by seawater again, and then the influx of rainfall was intensified again. This part coincides with the occasionally high C/N points and the section where the kaolinite composition of clay mineral rapidly increases, so it can be seen that the nearby soil and derived organic matter caused intense leaching by precipitation and partially entered to carbonate platform (Bang and Lee, 2020). Unlike the previous sections, it is estimated that the low pH section before TC4 and TN3 was a climate greatly affected by strong precipitation that dissolved much $CO_2$ in the atmosphere. In other words, the factor that caused the low $\delta^{13}C$ and $\delta^{11}B$-pH of seawater at this time was probably atmospheric $CO_2$ influx. The process may have been driven by climate accompanied by strong precipitation. Due to surface desalination and sea level rise, the surface layer with high productivity and poor circulation under the mixed layer would have been isolated, resulting in an environment where redox conditions and denitrification were active (High Mn content, heavy $\delta^{15}N$). Acid rain with high atmospheric $pCO_2$ (lower than pH 5.6) is significant acidification, and weathering factor in modern reef platforms and soil profiles (Chisholm and Barnes, 1998; Li et al., 2020; Pandolfi et al., 2011; Reitner, 1993; Sivaramanan, 2015), and extinction events caused by it have been reported on geological timescales such as Aptian (Aina, 2011; Veron, 2008) and Ediacaran (Michail, 2022).

TC6, an ideal carbonate accumulation environment as estimated by stable isotopes, was well-circulated (low TOC, Mn content) and seemed to have reduced disturbing by precipitation or freshwater (higher Sr/Ba, lower C/N, kaolinite content). This may be because the platform's depth has been stabilized below the mixed layer due to the rising sea level.

The upper point (69 m) corresponding to TC7 is a time zone characterized by heavy $\delta^{13}C$ and light

$\delta^{11}B$ (lower pH). TOC and C/N at this time were very low, and the Mn content was also low, indicating that it was a well-circulated environment. However, what is different from the previous period is that the value of Sr/Ba increases and then decreases, and in these periods, kaolinite and chlorite are intermittently high. Even at this time, there was occasional intense soil weathering by increased precipitation, which may have contributed to the slightly lowered pH. However, if the surface carbon utilities had stabilized by very high productivity, the value of $\delta^{13}C$ could have remained heavy, despite occasional atmospheric $CO_2$ dissolution with precipitation.

## 3.5. Conclusion

In this study, we compared reconstructed $\delta^{11}B$ and approximate pH fluctuations from carbonate rock to the Middle Ordovician $\delta^{13}C_{carb}$ stratigraphic time interval of MDICE with other palaeoceanographic proxies. As a result, acidification of the carbonate platform was induced by precipitation before TC4 among the existing MDICE features, anoxia and denitrification were influenced in the lower part of the mixed layer with the rise of the sea level. These changes may have caused an environment where some previously dominant species went extinct, and new dominant species emerged and adapted. Afterward, pH and seawater circulation conditions favorable to carbonate accumulation were maintained until TC6. At this time, some circumstances may have favored the growth and development of organisms with calcareous shells. These characteristics show that the platform with high productivity in the Taebaek area declined due to shallowing and acidification and then matured again, indicating the possibility that it created an environment favorable to the differentiation of Middle Ordovician species.

## 3.6 References


Aina, E.D., 2011. Development and loss of porosity in the Lower Cretaceous (Aptian-Albian) Sligo Formation shelf edge reef, South Texas. Mississippi State University.

Ainsaar, L., Kaljo, D., Martma, T., Meidla, T., Männik, P., Nõlvak, J., Tinn, O., 2010. Middle and Upper Ordovician carbon isotope chemostratigraphy in Baltoscandia: a correlation standard and clues to environmental history. Palaeogeography, Palaeoclimatology, Palaeoecology 294, 189-201.

Ainsaar, L., Männik, P., Dronov, A.V., Izokh, O.P., Meidla, T., Tinn, O., 2015. Carbon isotope chemostratigraphy and conodonts of the Middle–Upper Ordovician succession in the Tungus Basin, Siberian Craton. Palaeoworld 24, 123-135.

Ainsaar, L., Meidla, T., Tinn, O., 2004. Middle and Upper Ordovician stable isotope stratigraphy across the facies belts in the East Baltic, WOGOGOB-2004 Conference Materials. Tartu University Press, Tartu, pp. 11-12.

Ainsaar, L., Tinn, O., Dronov, A., Kiipli, E., Radzevičius, S., Meidla, T., 2020. Stratigraphy and facies differences of the Middle Darriwilian isotopic carbon excursion (MDICE) in Baltoscandia. Estonian journal of earth sciences 69, 214-222.

Albanesi, G.L., Bergström, S.M., Schmitz, B., Serra, F., Feltes, N.A., Voldman, G.G., Ortega, G., 2013. Darriwilian (Middle Ordovician) δ 13 C carb chemostratigraphy in the Precordillera of Argentina: Documentation of the middle Darriwilian Isotope Carbon Excursion (MDICE) and its use for intercontinental correlation. Palaeogeography, Palaeoclimatology, Palaeoecology 389, 48-63.

Algeo, T.J., Marenco, P.J., Saltzman, M.R., 2016a. Co-evolution of oceans, climate, and the biosphere during the 'Ordovician Revolution': a review. Palaeogeography, Palaeoclimatology, Palaeoecology 458, 1-11.

Algeo, T.J., Marenco, P.J., Saltzman, M.R., 2016b. Co-evolution of oceans, climate, and the biosphere during the 'Ordovician Revolution': A review. Palaeogeography, Palaeoclimatology, Palaeoecology.

Alizai, A., Hillier, S., Clift, P.D., Giosan, L., Hurst, A., VanLaningham, S., Macklin, M., 2012. Clay mineral variations in Holocene terrestrial sediments from the Indus Basin. Quaternary Research 77, 368-381.

Averyt, K.B., Paytan, A., Li, G., 2003. A precise, high-throughput method for determining Sr/Ca, Sr/Ba, and Ca/Ba ratios in marine barite. Geochemistry, Geophysics, Geosystems 4.

Bang, S., Lee, Y.I., 2020. Darriwilian carbon isotope stratigraphy in the Taebaeksan Basin, Korea and its implications for Middle Ordovician paleoceanography. Palaeogeography, Palaeoclimatology, Palaeoecology

541, 109534.

Bergstroem, S.M., Chen, X., GUTIÉRREZ-MARCO, J.C., Dronov, A., 2009. The new chronostratigraphic classification of the Ordovician System and its relations to major regional series and stages and to δ13C chemostratigraphy. Lethaia 42, 97-107.

Berry, W.B., Ripperdan, R.L., Finney, S.C., 2002. Late Ordovician extinction: a Laurentian view. SPECIAL PAPERS-GEOLOGICAL SOCIETY OF AMERICA, 463-472.

Brand, U., Azmy, K., Tazawa, J.-i., Sano, H., Buhl, D., 2010. Hydrothermal diagenesis of Paleozoic seamount carbonate components. Chemical Geology 278, 173-185.

Brand, U., Veizer, J., 1980. Chemical diagenesis of a multicomponent carbonate system; 1, Trace elements. Journal of Sedimentary Research 50, 1219-1236.

Chen, J., Chen, P., Yao, D., Liu, Z., Wu, Y., Liu, W., Hu, Y., 2015. Mineralogy and geochemistry of Late Permian coals from the Donglin Coal Mine in the Nantong coalfield in Chongqing, southwestern China. International Journal of Coal Geology 149, 24-40.

Cherns, L., Wheeley, J.R., Popov, L., Pour, M.G., Owens, R., Hemsley, A.R., 2013. Long-period orbital climate forcing in the early Palaeozoic? Journal of the Geological Society 170, 707-710.

Chisholm, J.R., Barnes, D.J., 1998. Anomalies in coral reef community metabolism and their potential importance in the reef CO2 source-sink debate. Proceedings of the National Academy of Sciences 95, 6566-6569.

Cho, S.H., Lee, B.-S., Lee, D.-J., Choh, S.-J., 2021. The Ordovician succession of the Taebaek Group (Korea) revisited: old conodont data, new perspectives, and implications. Geosciences Journal 25, 417-431.

Choi, D.K., Chough, S.K., 2005. The Cambrian-Ordovician stratigraphy of the Taebaeksan Basin, Korea: a review. Geosciences Journal 9, 187-214.

Choi, D.K., Chough, S.K., Kwon, Y.K., Lee, S.-B., Woo, J., Kang, I., Lee, H.S., Lee, S.M., Sohn, J.W., Shinn, Y.J., 2004. Taebaek group (Cambrian-Ordovician) in the Seokgaejae section, Taebaeksan Basin: a refined lower Paleozoic stratigraphy in Korea. Geosciences Journal 8, 125-151.

Clarkson, M., Kasemann, S.A., Wood, R., Lenton, T., Daines, S., Richoz, S., Ohnemueller, F., Meixner, A., Poulton, S.W., Tipper, E., 2015. Ocean acidification and the Permo-Triassic mass extinction. Science 348, 229-232.

Deng, Y., Fan, J., Zhang, S., Fang, X., Chen, Z., Shi, Y., Wang, H., Wang, X., Yang, J., Hou, X., 2021. Timing

and patterns of the Great Ordovician Biodiversification Event and Late Ordovician mass extinction: Perspectives from South China. Earth-Science Reviews 220, 103743.

Dronov, A., 2013. Late Ordovician cooling event: evidence from the Siberian Craton. Palaeogeography, Palaeoclimatology, Palaeoecology 389, 87-95.

Fang, Q., Wu, H., Wang, X., Yang, T., Li, H., Zhang, S., 2019. An astronomically forced cooling event during the Middle Ordovician. Global and Planetary Change 173, 96-108.

Foster, G.L., Marschall, H.R., Palmer, M.R., 2018. Boron isotope analysis of geological materials, Boron Isotopes. Springer, pp. 13-31.

Foster, G.L., Rae, J.W., 2016. Reconstructing ocean pH with boron isotopes in foraminifera. Annual Review of Earth and Planetary Sciences 44, 207-237.

Gong, Q., Wang, X., Zhao, L., Grasby, S.E., Chen, Z.-Q., Zhang, L., Li, Y., Cao, L., Li, Z., 2017. Mercury spikes suggest volcanic driver of the Ordovician-Silurian mass extinction. Scientific Reports 7, 1-7.

Gradstein, F.M., Ogg, J.G., Schmitz, M.D., Ogg, G.M., 2020. Geologic time scale 2020. Elsevier.

Greenop, R., Hain, M.P., Sosdian, S.M., Oliver, K.I., Goodwin, P., Chalk, T.B., Lear, C.H., Wilson, P.A., Foster, G.L., 2017. A record of Neogene seawater δ 11 B reconstructed from paired δ 11 B analyses on benthic and planktic foraminifera. Climate of the Past 13, 149-170.

Guo, C., Chen, D., Qing, H., Zhou, X., Ding, Y., 2020a. Early dolomitization and recrystallization of the Lower-Middle Ordovician carbonates in western Tarim Basin (NW China). Marine and Petroleum Geology 111, 332-349.

Guo, R., Zhang, S., Bai, X., Wang, K., Sun, X., Liu, X., 2020b. Hydrothermal dolomite reservoirs in a fault system and the factors controlling reservoir formation-A case study of Lower Paleozoic carbonate reservoirs in the Gucheng area, Tarim Basin. Marine and Petroleum Geology 120, 104506.

Haq, B.U., Schutter, S.R., 2008. A chronology of Paleozoic sea-level changes. Science 322, 64-68.

He, J., Garzanti, E., Dinis, P., Yang, S., Wang, H., 2020. Provenance versus weathering control on sediment composition in tropical monsoonal climate (South China)-1. Geochemistry and clay mineralogy. Chemical Geology 558, 119860.

Hemming, N.G., Hanson, G.N., 1992. Boron isotopic composition and concentration in modern marine carbonates. Geochimica et Cosmochimica Acta 56, 537-543.

Herbert, R., 1999. Nitrogen cycling in coastal marine ecosystems. FEMS microbiology reviews 23, 563-590.

Hu, B., Zhang, C., Zhang, X., 2022. The Effects of Hydrochloric Acid Pretreatment on Different Types of Clay Minerals. Minerals 12, 1167.

Huang, Y., Fan, T., Berra, F., 2020. Architecture and paleogeography of the Early Paleozoic carbonate systems in the east-central Tarim Basin (China): constraints from seismic and well data. Marine and Petroleum Geology 113, 104147.

Jiang, M., Zhu, J., Chen, D., Zhang, R., Qiao, G., 2001. Carbon and strontium isotope variations and responses to sea-level fluctuations in the Ordovician of the Tarim Basin. Science in China Series D: Earth Sciences 44, 816-823.

Jin, J., Harper, D.A., Cocks, L.R.M., McCausland, P.J., Rasmussen, C.M., Sheehan, P.M., 2013. Precisely locating the Ordovician equator in Laurentia. Geology 41, 107-110.

Jing, X., Zhao, Z., Fu, L., Zhang, C., Fan, R., Shen, Y., Yang, B., 2022. Biostratigraphically-controlled Darriwilian (Middle Ordovician) δ13C excursions in North China: Implications for correlation and climate change. Palaeogeography, Palaeoclimatology, Palaeoecology 601, 111149.

Jing, X., Zhou, H., Wang, X., 2015. Ordovician (middle Darriwilian-earliest Sandbian) conodonts from the Wuhai area of Inner Mongolia, North China. Journal of Paleontology 89, 768-790.

Jiu, B., Huang, W., Mu, N., He, M., 2020. Effect of hydrothermal fluids on the ultra-deep Ordovician carbonate rocks in Tarim Basin, China. Journal of Petroleum Science and Engineering 194, 107445.

Jurikova, H., Neugebauer, I., Plessen, B., Henehan, M., Tjallingii, R., Schwab, M.J., Brauer, A., Blanchet, C., 2020. Boron isotope systematics of lacustrine carbonates: a new approach for tracing the palaeo-hydroclimatic evolution of the Dead Sea, EGU General Assembly Conference Abstracts, p. 16623.

Kah, L.C., Thompson, C.K., Henderson, M.A., Zhan, R., 2015. Behavior of marine sulfur in the Ordovician. Palaeogeography, Palaeoclimatology, Palaeoecology.

Kaljo, D., Martma, T., Saadre, T., 2007. Post-Hunnebergian Ordovician carbon isotope trend in Baltoscandia, its environmental implications and some similarities with that of Nevada. Palaeogeography, Palaeoclimatology, Palaeoecology 245, 138-155.

Kasemann, S., Erzinger, J., Franz, G., 2000. Boron recycling in the continental crust of the central Andes from the Palaeozoic to Mesozoic, NW Argentina. Contributions to Mineralogy and Petrology 140, 328-343.

Kasemann, S.A., Hawkesworth, C.J., Prave, A.R., Fallick, A.E., Pearson, P.N., 2005. Boron and calcium isotope composition in Neoproterozoic carbonate rocks from Namibia: evidence for extreme environmental change. Earth and Planetary Science Letters 231, 73-86.

Komadel, P., Madejová, J., 2006. Acid activation of clay minerals. Developments in clay science 1, 263-287.

Kwon, Y., Chough, S., Choi, D., Lee, D., 2006. Sequence stratigraphy of the Taebaek Group (Cambrian–Ordovician), mideast Korea. Sedimentary Geology 192, 19-55.

Kwon, Y.J., Kwon, Y.K., 2020. Sequence stratigraphy in the Middle Ordovician carbonate successions (Yeongheung Formation), mid-east Korea: Paleogeographic implications for a land-detached ramp-type platform. Journal of Asian Earth Sciences 193, 104263.

LaPorte, D., Holmden, C., Patterson, W., Loxton, J., Melchin, M., Mitchell, C., Finney, S., Sheets, H., 2009. Local and global perspectives on carbon and nitrogen cycling during the Hirnantian glaciation. Palaeogeography, Palaeoclimatology, Palaeoecology 276, 182-195.

Lee, B.-S., Cho, S.H., Choh, S.-J., Wang, X., 2022. Confirmation of the Floian-Darriwilian (Lower to Middle Ordovician) hiatus in the Taebaek Group, Korea: integration of conodont biostratigraphy and sedimentology. Geosciences Journal 26, 649-667.

Lee, K., 1990. Conodont biostratigraphy of the Upper Joseon Supergroup in Jangseong-Dongjeom area, Kangwondo. Journal of the Paleontological Society of Korea 6, 188-210.

Lee, S., 1989. Conodonts biostratigraphy and paleontology of the Lower Paleozoic Yeongheung Formation in the Yeongweol area, Kangweondo, Korea, unpubl. thesis, Yeonsei University, Seoul, 107p.

Lee, Y., Lee, H., 1986. Conodont biostratigraphy of the Jigunsan shale and Duwibong limestone in the Nokjeon-Sangdong area, Yeongweol-gun, Kangweondo. Korea. Journal of the Paleontological Society of Korea 2, 114-136.

Lee, Y.I., Choi, T., Lim, H.S., Orihashi, Y., 2016. Detrital zircon geochronology and Nd isotope geochemistry of the basal succession of the Taebaeksan Basin, South Korea: Implications for the Gondwana linkage of the Sino-Korean (North China) block during the Neoproterozoic–early Cambrian. Palaeogeography, Palaeoclimatology, Palaeoecology 441, 770-786.

Lehnert, O., Meinhold, G., Wu, R., Calner, M., Joachimski, M.M., 2014. [delta]^ sup 13^ C chemostratigraphy in the upper Tremadocian through lower Katian (Ordovician) carbonate succession of the Siljan district, central Sweden. Estonian Journal of Earth Sciences 63, 277.

Li, Y., Clift, P.D., Murray, R.W., Exnicios, E., Ireland, T., Böning, P., 2020. Asian summer monsoon influence on chemical weathering and sediment provenance determined by clay mineral analysis from the Indus Submarine Canyon. Quaternary Research 93, 23-39.

Liu, S., Zheng, D., Sun, J., Li, Y., 2021. Geochemical characteristics of the Ediacaran Dengying Formation in

South Qinling: implications for the dolomitization mechanism of dolomites and the terminal Ediacaran paleoenvironment. Arabian Journal of Geosciences 14, 1-21.

Lu, Z., Jenkyns, H.C., Rickaby, R.E., 2010. Iodine to calcium ratios in marine carbonate as a paleo-redox proxy during oceanic anoxic events. Geology 38, 1107-1110.

Ma, Y., Xiao, Y., He, M., Xiao, J., Shen, Q., Jiang, S., 2011. Boron isotopic composition of Paleozoic brachiopod and coeval coral calcites in Yunnan-Guizhou Plateau, China. Science China Earth Sciences 54, 1912-1925.

McCulloch, M.T., Holcomb, M., Rankenburg, K., Trotter, J.A., 2014. Rapid, high-precision measurements of boron isotopic compositions in marine carbonates. Rapid Communications in Mass Spectrometry 28, 2704-2712.

Michail, S., 2022. Ancient acid rains in the Ediacaran period–An alternative story for sulfate sedimentation. Precambrian Research 379, 106804.

Misra, S., Froelich, P.N., 2012. Lithium isotope history of Cenozoic seawater: changes in silicate weathering and reverse weathering. science 335, 818-823.

Mucci, A., 2004. The behavior of mixed Ca–Mn carbonates in water and seawater: controls of manganese concentrations in marine porewaters. Aquatic Geochemistry 10, 139-169.

Munnecke, A., Zhang, Y., Liu, X., Cheng, J., 2011. Stable carbon isotope stratigraphy in the Ordovician of South China. Palaeogeography, Palaeoclimatology, Palaeoecology 307, 17-43.

Nõlvak, J., Hints, O., Männik, P., 2006. Ordovician timescale in Estonia: recent developments, Proceedings of the Estonian Academy of Sciences, Geology, pp. 95-108.

Pandolfi, J.M., Connolly, S.R., Marshall, D.J., Cohen, A.L., 2011. Projecting coral reef futures under global warming and ocean acidification. science 333, 418-422.

Paris, G., Bartolini, A., Donnadieu, Y., Beaumont, V., Gaillardet, J., 2010. Investigating boron isotopes in a middle Jurassic micritic sequence: Primary vs. diagenetic signal. Chemical Geology 275, 117-126.

Rae, J.W., Zhang, Y.G., Liu, X., Foster, G.L., Stoll, H.M., Whiteford, R.D., 2021. Atmospheric CO2 over the past 66 million years from marine archives. Annual Review of Earth and Planetary Sciences 49, 609-641.

Rao, V.P., Rao, B.R., 1995. Provenance and distribution of clay minerals in the sediments of the western continental shelf and slope of India. Continental Shelf Research 15, 1757-1771.

Rasmussen, C.M., Ullmann, C.V., Jakobsen, K.G., Lindskog, A., Hansen, J., Hansen, T., Eriksson, M.E.,

Dronov, A., Frei, R., Korte, C., 2016. Onset of main Phanerozoic marine radiation sparked by emerging Mid Ordovician icehouse. Scientific Reports 6, 1-9.

Rasmussen, J.A., Thibault, N., Mac Ørum Rasmussen, C., 2021. Middle Ordovician astrochronology decouples asteroid breakup from glacially-induced biotic radiations. Nature communications 12, 1-14.

Reitner, J., 1993. Modern cryptic microbialite/metazoan facies from Lizard Island (Great Barrier Reef, Australia) formation and concepts. Facies 29, 3-39.

Saltzman, M.R., Young, S.A., 2005. Long-lived glaciation in the Late Ordovician? Isotopic and sequence-stratigraphic evidence from western Laurentia. Geology 33, 109-112.

Sang, P.N., Liu, Z., Stattegger, K., 2019. Weathering and erosion in central Vietnam over the Holocene and Younger Dryas: Clay mineralogy and elemental geochemistry from the Vietnam Shelf, western South China Sea. Journal of Asian Earth Sciences 179, 1-10.

Schmitz, B., Bergström, S.M., Xiaofeng, W., 2010. The middle Darriwilian (Ordovician) δ13C excursion (MDICE) discovered in the Yangtze Platform succession in China: implications of its first recorded occurrences outside Baltoscandia. Journal of the Geological Society 167, 249-259.

Schmitz, B., Farley, K.A., Goderis, S., Heck, P.R., Bergström, S.M., Boschi, S., Claeys, P., Debaille, V., Dronov, A., Van Ginneken, M., 2019. An extraterrestrial trigger for the mid-Ordovician ice age: Dust from the breakup of the L-chondrite parent body. Science Advances 5, eaax4184.

Schoeninger, M.J., DeNiro, M.J., 1984. Nitrogen and carbon isotopic composition of bone collagen from marine and terrestrial animals. Geochimica et Cosmochimica Acta 48, 625-639.

Servais, T., Harper, D.A., 2018. The great Ordovician biodiversification event (GOBE): definition, concept and duration. Lethaia 51, 151-164.

Shuttleworth, R., Bostock, H., Chalk, T.B., Calvo, E., Jaccard, S., Pelejero, C., Martínez-García, A., Foster, G., 2021. Early deglacial CO2 release from the Sub-Antarctic Atlantic and Pacific oceans. Earth and planetary science letters 554, 116649.

Sial, A., Peralta, S., Gaucher, C., Toselli, A., Ferreira, V., Frei, R., Parada, M., Pimentel, M., Pereira, N.S., 2013. High-resolution stable isotope stratigraphy of the upper Cambrian and Ordovician in the Argentine Precordillera: Carbon isotope excursions and correlations. Gondwana Research 24, 330-348.

Singer, A., 1980. The paleoclimatic interpretation of clay minerals in soils and weathering profiles. Earth-Science Reviews 15, 303-326.

Sivaramanan, S., 2015. Acid rain, causes, effect and control strategies. Central Environmental Authority, Battaramulla 1.

Song, W., Xu, C., Veksler, I.V., Kynicky, J., 2016. Experimental study of REE, Ba, Sr, Mo and W partitioning between carbonatitic melt and aqueous fluid with implications for rare metal mineralization. Contributions to Mineralogy and Petrology 171, 1-12.

Spivack, A., Edmond, J., 1987. Boron isotope exchange between seawater and the oceanic crust. Geochimica et Cosmochimica Acta 51, 1033-1043.

Strasser, A., 2022. Shallow marine carbonates as recorders of orbitally induced past climate changes–example from the Oxfordian of the Swiss Jura Mountains. Climate of the Past 18, 2117-2142.

Swihart, G.H., Moore, P.B., 1989. A reconnaissance of the boron isotopic composition of tourmaline. Geochimica et Cosmochimica Acta 53, 911-916.

Thompson, C.K., Kah, L.C., 2012. Sulfur isotope evidence for widespread euxinia and a fluctuating oxycline in Early to Middle Ordovician greenhouse oceans. Palaeogeography, Palaeoclimatology, Palaeoecology 313, 189-214.

Trotter, J.A., Williams, I.S., Barnes, C.R., Lécuyer, C., Nicoll, R.S., 2008. Did cooling oceans trigger Ordovician biodiversification? Evidence from conodont thermometry. Science 321, 550-554.

Tyson, R.V., 1995. Abundance of organic matter in sediments: TOC, hydrodynamic equivalence, dilution and flux effects, Sedimentary organic matter. Springer, pp. 81-118.

Újvári, G., Varga, A., Raucsik, B., Kovács, J., 2014. The Paks loess-paleosol sequence: a record of chemical weathering and provenance for the last 800 ka in the mid-Carpathian Basin. Quaternary International 319, 22-37.

Vengosh, A., Starinsky, A., Kolodny, Y., Chivas, A.R., Raab, M., 1992. Boron isotope variations during fractional evaporation of sea water: New constraints on the marine vs. nonmarine debate. Geology 20, 799-802.

Veron, J.E., 2008. Mass extinctions and ocean acidification: biological constraints on geological dilemmas. Coral Reefs 27, 459-472.

Wang, A., Wang, Z., Liu, J., Xu, N., Li, H., 2021. The Sr/Ba ratio response to salinity in clastic sediments of the Yangtze River Delta. Chemical geology 559, 119923.

Wang, X., Shi, X., Tang, D., Zhang, W., 2013. Nitrogen Isotope Evidence for Redox Variations at the

Ediacaran-Cambrian Transition in South China. The Journal of Geology 121, 489-502.

Witzke, B.J., Bunker, B.J., 1996. Relative sea-level changes during Middle Ordovician through Mississippian deposition in the Iowa area, North American craton. SPECIAL PAPERS-GEOLOGICAL SOCIETY OF AMERICA, 307-330.

Woo, J., Chough, S.K., 2007. Depositional processes and sequence stratigraphy of the Jigunsan Formation (Middle Ordovician), Taebaeksan Basin, mideast Korea: implications for basin geometry and sequence development. Geosciences Journal 11, 331-355.

Wright, V.P., 1994. Paleosols in shallow marine carbonate sequences. Earth-Science Reviews 35, 367-395.

Xiong, Y., Tan, X., Zuo, Z., Zou, G., Liu, M., Liu, Y., Liu, L., Xiao, D., Zhang, J., 2019. Middle Ordovician multi-stage penecontemporaneous karstification in North China: Implications for reservoir genesis and sea level fluctuations. Journal of Asian earth sciences 183, 103969.

Yang, J., Zhang, Y., Chen, Y., Zhang, L., Zhu, C., Wang, Z., 2018. Methods for reconstruction of paleo-seawater pH based on boron isotopes in evaporative depositional sequences: case study using the Cambrian–Lower Ordovician evaporite sequence in the Tarim Block, NW China. Carbonates and Evaporites 33, 717-726.

Young, S.A., Gill, B.C., Edwards, C.T., Saltzman, M.R., Leslie, S.A., 2015. Middle–Late Ordovician (Darriwilian–Sandbian) decoupling of global sulfur and carbon cycles: Isotopic evidence from eastern and southern Laurentia. Palaeogeography, Palaeoclimatology, Palaeoecology.

Young, S.A., Saltzman, M.R., Foland, K.A., Linder, J.S., Kump, L.R., 2009. A major drop in seawater 87Sr/86Sr during the Middle Ordovician (Darriwilian): Links to volcanism and climate? Geology 37, 951-954.

Zeebe, R.E., Sanyal, A., Ortiz, J.D., Wolf-Gladrow, D.A., 2001. A theoretical study of the kinetics of the boric acid–borate equilibrium in seawater. Marine Chemistry 73, 113-124.

Zeebe, R.E., Wolf-Gladrow, D., 2001. CO2 in seawater: equilibrium, kinetics, isotopes. Gulf Professional Publishing.

Zhang, F., Dahl, T.W., Lenton, T.M., Luo, G., Shen, S.-z., Algeo, T.J., Planavsky, N., Liu, J., Cui, Y., Qie, W., 2020. Extensive marine anoxia associated with the Late Devonian Hangenberg Crisis. Earth and Planetary Science Letters 533, 115976.

Zhang, Y., Munnecke, A., 2015. Ordovician stable carbon isotope stratigraphy in the Tarim Basin, NW China. Palaeogeography, Palaeoclimatology, Palaeoecology.

# 국문초록

해양 탄산염($CaCO_3$)에 존재하는 붕소의 동위원소는 과거 해수의 pH와 $CO_2$ 함량을 지시하는 것으로 알려져 있다. 본 학위 논문에서는 과거 해양 탄산염(e.g.,신생대 유공충과 고생대 탄산염 암석들)을 이용한 붕소 동위원소 연구를 통해 해당 방법에 대한 이해를 증진시키는 것을 목표로 하고 있다. 이 학위 논문은 세 개의 장으로 이루어져 있으며 pH에 의존적인 붕소 동위원소의 분별 작용 (1장), 붕소 동위원소 기록에서 복원한 pH와 $pCO_2$에 대한 고해양학적 사례(2장과 3장)를 다룬다.

제 2장에서는 서북태평양(WNP) 샤스키 라이즈의 퇴적물 코어인 NPGM/P 1302-1B (32° 16′ N, 158° 13′ E, 2514 m water depth)에서 채집하고 전처리한 여러 종의 부유성 유공충으로부터 해수의 $pCO_2$ 기록을 복원하였고, 이는 마지막 최대빙하기 (LGM; 24 – 18 ka), 하인리히 아빙기-1 (HS1; 18 – 15 ka), 볼링-앨러로드 (B/A; 15 – 12.8 ka), 영거 드라이아스 한랭기(YD; 12.8 – 11.5 ka)의 시간 범위를 포함한다. 새로운 WNP의 $\delta^{11}B$, pH, pCO2 기록은 4-23 kyr에 달하며 주요한 CO2 방출에 대한 패턴이 LGM과 HS1의 변환기 (19.7 – 17.5 ka), HS1의 중반(16 – 17 ka)과 YD의 초반 시기에 나타났다. 또한 본 연구에서 WNP의 새로운 $\Delta pCO_2$ 데이터를 도출함으로써 다른 태평양 연구(북태평양, 적도대 서태평양, 적도대 동태평양)들과 비교할 수 있게 되었다. WNP는 LGM과 HS1, YD의 시기에 북태평양과 적도대 동태평양의 $\Delta pCO_2$와 유사한 패턴을 나타냈다. 이러한 변화는

대기 중 $CO_2$가 급격하게 증가하던 시간 범위에서 북반구 태평양의 표층-중층을 이루는 해류의 상호 관계로 설명할 수 있다.

제 3장에서는 태백층군의 하부 고생대에 해당하는 탄산염 암석으로부터 붕소 동위원소를 추출하여 분석한 연구를 다룬다. 이 연구에서는 불용해성 잔여물 함량이 서로 다른 탄산염 암석으로부터 효율적인 용해 과정을 시험하였고, 점토 광물에 의한 오염이 가장 적은 산의 농도와 반응 시간을 발견하였다. 이 새로운 전처리 방법을 적용하여 25개의 시료로부터 중기 다리윌리안(Darriwillian) 중기 오르도비스기의 새로운 $\delta^{11}B$ 기록을 복원할 수 있었다. 새로운 $\delta^{11}B_{bulk}$ 데이터는 최신 생층서대 정보를 반영하여 오르도비스기 해수의 $\delta^{11}B$ 선행 연구, $\delta^{13}C$ 화학층서와 상호 관계를 비교하였다. 이러한 비교 결과는 태백이 과거 페리-곤드와나(peri-Gondwana)의 내륙해 분지에 해당했던 얕은 탄산염 대지(carbonate platform)이었을 때, 해수 층서화와 산성화가 연관되어 나타났다는 가설을 지지한다.

**주요어 : 붕소 동위원소, 고해양학, $CO_2$ flux, 산성화, 해양 탄산염, 기후 변화**
**학 번 : 2017-34629**